

Benchmarking Protocols for Proton Exchange Membrane Water Electrolyser

by

Jonathan O. Kiangani

Thesis submitted in fulfilment of the requirements for the degree:

Master of Engineering in Chemical Engineering

in the Faculty of Engineering and the Built Environment

at the Cape Peninsula University of Technology

Supervised by:

Prof. Mahabubur Chowdhury (Cape Peninsula University of Technology)

Dr. Rhiyaad Mohamed (University of Cape Town)

October 2022

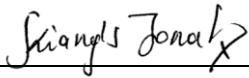
CPUT copyright information

This thesis may not be published either in part (in scholarly, scientific, or technical journals), or as a whole (as a monograph), unless permission has been obtained from the University.

DECLARATION

I, Jonathan O. Kiangani, declare that the contents of this thesis represent my own unaided work, any information and ideas derived from published work of others are acknowledged in the text and references are given in the Bibliography.

I further declare that the thesis has not previously been submitted for academic examination towards any qualification and it represents my own opinions and not necessarily those of the Cape Peninsula University of Technology.



Signed

01 October 2022

Date

ABSTRACT

Fossil fuel-based energy resources covers nearly 84 percent of the global primary energy consumption. However, the dependence on fossil fuel is no longer sustainable as these fuels account for more than 84 percent of anthropogenic greenhouse gas emissions. Renewable energy sources are the most promising alternatives to reduce anthropogenic greenhouse gas emissions. However, issues such as fluctuating and intermittent energy supply associated with these technologies require the use of energy storage. Proton exchange membrane water electrolysis (PEMWE) can be coupled with renewable energy sources to store excess energy in the form of hydrogen. However, the widespread commercial use of PEMWE is still impeded by its high operating cost, short durability and low system efficiency.

As a part of National Hydrogen and Fuel Cells Technologies Flagship project in South Africa, the HySA Catalysis Centre of Competence has been tasked to establish South Africa as one of the main global exporters of electrolyser technologies. This entails but not limited to the development of manufacturing processes for electrocatalysts and other components for PEMWE systems.

Towards meeting these objectives, in this project a fabrication method for PEMWE catalyst coated membranes (CCMs) was developed in house, using the Mayer rod coating technique. Anode catalyst layers were coated onto a polytetrafluoroethylene (PTFE, Teflon™) substrate from which it was transferred to a membrane via decal transfer, making up the 3-layer CCM used for electrochemical evaluation in an electrolyser cell. Several coating parameters were investigated to obtain uniform catalyst layers. It was found that the water to isopropyl alcohol mixture ratio of 3:1 and catalyst ink solid content of 30 wt% showed the most uniform catalyst layer surface structure and improved attachment to the substrate. A catalyst ink mixing time of 24 hours provided the most uniform distribution of the catalyst nanoparticle aggregate sizes. For the addition of pore forming additives to the catalyst ink suspension, complete transfer of the catalyst layer and removal of the pore forming additives was achieved with a hot-pressing pressure of as low as 500 Kg/cm² for 3 minutes.

Additionally, reliable electrochemical evaluation protocols to assess the performance of the fabricated CCMs were also developed. Several operating test parameters were investigated, where it was found that a compression of 4 kN and a water flow rate of 0.1 L/min provided better temperature control and improved overall CCM performance. Furthermore, from the porous transport layer (PTL) investigation, it was found that titanium powder sintered PTLs on both the anode and cathode sides provided a better overall electrolyser cell performance at

high current density operation. Also investigated, were the effects of different electrolyser cell conditioning and evaluation measurement parameters on the overall CCM performance and it was found that the shortest cell conditioning time of 5 min provided the lower performance while cell conditioning times of 15 min, 30 min and 45 min showed no significant differences in their results. The addition of the open circuit voltage (OCV) step and the halving of the current-voltage measurement interval time from 5 min to 2.5 min provided the best CCM performance and improved significantly the cell performance profile at 1000 mA cm^{-2} over time.

Finally, the effect of pore forming additives to the anode catalyst ink on the anode catalyst layer morphology and overall PEMWE cell performance was investigated. Ammonium carbonate and ammonium bicarbonate with varying weight ratios were used as pore forming additives in the catalyst ink formulation and subsequently removed during the decal transfer process. The investigation was conducted on both Nafion 212 and Nafion 115 membranes. From the investigation of pore forming additives effects, the physical characterisation of the anode catalyst layers data showed that an increase of porosity (pore size, pore quantity and pore distribution) in the anode catalyst layer was achieved in this study. The addition of pore forming substances increased the quantity of pores in the catalyst layer by 2.5-fold (from 30% to $74 \pm 1\%$ of the total catalyst layer volume) and 1.3-fold (from 30% to $45\% \pm 0.5\%$ of the total catalyst layer volume) for pore forming materials to catalyst weight ratios of 1:1 and 1:10, respectively for the Nafion 212 CCMs samples. ~ 1.75 -fold (from 40% to 70% of the total catalyst layer volume) and ~ 1.5 -fold (from 40% to around 60% of the total catalyst layer volume) for 1:1 and 1:10 ammonium bicarbonate to $\text{IrO}_x\text{-TiO}_2$ weight ratio, respectively for Nafion 115 CCMs samples.

The electrochemical performance evaluation of the PEMWE cell showed that the addition of pore forming additives to the anode electrode catalyst ink formulation allowed for the reduction of iridium catalyst loading while improving the electrochemical performance. The iridium catalyst loading reduction of up to 45% was achieved while improving the overall cell performance, with CCM of $1.31 \text{ mg}_{\text{Ir}} \text{ cm}^{-2}$ performing with 1.89 V at 1 A cm^{-2} and $0.72 \text{ mg}_{\text{Ir}} \text{ cm}^{-2}$ performing with 1.82 V at 1.0 A cm^{-2} . Furthermore, the electrochemical evaluation tests showed that the CCMs with a high number of pores in their catalyst layers had the best catalyst utilisation compared to CCMs without pore formers.

ACKNOWLEDGEMENTS

First, I would like to thank the staff at HySA Catalysis institute at UCT who made this work possible. To Dr. Rhiyaad Mohamed, who gave me a first-hand exposure to the research and development of green hydrogen production technology. To Dr. Darija Susac, who put tremendous efforts into assisting me with the physical characterisation of the prepared samples and providing her world-class expertise and knowledge of proton exchange membrane water electrolyser technology which were essential in guiding the writing of this thesis. To Nyasha Mawungwe, Durga Iyer, and everyone in the analytical laboratory in the chemical engineering department who assisted me with the handling of analytical equipment and some experimental work setups.

Secondly, I would like to convey my gratefulness to Dr. Mahabubur Chowdhury, my research supervisor at CPUT, whose assistance and valuable academic insights made this work possible.

A special note of gratitude to my parents, M. T Mabilia, and father, P. K Kiangani for support their and belief in me.

Finally, to my wonderful spouse, A. Ngulube, thank you for being patient, understanding and supporting. My love for you is infinite.

TABLE OF CONTENTS

DECLARATION	i
ABSTRACT.....	ii
ACKNOWLEDGEMENTS	iv
LIST OF FIGURES	v
LIST OF TABLES.....	ix
NOMENCLATURE	x
ABBREVIATIONS	xi
GLOSSARY	xii
OUTPUTS FROM THIS STUDY	xiii
CHAPTER 1 INTRODUCTION.....	1
1.1. An Overview of the Global Energy Sector.....	1
1.2. Hydrogen as Renewable Energy Storage.....	1
1.3. An Overview of Water Electrolysis.....	2
1.3.1. Basic Chemistry of Water Electrolysis.....	2
1.3.1.1. Types of Water Electrolysis Technologies.....	2
1.4. Proton Exchange Membrane Water Electrolysis.....	3
1.4.1. Basic Principles of the PEMWE	4
1.4.2. Challenges of PEMWE	4
1.5. Problem Statement.....	5
1.6. Objectives	5
1.7. Scope of the Study	6
1.8. Significance of the Study	6
1.9. Thesis Outline	6
CHAPTER 2 BACKGROUND INFORMATION AND LITERATURE REVIEW	8
2.1. PEMWE Materials and Components	8
2.1.1. Bipolar Plate	9
2.1.2. Porous Transport Layer	9
2.1.3. Proton Exchange Membrane	9

2.1.4.	Electrocatalyst Layer.....	10
2.2.	Principles of PEMWE	10
2.2.1.	Thermodynamics	10
2.2.2.	Kinetics – Current Density.....	12
2.3.	PEMWE Voltage Losses	13
2.3.1.	Activation Overvoltage	13
2.3.2.	Ohmic Overvoltage	14
2.3.3.	Concentration Overvoltage	15
2.4.	An Overview of the PEMWE Electrodes Fabrication.....	17
2.4.1.	PEMWE Catalyst Ink Formulation	17
2.4.1.1.	Ionomer	17
2.4.1.2.	Solvent.....	17
2.4.2.	PEMWE Catalyst Ink Mixing Methods	20
2.4.2.1.	High Shear Mixing	20
2.4.2.2.	Ultrasonication	21
2.4.2.3.	Ball Milling	21
2.4.3.	PEMWE Catalyst Ink Coating Methods	22
2.4.3.1.	Screen Printing	22
2.4.3.2.	Ultrasonic Spray	23
2.4.3.3.	Mayer Rod Coating.....	23
2.4.4.	Decal Transfer and Hot Pressing	23
2.5.	PEMWE Anode Electrode Catalyst Layer	24
2.5.1.	Anode Catalyst Layer Structure	24
2.5.2.	Anode Catalyst Layer Properties.....	26
2.6.	An Overview of the PEMWE Electrodes Evaluation.....	26
2.6.1.	Physical Characterisations.....	26
2.6.1.1.	Scanning Electron Microscopy.....	26
2.6.1.2.	Energy Dispersive X-Ray Spectroscopy.....	28
2.6.2.	Electrochemical Characterisations	28

2.6.2.1. Current – Voltage Performance	28
2.6.2.2. Electrochemical Impedance Spectroscopy.....	28
2.7. Highly Porous Electrodes Catalyst Layers	30
2.7.1. Pore Forming Additives Properties.....	30
2.7.2. Effects of Pore Forming Additives on Electrodes Structures and Overall PEM Systems Performance.....	31
CHAPTER 3 DEVELOPMENT OF THE FABRICATION METHOD FOR PEMWE ELECTRODES.....	33
3.1. Mayer Rod Coating	33
3.1.1. Mayer Rod Coater Parameters	33
3.1.2. Ink Formulation Parameters.....	35
3.1.2.1. Effects of Solvent Mixture Components Ratio	36
3.1.2.2. Effect of the Solid Content	38
3.1.3. Ink Mixing Parameters	40
3.2. Decal Transfer Process	41
3.3. Fabrication of PEMWE Electrodes Using Mayer Rod Coating	46
3.3.1. Chemicals and Materials Specifications	46
3.3.2. Catalyst Coated Membrane Method.....	48
3.3.2.1. Anode Catalyst Ink Formulation Procedure.....	48
3.3.2.2. Anode Catalyst Ink Mixing Procedure	49
3.3.2.3. Anode Catalyst Ink Coating Procedure	50
3.3.2.4. PEMWE Electrodes Fabrication Procedure.....	52
3.4. Fabrication of Highly Porous Anode Catalyst Layers Using Mayer Rod Coating.....	54
3.4.1. Catalyst Coated Membrane Method.....	54
3.4.2. Removal of Pore Forming Materials	55
3.5. Chapter Summary	58
CHAPTER 4 DEVELOPMENT OF THE ELECTROCHEMICAL EVALUATION PROTOCOLS FOR PEMWE SYSTEM	60
4.1. Development of the Current-Voltage Performance Evaluation Protocols	60
4.1.1. PEMWE System Hardware	60

4.1.1.1.	PEMWE Test Bench	60
4.1.1.2.	PEMWE Cell.....	63
4.1.2.	PEMWE Cell Assembly Protocols.....	64
4.1.2.1.	PEMWE CCM Preparation.....	64
4.1.2.2.	PEMWE Cell Connection	65
4.1.3.	Investigation of the PEMWE CCM Testing Parameters.....	66
4.1.3.1.	PEMWE Cell Compression	66
4.1.3.2.	PEMWE System Water Flow Rate	68
4.1.3.3.	PEMWE Porous Transport Layer	70
4.1.4.	PEMWE Cell Conditioning and Current-Voltage Measurement Parameters.....	72
4.2.	Commercial PEMWE CCMs Benchmarking	75
4.2.1.	Physical Characterisation.....	75
4.2.2.	Electrochemical Characterisations	76
4.3.	Chapter Summary	79
CHAPTER 5 EFFECTS OF PORE FORMING ADDITIVES ON THE PEMWE ANODE ELECTRODE CATALYST LAYER		81
5.1.	Highly Porous Anode Catalyst Layer on a Thin Proton Exchange Membrane.....	81
5.1.1.	Anode Catalyst Layer Physical Characterisation.....	81
5.1.1.1.	Anode Catalyst Layer Structure	81
5.1.1.2.	Anode Catalyst Layer Porosity.....	85
5.1.2.	PEMWE Current-Voltage Performance	88
5.2.	Highly Porous Anode Catalyst Layer on a Thick Proton Exchange Membrane	91
5.2.1.	Anode Catalyst Layer Physical Characterisation.....	91
5.2.1.1.	Anode Catalyst Layer structure.....	91
5.2.1.2.	Anode Catalyst Layer Porosity.....	94
5.2.2.	PEMWE Current-Voltage Performance	96
5.3.	Chapter Summary	99
CHAPTER 6 CONCLUSIONS AND RECOMMENDATIONS.....		101
6.1.	Conclusions.....	101

6.2. Recommendations	103
REFERENCES	104
APPENDIX.....	113

LIST OF FIGURES

Figure 2.1.1: Schematic illustration of a PEMWE cell. Including a proton exchange membrane (PEM) electrolyte; anode catalyst layer (CLa) and cathode catalyst layer (CLc); anodic porous transport layer (PTLa) and cathodic porous transport layer (PTLc) and two bipolar plates (Babic, et al., 2017).....	8
Figure 2.3.1: Schematic diagram illustrating the transport of reactants and products transport in the PEMWE single cell (Bernt & Gasteiger, 2016).....	15
Figure 2.3.2: Conceptual representation of performance influencing PEMWE electrode properties in the activation, ohmic, and mass transport regions of an electrolyser polarization curve (Merwe, et al., 2014).....	16
Figure 2.4.1: (a) Image of a High Shear Mixer. (b) Schematic diagram of the high shear mixing mechanism (Ross, 2015).	20
Figure 2.4.2: Schematic of an ultrasonic device with all the basic components (Kopeliovich, 2015).	21
Figure 2.4.3: Image of a ball mill and diagram of its main operating mechanisms (Paipetis & Kostopoulos, 2013).	22
Figure 2.5.1: An overview of the anode electrode catalyst layer triple-phase boundary (Bladergroen, et al., 2012).	25
Figure 2.6.1: SEM image of PEMWE components with (Xu, et al., 2011): (a) From bottom to top, a cross-sectional image of anode PTL (titanium sintered), anode electrode catalyst layer composed of electrocatalyst particles and ionomer, membrane, cathode electrode composed of electrocatalyst particles and ionomer, cathode PTL (carbon paper). (b) & (c) Top view of the anode electrode catalyst layer at different image magnification.....	27
Figure 2.6.2: (a) Schematic representation of Randles circuit. (b) Typical impedance plot for a PEMWE cell with denoted resistance types for different regions. (c) Nyquist plot of Randles circuit frequency response (Bruce, et al., 1994; Merwe, et al., 2014; Randles, 1947).....	30
Figure 3.1.1: Optical microscope images of ATO coated substrates showing differences in the coated film surface obtained from ATO ink formulations solvent mixture of: (a) Water : IPA ratio of 1:3, (b) Water : IPA ratio of 1:1, and (c) Water : IPA ratio of 3:1.	37
Figure 3.1.2: Optical microscope images of ATO coated substrates surface showing the difference in ATO layers obtained from the ink solid content of (a) 25 wt.%, (b) 30 wt.%, (c) 35 wt.% and (d) 40 wt.%.	39
Figure 3.1.3: SEM images of ATO surface layer form the ink mixing time of: (a) 12 hours, (b) 18 hours, and (c) 24 hours.	41

Figure 3.2.1: SEM images of ATO anode coated substrate layer surfaces and cross-sections form various decal transfer pressures, hot pressed for 6 minutes.....	45
Figure 3.3.1: Schematic representation of the experimental procedures of the PEMWE electrodes fabrication developed in this study.	48
Figure 3.3.2: Image of chemicals and materials used in the anode electrode catalyst ink preparation.....	49
Figure 3.3.3: Roller mill machine used for anode electrode catalyst ink fabrication.	50
Figure 3.3.4: (a) Anode catalyst ink deposited onto the Teflon substrate. (b) Teflon substrate after the coating of the anode electrode catalyst ink. (c) Slightly dried catalyst ink coated substrate.	51
Figure 3.3.5: Images of IrO _x -TiO ₂ anode electrode catalyst layer coated on Teflon sheet. ..	51
Figure 3.3.6: Overview of the decal transfer process for the fabrication of the PEM water electrolyser electrodes using the CCM method (not drawn to scale).	52
Figure 3.3.7: Image of IrO _x -TiO ₂ anode catalyst layer and Pt/C cathode catalyst layer on a proton exchange membrane after decal transfer process forming a catalyst coated membrane (CCM).	53
Figure 3.4.1: Images of IrO _x -TiO ₂ anode electrode catalyst layer catalyst layer coated on a Teflon substrate with 1:10 NH ₄ HCO ₃ pore forming additive to IrO _x -TiO ₂ catalyst weight ratio.	54
Figure 3.4.2: Anode catalyst layer surface images and their corresponding chemical compositions obtained from EDX analysis of (a) sample without pore former, (b) sample with Ammonium Carbonate and (c) sample with Ammonium Bicarbonate.	57
Figure 4.1.1: Process flow diagram of the PEMWE electrochemical test bench used at HySA Catalysis Centre.....	62
Figure 4.1.2: Schematic illustration of a PEMWE single cell (not drawn to scale).....	63
Figure 4.1.3: PEM water electrolyser cell assembly with titanium (Pt) PTLs.....	65
Figure 4.1.4: Schematic illustration of the PEM water electrolyser cell assembly components (not drawn to scale).	65
Figure 4.1.5: PEMWE cell insertion into compression frame.	66
Figure 4.1.6: Current-voltage performance of commercial PEMWE CCMs at different cell compressions. Testing conditions: cell T.= 60°C, cell P = 1 bara, 0.1 L/min water flowrate, carbon paper PTLs.	67
Figure 4.1.7: EIS semicircles of a commercial CCM showing the effects of different cell compressions performed at 0.2 A cm ⁻² . Testing conditions: frequency= 100 mHz to 100 kHz, cell T = 60°C, cell P = 1 bara, 0.1 L/min water flowrate, carbon paper PTLs.	68

Figure 4.1.8: (a) Current-voltage PEMWE cell performance curves for 0.1 L/min and 0.2 L/min water flow rates with (b) their corresponding temperature gradients. Testing conditions: cell T = 60°C, cell P = 1 bara, cell compression= 4 kN, carbon paper PTLs.....	70
Figure 4.1.9: Current-voltage performance curves of PEMWE cell with different PTLs materials. Testing conditions: cell T.= 60°C, cell P.= 1 bara, 0.1 L/min water flowrate.....	71
Figure 4.1.10: EIS semicircles of PEMWE cell showing the effects of different PTLs combinations performed at 0.2 A.cm ⁻² . Testing conditions: frequency= 100 mHz to 100 kHz, cell T = 60°C, cell P = 1 bara, 0.1 L/min water flowrate.	72
Figure 4.1.11: (a) Polarisation curves of PEMWE cell with different cell conditioning and I-V measurement parameters and (b) their corresponding performance profiles throughout the I-V test. Testing conditions: cell T = 60°C, cell P = 1 bara, 0.1 L/min water flowrate, Titanium (Pt-coated) PTLs.....	74
Figure 4.2.1: SEM images of a commercial CCM anode catalyst layer with (a) catalyst layer surface and (b) catalyst layer cross section.....	76
Figure 4.2.2: Current-voltage performance graphs of N115 commercial CCMs from in-house benchmarking results. Testing conditions: cell T = 60°C, cell P = 1 bara, 0.1 L/min water flowrate, Titanium (Pt) PTLs.....	77
Figure 4.2.3: The electrochemical impedance spectra of commercial CCMs conducted at 0 A cm ⁻² . Testing conditions: frequency= 100 mHz to 100 kHz, cell T = 60°C, cell P = 1 bara, 0.1 L/min water flowrate, Titanium (Pt) PTLs.....	78
Figure 5.1.1: SEM images of IrO _x -TiO ₂ anode catalyst layer surface and cross-section obtained from N212 CCM samples without pore formers and with ammonium carbonate at varying pore former to catalyst mass ratio.....	84
Figure 5.1.2: SEM images of IrO _x -TiO ₂ anode electrode surface showing catalyst layer porosity obtained from Nafion 212 CCM samples without pore formers and with ammonium carbonate and ammonium bicarbonate at varying pore forming substance weight ratio.....	86
Figure 5.1.3: Current-voltage performance curves of Nafion 212 CCMs with anode electrode without pore forming additives Testing conditions: cell T = 60°C, cell P = 1 bara, 0.1 L/min water flowrate, Titanium (Pt coated) PTLs.....	88
Figure 5.1.4: Current-voltage performance curves of Nafion 212 CCMs with anode electrode (a) with ammonium carbonate, (b) with ammonium bicarbonate. Testing conditions: cell T = 60°C, cell P = 1 bara, 0.1 L/min water flowrate, Titanium (Pt coated) PTLs.....	89
Figure 5.1.5: Performance of prepared Nafion 212 CCMs samples at current density per mg iridium loading. Testing conditions: cell T = 60°C, cell P = 1 bara, 0.1 L/min water flowrate, Titanium (Pt coated) PTLs.....	90

Figure 5.2.1: SEM images of IrO _x -TiO ₂ anode catalyst layer surface and cross-section obtained from N115 CCMs samples without pore formers and with ammonium bicarbonate at varying pore former to catalyst weight ratios.	93
Figure 5.2.2: SEM images of IrO _x -TiO ₂ anode electrode surface showing catalyst layer porosity obtained from Nafion 115 CCM samples without pore former and with ammonium bicarbonate at varying ammonium to IrO _x -TiO ₂ weight ratios.	95
Figure 5.2.3: Current-voltage performance curves of prepared Nafion 115 CCMs with anode electrode without pore forming additives. Testing conditions: cell T = 60°C, cell P = 1 bara, 0.1 L/min water flowrate, Titanium (Pt coated) PTLs.	97
Figure 5.2.4: (a) Current-voltage performance curves of prepared Nafion 115 CCMs with anode electrode of 1:1 and 1:10 ammonium bicarbonate to IrO _x -TiO ₂ weight ratio. And (b) Performance of all prepared Nafion 115 CCMs samples at current density per mg iridium loading. Testing conditions: cell T = 60°C, cell P = 1 bara, 0.1 L/min water flowrate, Titanium (Pt coated) PTLs.	98

LIST OF TABLES

Table 1.3.1: Main characteristics of different electrolysis technologies (Gahleitner, 2013; Götz, et al., 2016; Schmidt, et al., 2017).....	3
Table 2.4.1: Properties of solvents used in catalysts ink preparation, membrane (swelling ratio), and the resultant electrodes characteristics from Therdthianwong, et al., (2010) study.	19
Table 2.7.1: Summary of research studies on the effects of pore forming substances on the structure and properties of catalyst layers and performance.	32
Table 3.1.1: Wire-wound size selection chart for the Mayer Rod Coater (R.D. Specialities, 2016).	34
Table 3.1.2: Various Mayer rod coater speed values and their corresponding experimental ATO coated layer quality and loading.....	35
Table 3.2.1: Summary of hot-pressing parameters and their effects on the ATO layer transfer.	43
Table 3.3.1: Chemicals and Materials for PEMWE electrodes fabrication.	47
Table 3.4.1: Summary of chemical composition from EDX of the IrO _x -TiO ₂ electrode samples after decal transfer process.....	56
Table 4.1.1: Greenlight innovation electrolyser test station equipment specifications.	61
Table 4.1.2: PEMWE cell specifications.	64
Table 4.1.3: Summary of commercial CCMs with their corresponding cell conditioning and I-V measurement parameters investigated.	75
Table 5.1.1: Summary of anode electrode catalyst layer physical properties for all fabricated N212 CCM samples.....	85
Table 5.1.2: Summary of anode electrode catalyst layer component volume fraction for the prepared Nafion 212 CCM sample.....	87
Table 5.2.1: Summary of anode electrode catalyst layer physical properties for some of the fabricated N115 CCM sample.	93
Table 5.2.2: Summary of anode electrode catalyst layer pore volume fraction for some of the fabricated Nafion 115 CCM samples.....	96
Table 0.1: Abbreviations and descriptions for the process flow diagram of the PEMWE test bench.....	113
Table 0.2: Properties summary of PEMWE electrodes prepared samples using CCM method.	114
Table 0.3: Testing protocols for the catalyst coated membrane samples electrochemical test.	115

NOMENCLATURE

ΔG	Gibb's free energy	J mol^{-1}
ΔH	Enthalpy	J mol^{-1}
ΔS	Entropy	$\text{J mol}^{-1} \text{K}^{-1}$
E°	Standard cell voltage	V
F	Faraday constant	C mol^{-1}
n	Number of electrons formed	

ABBREVIATIONS

ATO	Antimony Doped Tin Oxide
AWE	Alkaline Water Electrolysis
BPP	Bipolar Plate
CCM	Catalyst Coated Membrane
CCS	Catalyst Coated Substrate
CPUT	Cape Peninsula University of Technology
EIS	Electrochemical Impedance Spectroscopy
EGDEE	Ethylene Glycol Diethyl Ether
EGDME	Ethylene Glycol Dimethyl Ether
GDE	Gas Diffusion Electrode
HySA	Hydrogen South Africa
IPA	Isopropyl Alcohol
OCV	Open Circuit Voltage
OER	Oxygen Evolution Reaction
PEM	Proton Exchange Membrane
PEMWE	Proton Exchange Membrane Water Electrolysis
PFSA	Perfluoroalkylsulfonic acid
PGM	Platinum Group Metal
PTL	Porous Transport Layer
RHE	Reversible Hydrogen Electrode
SEM	Scanning Electron Microscopy
SOWE	Solid Oxide Water Electrolysis
TPB	Triple Phase Boundary
UCT	University of Cape Town

GLOSSARY

Anode	Negative electrode where oxidation occurs (Durst, 1997).
Catalyst	Substances that increase the rate of a chemical reaction (Gerardi, 2003).
CCS	Catalyst coated substrate, referring to catalyst coated onto Teflon sheet.
Current Density	Amount of electric current flowing per unit of electrode surface area [$A\ cm^2$] (Garverick, 1994).
Decal	Transfer of the catalyst layer (coated on a substrate) onto a membrane after hot pressing.
Nafion	Membrane ionomer which has an aliphatic perfluorinated backbone with ether linked side chains and sulfonate cation exchange sites at the ends.
Open Circuit Voltage	Maximum voltage reachable by a system at infinite resistance (open circuit mode).

OUTPUTS FROM THIS STUDY

- **Articles Submitted for Publication.**

Jonathan Oumbenga Kiangani, Durgaprasad Madras Rajaraman Iyer, Darija Susac, Mahabubur Chowdhury and Rhiyaad Mohamed. 2022. Effects of the Addition of Inorganic Pore Formers to the Anode Catalyst inks on the Anode Catalyst Layer Morphology and Cell Performance for Proton Exchange Membrane Water Electrolyser.

CHAPTER 1 INTRODUCTION

1.1. An Overview of the Global Energy Sector

For the last seven decades, worldwide primary energy consumption, driven by the growing electrification of most economic sectors (such as transportation, industry, agriculture, and heat), has increased more than 5-fold (Smil, 2017; BP, 2021) and is projected to increase over 50 percent by the end of the mid-century comparative to the year 2010 (International Energy Agency, 2021). In 2020, fossil fuel-based energy resources covered nearly 83.7 percent of the total global primary energy consumption (BP, 2021). However, the dependency of the energy system on fossil fuel is no longer sustainable as these fuels usage accounts for more than 84 percent of global anthropogenic greenhouse gas emissions in 2020 (IPCC, 2021).

While the use of many carbon-neutral energy sources such as bioenergy and geothermal power can mitigate the environmental pollution; renewable energies, particularly solar and wind energies, are the most suitable pathways to reduce anthropogenic greenhouse gas emissions at the required speed and sustain the increasing energy demand (Blanco & Faaij, 2018; IPCC, 2021). However, inherent issues such as fluctuating and intermittent energy outputs associated with the forementioned renewable energy sources require the use of energy storage technologies to compensate for their periodic energy output imbalances (Blanco & Faaij, 2018; Cook, et al., 2010; Schiebahn, et al., 2015).

Energy storage technologies such as supercapacitors and batteries can provide high-capacity storage of renewable energy sources. However, the cyclic, and long-term storage of periodic renewable energy outputs can only be efficiently accomplished by hydrogen as an energy carrier (Blanco & Faaij, 2018; Lewis & Nocera, 2006).

1.2. Hydrogen as Renewable Energy Storage

Hydrogen energy storage is another form of chemical energy storage. In this storage technology, renewable power is chemically converted into hydrogen through water electrolysis and stored (Sterner, 2009; Turner, et al., 2008). And when required, it can be released as fuel for a combustion engine or a fuel cell providing a store of carbon-free energy for dispatch when demand is strongest (Sterner, 2009; Turner, et al., 2008). Besides its long-term storability capacity, electrolytic hydrogen delivers more energy dispatched from storage than other technologies, it can be utilised to transfer renewable energies to transport, heating and many other sectors further contributing to the decarbonization of numerous sectors

(Gahleitner, 2013; Sterner, 2009; Turner, et al., 2008). Hydrogen has the highest energy per mass of any fuel, for example, hydrogen has nearly three times the energy content of gasoline (Pellow, et al., 2015).

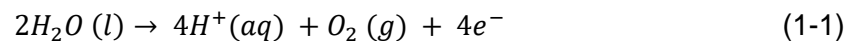
1.3. An Overview of Water Electrolysis

Water electrolysis is the process of splitting water into hydrogen and oxygen molecules using electricity (Pellow, et al., 2015). Water electrolysis is a clean technology, offering remarkable prospects to store long-term large amounts of renewable energy in the form of chemical energy.

1.3.1. Basic Chemistry of Water Electrolysis

The electrochemical splitting of pure water can be illustrated with the following oxidation and reduction half-reactions (Bladergroen, et al., 2012; Millet, et al., 2011):

At the anode (Half-reaction: oxidation):



At the cathode (Half-reaction: reduction):



The water electrolysis process (overall reaction):



In water electrolysis, the anode half-reaction kinetics are significantly slower compared to the cathode half-reaction. (Ghosh & Hasimur Rahaman, 2019).

1.3.1.1. Types of Water Electrolysis Technologies

Water electrolysis technologies are categorised by the operating temperature and the nature of the electrolyte medium. Low temperature alkaline water electrolysis (AWE) has been used for large-scale industrial hydrogen production for over a century (Schmidt, et al., 2017). This technology utilises aqueous sodium hydroxide or potassium hydroxide electrolytes. However, its inability to operate at high current densities and low efficiencies limit its widespread adoption for the production of green hydrogen. Proton exchange membrane water electrolysis (PEMWE), also a low temperature electrolysis process, is based on the utilisation of a proton-conducting polymer membrane as both the electrolyte and separator (Carmo, et al., 2013; Feng, et al., 2017; Schiebahn, et al., 2015).

Solid oxide water electrolysis (SOWE) operates at high temperatures and uses solid oxide electrolytes such as ZrO_2 doped with Y_2O_3 (Schmidt, et al., 2017). The main characteristics of the different types of water electrolysis technologies are summarised in Table 1.3.1.

Table 1.3.1: Main characteristics of different electrolysis technologies (Gahleitner, 2013; Götz, et al., 2016; Schmidt, et al., 2017).

Characteristics	AWE	PEMWE	SOWE
Electrolyte	Liquid alkaline solution	Solid polymer membrane	Ceramic metal compound
Operating Temperature (°C)	40.1 – 90.1	20.1 – 200.1	700.1 – 1000.1
Operating Pressure (kPa)	< 3000	< 20000	101.325
Operating Current Density (A)	0.2 – 0.4	0.6 – 2	0.3 – 2
System Energy (Wh Nm ³)	4500 – 6600	4200 – 6600	3700 – 4700
Voltage Efficiency HHV (%)	62 – 82	67 – 82	< 110
System Response	Seconds	Milliseconds	Seconds
Cold Start Time (Sec)	< 3600	< 1200	< 3600
Lower Dynamic Range (%)	10 – 40	0 – 40	< 30

There are a number of key characteristics, such as operation at low dynamic range, quick system components response which enables dynamic operations, short cold-start times, that are required for an electrolyser system to be paired with fluctuating and intermittent renewable energy sources. PEMWE appears to be the most suitable electrolysis technology for operations with cyclic and intermittent energy sources, as shown in Table 1.3.1.

1.4. Proton Exchange Membrane Water Electrolysis

The PEMWE system was first introduced in the 1950s by W.T. Grubb and developed a decade later by General Electric to overcome the drawbacks of alkaline water electrolysis (Carmo, et al., 2013; Kumar & Himabindu, 2019). This system is based on the utilisation of thin solid proton-conducting polymer electrolyte membranes, replacing the use of liquid electrolytes (Carmo, et al., 2013; Feng, et al., 2017; Schiebahn, et al., 2015).

PEMWE technology has many great advantages such as production of highly compressed and ultrapure hydrogen, flexible operation at high current densities and high system efficiencies (Kumar & Himabindu, 2019).

1.4.1. Basic Principles of the PEMWE

In PEMWEs, electrochemical reactions occur at the anode and cathode electrode catalyst layers (Babic, et al., 2017; Carmo, et al., 2013). Water is circulated in the anode compartment through flow channels to the catalyst layer surface where it is electrochemically split into oxygen molecules, protons (H^+) and electrons (e^-) by applying a direct current (DC) power (Babic, et al., 2017). The produced oxygen molecules exit the process unit along with water at the anode outlet. The solvated protons (H^+) migrate from the anode electrode to the cathode electrode catalyst layer through the proton exchange membrane and combine with electrons, generated at the anode catalyst layer, and circulated by an external electrical circuit, to form hydrogen molecules (Mo, et al., 2016; Turner, et al., 2008). The hydrogen molecules then exit the cell through the cathode outlet.

1.4.2. Challenges of PEMWE

As mentioned above, PEMWE technologies offers many advantages over their alkaline and high temperature counterparts such as high current density operation, high hydrogen product purity, low gas permeability, dynamic and intermittent operations (Feng, et al., 2017; Shen, et al., 2018). However, the commercial use of PEMWE systems for the production of green hydrogen still faces some limitations. One of the main impediments of the PEMWE technology is the requirement of high capital investment. This is due to the indispensable use of expensive and rare noble metals such as ruthenium, iridium for the anode and platinum at the cathode electrodes in high loadings, especially at the anode (Babic, et al., 2017; Carmo, et al., 2013; Grigoriev, et al., 2009). To achieve commercial feasibility of the PEMWE technology, costs improvements of its components need to be conducted (Fouda-Onana, et al., 2016). Furthermore, the development of inexpensive and efficient PEMWE electrodes fabrication processes, and the reduction of noble metal electrocatalyst loadings or their substitution with non noble materials should be explored. (Fouda-Onana, et al., 2016; Grigoriev, et al., 2009; Nie & Chen, 2010).

1.5. Problem Statement

As a part of the South African National Hydrogen and Fuel Cells Technologies Flagship project, the HySA Catalysis Centre of Competence (CoC) is tasked to establish South Africa as one of the main global exporters of electrolyser and fuel cell technologies. This entails but not limited to the development of manufacturing processes for electrocatalysts and other components for fuel cell and electrolyser systems. As mentioned above, the PEMWE technology for the production of hydrogen from renewable energies is still hindered by its high capital expense. One of the factors influencing its high costs is the requisite use of high amounts of noble metals in the electrode catalyst layers. Although much efforts have been devoted into establishing synthesis methods for the production of highly active and durable electrocatalysts to offset the need of high catalyst loadings, little attention has been paid into developing inexpensive, efficient, and easily scalable fabrication processes and electrochemical characterisations for the PEMWE electrodes. Furthermore, considering that the use of high quantity of noble metals is mainly required at the anode electrode, the optimisation of the anode catalyst layer structure can provide a pathway to further lower its electrocatalyst loadings while maintaining or even improving the overall PEMWE system performance. Therefore, research and development of PEMWE electrodes fabrication and testing techniques as well as investigations of the anode catalyst layer structure need to be conducted.

1.6. Objectives

To reduce the capital expenditure, improve the efficiency and durability of the PEMWE system, the anode electrode catalyst layer structure needs to be designed in the way that the electrocatalysts utilisation is optimum and the resistance induced losses are minimised.

To achieve this aim, the following objectives were formulated:

- The development of a comprehensive method for the fabrication of the proton exchange membrane water anode electrode using the Mayer rod coating technique.
- The development of systematic electrochemical characterisation protocols for the evaluation of the PEMWE cell overall in-situ performance.
- Assessing the use of pore forming additives such as $(\text{NH}_4)_2\text{CO}_3$ and NH_4HCO_3 in the anode catalyst ink formulation on the physical and electrochemical properties of the catalyst coated membranes (CCMs).
- The investigation of the effects of the addition of pore forming materials on the physical and electrochemical properties of the anode catalyst layer.

- Understanding the relationship between anode catalyst layer structure, electrocatalyst utilisation and overall PEMWE cell performance.

1.7. Scope of the Study

In this study, the fabrication method and electrochemical characterisation protocols of the PEMWE electrodes were developed. The effects of the addition of pore forming materials on the anode catalyst layer structure and overall PEMWE cell performance were also investigated.

1.8. Significance of the Study

This work will contribute to establishing an efficient and scalable fabrication method and electrochemical characterisation techniques of PEMWE electrodes at the HySA Catalysis CoC. Furthermore, this study could provide information on the manufacturing of highly porous PEMWE electrodes for high current density water electrolysis operations, further improving the cost-competitiveness of PEMWE systems for commercial adoption. This work could also contribute to the understanding of the PEMWE anode catalyst layer structure and its relationship to the overall cell performance.

1.9. Thesis Outline

This thesis comprises the following chapters:

- **Chapter 1: Introduction**

In this Chapter, key information prerequisite to understand the research topic is presented. The background and relevance of this study are provided; and the principles and challenges of the proton exchange membrane water electrolysis system are highlighted. Furthermore, the research objectives are clearly stated and the overall experimental methodology utilised to undertake this study is introduced.

- **Chapter 2: Background Information and Literature Review**

In this Chapter, the fundamental laws relevant to the proton exchange membrane water electrolyser technology and its hardware composition are shown. Published work such as books, scientific articles, and other scholar sources important to the understanding of the PEMWE electrodes fabrication and electrochemical characterisation techniques are critically

assessed and summarised, as well as the structure and properties of the anode electrode catalyst layer.

- **Chapter 3: Development of the Fabrication Method for PEMWE Electrodes**

In Chapter 3, the experimental method set-up, the materials and equipment used to develop the fabrication method of the PEMWE electrodes are described, and various parameters investigated and their findings are presented and discussed.

- **Chapter 4: Development of the Electrochemical Evaluation Protocols for PEMWE Electrodes**

Chapter 4 contains the description of the overall development study of the electrochemical characterisation protocols for the PEMWE electrodes; including the discussion of findings from various testing conditions investigated as well as the equipment and materials used.

- **Chapter 5: Effects of Pore Forming Additives on the Anode Electrodes Catalyst Layer**

In Chapter 5, a comprehensive analysis and discussion of the results obtained from the addition of pore forming materials in the anode electrode catalyst ink formulation are presented.

- **Chapter 6: Conclusion and Recommendations**

In this Chapter, the summary of the main findings of this study is given and a brief research outlook, established from the main findings, is proposed.

CHAPTER 2 BACKGROUND INFORMATION AND LITERATURE REVIEW

To develop a fabrication method and electrochemical evaluation protocols for the proton exchange membrane water electrolysis (PEMWE) electrodes, published work relevant to these topics were reviewed. The summary of the literature survey is presented in this chapter. This review first describes the composition of the PEMWE cell and its fundamental laws to provide a background to the functioning of the PEMWE technology. Evaluation methods for the physical characterisation of the anode electrode catalyst layer structure are also discussed. Lastly, methods of fabrication and electrochemical evaluations of PEMWE electrodes as well as pore forming material types and properties for the fabrication of PEMWE highly porous anode catalyst layers are presented.

2.1. PEMWE Materials and Components

The basic design of a PEMWE cell, with its main components, is shown in Figure 2.1.1. A single PEMWE cell consists of cathode and anode electrodes that are separated by a proton exchange membrane electrolyte (Babic, et al., 2017). Each electrode mainly comprises of a bipolar plate (BPP), porous transport layer (PTL) and an electrocatalyst layer where the respective electrochemical reactions take place (Babic, et al., 2017).

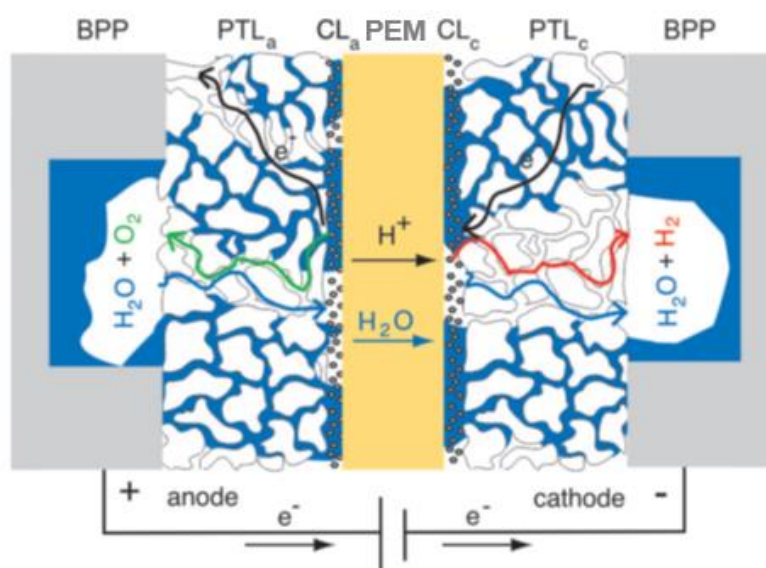


Figure 2.1.1: Schematic illustration of a PEMWE cell. Including a proton exchange membrane (PEM) electrolyte; anode catalyst layer (CL_a) and cathode catalyst layer (CL_c); anodic porous transport layer (PTL_a) and cathodic porous transport layer (PTL_c) and two bipolar plates (Babic, et al., 2017)

2.1.1. Bipolar Plate

Bipolar plates (BPPs) are multifunctional PEMWE components that offer structural support to the cell and allow the compression pressure to be uniformly distributed across the device. Good PEMWE BPPs need to be mechanically stable, possess high electrical and thermal conductivity, and exhibit excellent corrosion resistance (Babic, et al., 2017). Despite their high costs, titanium-based materials are used as standard for BPPs in PEMWE cells because of their high corrosion and oxidation resistance (Babic, et al., 2017). PEMWE BPPs often have surface integrated flow channels that are used to ensure water flows evenly through the PTL and to remove the gaseous products (O_2 and H_2) from the cell and facilitate heat management (Babic, et al., 2017; Feng, et al., 2017).

2.1.2. Porous Transport Layer

Porous transport layers (PTLs) are porous media situated between the catalyst layer and bipolar plate (BPP) at both anode and cathode electrode sides, as shown in Figure 2.1.1. Their main functions are to promote the transport of water, gas, and electrons to and from the electrochemical reaction sites with minimum ohmic, interfacial, and thermal losses (Babic, et al., 2017; Mo, et al., 2016). They also provide mechanical support to the membrane electrolyte (Babic, et al., 2017; Mo, et al., 2016). On the cathode side, carbon fibre-based materials can be used as porous transport layers. However, due to the high electrochemical potential and highly oxidative environment on the anode side, metallic porous transport layer materials such as titanium and stainless steel in the form of sintered powders, fibres or meshes are generally preferred (Babic, et al., 2017; Feng, et al., 2017; Mo, et al., 2016).

2.1.3. Proton Exchange Membrane

The proton exchange membrane (PEM) serves as the electrolyte and ensures the system's electrical insulation and separation of product gases between the anode and cathode electrodes (Babic, et al., 2017; Carmo, et al., 2013). The solid electrolyte makes it possible to have a compact electrolysis system design and enables high pressure operation and high conduction of protons (Babic, et al., 2017; Carmo, et al., 2013). The characteristics of a good proton exchange membrane are chemical and mechanical stability under typical PEMWE operating conditions. Commercial perfluoroalkylsulfonic acid (PFSA) based materials, such as Nafion, Flemion or Aquivion, are used as PEM electrolytes due to their excellent thermal and chemical stability, high proton conductivity, and good mechanical strength (Carmo, et al., 2013).

2.1.4. Electrocatalyst Layer

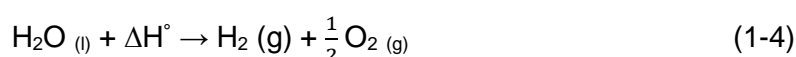
The electrocatalyst layer or catalyst layer (CL) is situated between the PEM and PTL on both the anodic and cathodic sides as shown in Figure 2.1.1. The catalyst layer comprises electrocatalyst particles, proton conducting ionomer and pores (Babic, et al., 2017). In PEMWE applications, electrocatalysts are only selected from the platinum-group-metals (PGMs) due to their high activity and good stability in the harsh electrochemical environment (Babic, et al., 2017). The catalysts are used to help the charge transfer kinetics and decrease the activation energy of the water splitting reaction (Kumar & Himabindu, 2019).

At the cathode electrode, carbon supported platinum-based materials are commonly used as catalysts for the hydrogen evolution reaction (HER) (Babic, et al., 2017). At the anode electrode catalyst layer, iridium oxide and ruthenium oxide show the highest activity for the oxygen evolution reaction (OER) in acidic media (Babic, et al., 2017; Carmo, et al., 2013). However, only iridium-based catalysts have sufficient stability for long-term operations as ruthenium oxide dissolves and corrodes at significantly high OER rates (Babic, et al., 2017; Carmo, et al., 2013). Whereas at the cathode electrode catalyst layer carbon is used as a catalyst support material; oxide and ceramic materials such as TaC, TiC SnO₂, Sb₂O₅, TiO₂ are commonly used as anode catalyst supports due to the OER reaction conditions since carbon readily oxidises under high electrochemical potentials (Babic, et al., 2017; Feng, et al., 2017).

2.2. Principles of PEMWE

2.2.1. Thermodynamics

The electrolysis of water requires a minimum amount of energy input to dissociate water molecules (Babic, et al., 2017; Carmo, et al., 2013). According to the second law of thermodynamics, the standard enthalpy of the reaction ΔH° , the total energy needed for water splitting to occur at 25°C and under atmospheric pressure, is 286.02 kJ mol⁻¹ (Babic, et al., 2017; Kumar & Himabindu, 2019). Equation (1-4) illustrates the overall water splitting reaction with its the standard enthalpy.



The enthalpy (or the heat) of a reaction is the difference between the heats of formation of products and reactants. Hence, for the water splitting reaction (Equation 1-4) the enthalpy of the electrolysis is expressed as (Chen, 2002):

$$\Delta H^{\circ} = (h_f)_{H_2} + \frac{1}{2}(h_f)_{O_2} - (h_f)_{H_2O} \quad (1-5)$$

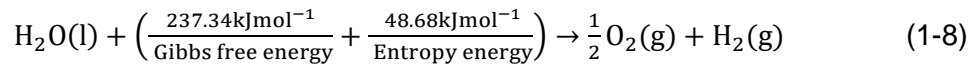
$$\Delta H^{\circ} = 0 + 0 - \left(-286.02 \frac{\text{kJ}}{\text{mol}}\right) = 286.02 \frac{\text{kJ}}{\text{mol}} \quad (1-6)$$

However, due the production of some entropy, only a portion of the reaction enthalpy supplied is used for water electrolysis process (Chen, 2002). Consequently, the standard reaction enthalpy for water splitting, ΔH° , is defined as (Babic, et al., 2017; Bladergroen, et al., 2012):

$$\Delta H^{\circ} = \Delta G^{\circ} + T\Delta S \quad (1-7)$$

Where ΔG° is the standard Gibbs free energy of the reaction, T is the temperature of the reaction and ΔS is the change in entropy of the system.

At standard conditions, the value of the irreversible energy required to compensate the change in entropy $T\Delta S$ is 48.68 kJ mol⁻¹. Thus, the standard Gibbs free energy ΔG° becomes 237.34 kJ mol⁻¹ (Babic, et al., 2017; Bladergroen, et al., 2012; Kumar & Himabindu, 2019). The Equation (1-4) with all the thermodynamic energy values described in Equation (1-7) becomes (Babic, et al., 2017; Kumar & Himabindu, 2019):



Because in PEMWE system the energy input is supplied as an electrical energy, the value of the enthalpy of the reaction is used as a measure of the electrical energy required for the electrochemical splitting of water (Chen, 2002). The theoretical reversible cell voltage E_{rev}° corresponding to the standard Gibbs free energy ΔG° , the minimum electrical energy required for water electrolysis at standard conditions, is about 1.23 V and is given by the Equation (1-9) (Babic, et al., 2017; Bladergroen, et al., 2012; Kumar & Himabindu, 2019):

$$E_{rev}^{\circ} = \left| \frac{\Delta G^{\circ}}{nF} \right| = \frac{237,340}{2 \times 96,485} \frac{\text{J mol}^{-1}}{\text{Coulombs mol}^{-1}} = 1.23 \text{ Volts} \quad (1-9)$$

And the theoretical (thermoneutral) cell voltage corresponding to the enthalpy of the reaction, the total energy required for water splitting at standard conditions, is about 1.482 V and given by the following Equation (1-10) (Babic, et al., 2017):

$$E_{\text{TN}}^{\circ} = \left| \frac{\Delta H^{\circ}}{nF} \right| = \frac{286,020}{2 \times 96,485} \frac{\text{J mol}^{-1}}{\text{Coulombs mol}^{-1}} = 1.482 \text{ Volts} \quad (1-10)$$

Where:

n = number of transferred electrons in the reaction

F = Faraday constant (96,485 Coulombs mol⁻¹)

E_{rev}° = Reversible cell voltage

E_{TN}° = Thermoneutral or total cell voltage

The reversible voltages of individual electrode (anode and cathode) are estimated using the Nernst equation and considering the activity coefficients, temperature, and pressure of each product molecule at standard conditions (Babic, et al., 2017):

At the anode

$$E_{\text{rev(OER)}}^{\circ} = E^{*\circ} + \frac{RT}{nF} \ln \left(\frac{a(\text{H}^+)^2 \sqrt{a(\text{O}_2)}}{a(\text{H}_2\text{O})} \right) = 1.23 \text{ Volts} \quad (\text{vs. RHE}) \quad (1-11)$$

At the cathode

$$E_{\text{rev(HER)}}^{\circ} = E^{*\circ} + \frac{RT}{nF} \ln \left(\frac{a(\text{H}^+)^2}{a(\text{H}_2)} \right) = 0 \text{ Volts} \quad (\text{vs. RHE}) \quad (1-12)$$

Where a is the activity coefficient of the respective molecule and RHE is the reversible hydrogen electrode.

2.2.2. Kinetics – Current Density

The current density is referred to the current, resulting from the flow of electrons, normalised to the unit area of electrode surface (Carmo, et al., 2013). Faraday's Law demonstrates that the current density is proportionally equal to the charge transferred and the consumption of reactant per unit area (Newman, 2012):

$$i = nFj \quad (1-13)$$

Where j is the flux of reactant per unit area in mol/s.cm² and nF is the charge transferred in coulombs/mol).

In other words, the hydrogen output rate of the PEMWE system is directly proportional to the current density applied to that system (Babic, et al., 2017; Newman, 2012).

2.3. PEMWE Voltage Losses

The thermoneutral voltage (Equation 1-10) which corresponds to the energy required to split water into O₂ and H₂ at 100% thermal efficiency does not take into account voltage losses occurring in PEMWE system when external current is applied (Babic, et al., 2017; Cook, et al., 2010; Shen, et al., 2011). In a real-world PEMWE system, excess voltages must be added to the theoretical thermodynamic cell voltage value ($E_{TN}^{\circ} = 1.482$ Volts). This corresponds to the total energy required to produce hydrogen at practical and economical viable reaction rates through water electrolysis. The different voltage losses are caused by the following factors (Babic, et al., 2017; Bladergroen, et al., 2012):

- Kinetics barrier to electrochemical reactions.
- Internal electron and proton conduction resistance.
- Resistance of the reactant and product transport from/to the catalyst particle sites.

The operational cell voltage, V_{CELL} , of the PEMWE system can be determined by adding the contributions of different voltage losses to the theoretical thermodynamic cell voltage (Bladergroen, et al., 2012; Carmo, et al., 2013):

$$V_{CELL} = E_{TN}^{\circ} + \Delta V_{act} + \Delta V_{ohm} + \Delta V_c \quad (1-14)$$

Where E_{TN}° is the theoretical cell voltage corresponding to the enthalpy of the reaction and sometimes referred to as the open circuit voltage (OCV); ΔV_{act} is the activation overvoltage; ΔV_{ohm} is the ohmic overvoltage; and ΔV_c is the concentration overvoltage.

2.3.1. Activation Overvoltage

The activation overvoltage or the kinetic overvoltage represents the voltage required to overcome losses due to inherent kinetic barriers to the electrochemical half-reactions occurring at the anode and cathode electrode interface, respectively (Bladergroen, et al., 2012; Carmo, et al., 2013). The activation voltage can be described as the amount of kinetic energy required to start the water splitting reaction (Bladergroen, et al., 2012; Carmo, et al., 2013). The activation overvoltage is the inherent property of the electrocatalysts utilised in the

PEMWE electrodes catalyst layers (Bladergroen, et al., 2012; Carmo, et al., 2013). The activation overvoltage is directly affected by the temperature of the PEMWE system and the electrode catalyst layer properties such as catalyst type, catalyst loading, catalyst utilisation, number of electrochemical active sites. The activation overvoltage can be determined using the Tafel law (Carmo, et al., 2013):

$$\eta = a + b \log(j) \quad (1-15)$$

where parameter a is the activity of the electrode, b relate to the mechanism of the electrode reaction and j represents the current density of the system.

At high current densities ($\geq 1 \text{ A cm}^{-2}$) most of the activation overvoltage originates from the oxygen evolution reaction (OER) kinetics at the anode electrode catalyst layer. The kinetics for the OER are orders of magnitude slower, resulting in substantial activation overpotentials whereas the hydrogen evolution reaction (HER) at the cathode electrode exhibits fast kinetics at these current densities (Carmo, et al., 2013). Hence, high reaction rates can be obtained at very low overpotentials at the cathode electrode catalyst layer (Carmo, et al., 2013). The OER is the dominant water electrolysis reaction and plays a significant role in determining the PEMWE system performance in the activation region of the electrochemical water splitting process (Carmo, et al., 2013).

2.3.2. Ohmic Overvoltage

The ohmic overvoltage represents the voltage required to subdue voltage losses due to flow resistance during the PEMWE process (Carmo, et al., 2013). Ohmic losses in the PEMWE system can be classified into proton transport resistance of the membrane induced losses called ionic losses and electrical resistance induced losses called electric losses, mostly due to the bipolar plate flow-fields and the porous transport layer interfacial contact (PTL) (Bladergroen, et al., 2012; Carmo, et al., 2013). Properties such as membrane thickness and ionic conductivity as well as the contact resistance between the PEMWE components, the cell compression pressure, and the electronic conductivity of the PTL are some key factors that play a role in determining the ohmic overvoltage (Bladergroen, et al., 2012; Carmo, et al., 2013). The total ohmic resistance of the PEMWE is typically quantified by the high frequency resistance, R_{HFR} , which can be measured using the electrochemical impedance spectroscopy (EIS) (Carmo, et al., 2013). The high frequency resistance, R_{HFR} , is expressed with the following equation:

$$R_{\text{HFR}} = R_{\text{memb}} + R_{\text{el}} \quad (1-16)$$

Where R_{memb} is the ionic resistance and R_{el} is the electrical resistance

The voltage losses due to the proton transport resistance of the membrane can account for the majority of the ohmic overvoltage under high current density operation (Carmo, et al., 2013). This can be lowered by utilising thinner membranes; however, this will cause an increase in hydrogen permeation (also called hydrogen crossover) through the membrane, resulting in a lower faradaic efficiency (Carmo, et al., 2013). The membrane proton conductivity, in the case of a single PEMWE cell, is the single most dominant factor to influence PEMWE performance in the ohmic region of the electrochemical water splitting process (Carmo, et al., 2013).

2.3.3. Concentration Overvoltage

The concentration overvoltage represents the voltage required to overcome losses due to the mass transport resistance of reactant and/or products to/from the electrode catalyst active sites (Bladergroen, et al., 2012; Carmo, et al., 2013). The mass transport resistance can add large voltage losses as reported by Suermann et al. (2015), who investigated various voltage losses for the PEMWE system. In the PEMWE system, liquid water is supplied to the anode catalyst layer where oxygen is evolved (OER), meaning that the water and gas are moving in counter-flow in relation to the membrane. While at the cathode catalyst layer, hydrogen and liquid water is transported by the electro-osmotic drag results in a co-flow configuration (Bladergroen, et al., 2012). It is therefore clear to consider the two-phase transport issues at the anode catalyst layer, where a more complex behaviour is expected due to the counter-flow situation as shown in Figure 2.3.1 (Bladergroen, et al., 2012; Carmo, et al., 2013; Bernt & Gasteiger, 2016).

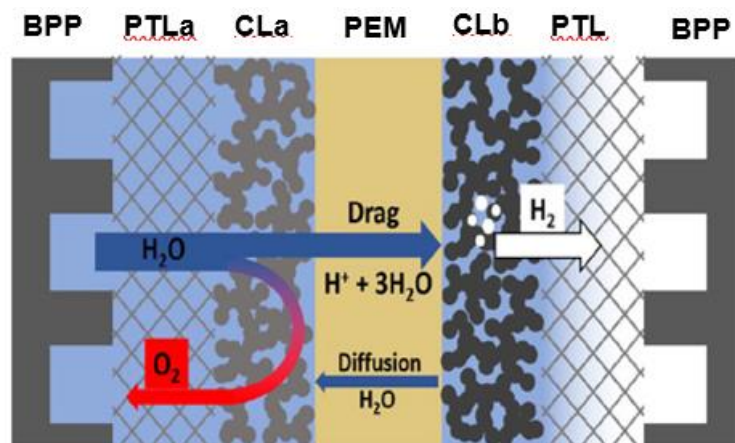


Figure 2.3.1: Schematic diagram illustrating the transport of reactants and products transport in the PEMWE single cell (Bernt & Gasteiger, 2016).

Generally, the concentration overvoltage depends on the structure of the catalyst layer (Carmo, et al., 2013). Catalyst layer properties such as thickness, porosity (pore type, pore size, pore quantity, and pore distribution) determine the concentration overvoltage in the mass transport region of the electrochemical water splitting process (Bladergroen, et al., 2012; Carmo, et al., 2013). This shows that optimisation of catalyst layers is critical to the impact of mass transport limitations in the PEMWE system. An optimised electrode catalyst layer structure can greatly reduce the contribution of mass transport losses thus making the overall operational cell overvoltage almost negligible even at relatively high current density operation (Bladergroen, et al., 2012; Carmo, et al., 2013; Merwe, et al., 2014). Figure 2.3.2 shows the main causes of voltage loss causes at different current density regions.

At high current densities ($\geq 1 \text{ A cm}^2$), mass transport losses can contribute up to 25 percent of the total operational cell overvoltage (Bladergroen, et al., 2012; Carmo, et al., 2013). The anode electrode performance is affected by mass transport limitations due to the high diffusion of gaseous oxygen products and water transport inside the pores of catalyst layers (Bladergroen, et al., 2012; Carmo, et al., 2013). Hence, it is important to ensure effective two-phase transport (liquid reactant-gaseous product) inside the anode electrode catalyst layers (Bladergroen, et al., 2012; Carmo, et al., 2013).

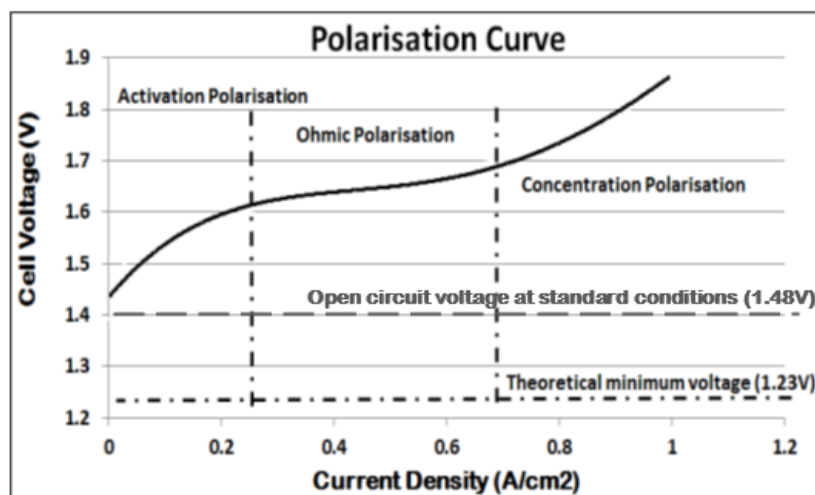


Figure 2.3.2: Conceptual representation of performance influencing PEMWE electrode properties in the activation, ohmic, and mass transport regions of an electrolyser polarization curve (Merwe, et al., 2014).

The overall performance of the PEMWE system is limited by various resistances of the PEMWE cell (Cook, et al., 2010; Maximilian & Gasteiger, 2016). One of primary challenges for PEMWE technology development is to improve the anode electrode catalyst layer to enable

high hydrogen output rates while minimising the magnitude of the overvoltage to the extent that the operational cell voltage approaches the theoretical cell voltage value ($E_{\text{TN}}^{\circ} = 1.482$ Volts) (Cook, et al., 2010; Maximilian & Gasteiger, 2016; Shen, et al., 2011).

2.4. An Overview of the PEMWE Electrodes Fabrication

The catalyst layers structures and properties of PEMWE cathode and anode electrodes depend significantly on their fabrication method (Bladergroen, et al., 2012). Two types of methods can be used to fabricate PEMWE electrodes. The gas diffusion electrode or porous transport electrode (GDE/PTE) method where the catalyst ink is deposited directly on an electrically conductive porous support; and the catalyst coated membrane (CCM) method where the catalyst layer is applied directly or indirectly (through a decal transfer) on the surface of the proton conductive membrane (Bladergroen, et al., 2012; Firtina, et al., 2011). PEMWE electrodes prepared by the CCM method provide higher current densities due to an extended catalyst-ionomer interface and improved catalyst utilisation (Bladergroen, et al., 2012).

2.4.1. PEMWE Catalyst Ink Formulation

The catalyst ink is a well-stirred mixture of electrocatalyst nanoparticles, ionomer, and solvent (Bladergroen, et al., 2012; Firtina, et al., 2011).

2.4.1.1. Ionomer

The addition of ionomer to the catalyst ink promotes the transport of protons from the catalyst layer to the membrane (Carmo, et al., 2013; Dixit, et al., 2018). The ionomer also acts as a binder providing stable catalyst layer structure (Bladergroen, et al., 2012; Firtina, et al., 2011). The ionomer is composed of a carbon fluorine hydrophobic backbone and a hydrophilic side chain. In practice, the ionomer solution tends to form a colloid structure when dispersed in a solvent (Dixit, et al., 2018).

2.4.1.2. Solvent

The solvent used in the catalyst ink formulation plays a major role as it affects the formation of the proton conduction network (Therdthianwong, et al., 2010). Johnston et al., (2009) reported that PEMFC electrodes fabricated with ionomer dispersed in glycerol-based solvent showed a lower performance compared to water-propanol/isopropanol solvent.

This is due to the solvent's physical properties such as dielectric constants and boiling points (Therdthianwong, et al., 2010). Table 2.4.1 summarised findings from Therdthianwong, et al., (2010) showing the effects of different solvents used in the catalyst ink formulation on PEMFC electrodes catalyst layers qualities and cell performance.

Table 2.4.1: Properties of solvents used in catalysts ink preparation, membrane (swelling ratio), and the resultant electrodes characteristics from Therdthianwong, et al., (2010) study.

Solvent	Boiling Point (°C)	Viscosity (cP)	Dielectric Constant	Swelling Ratio (%)	Transmittance (%)	Surface Quality	Power Density (mW cm ⁻²)	Performance Ranking
Isopropanol	82	2.1	18.3	199	0.0 ± 0.002	Smooth	442	1
Acetone	56	0.31	20.7	154	0.121 ± 0.002	Cracked	301	3
Deionised Water	100	0.89	80.4	39	0.266 ± 0.002	Cracked	268	4
Ethylene Glycol	197,3	16.1	37	83	0.263 ± 0.002	Cracked	294 ^b	5
EGDME	85	0.46	7.2	110	0.122 ± 0.002	Cracked	213	6
EGDEE	121,4	0.7	3.8	75	0,136 ± 0.002	Cracked and Poor Adhesion	200	6

^b Higher power density than deionised water but its performance reduced rapidly in the high current density region.

2.4.2. PEMWE Catalyst Ink Mixing Methods

There are many demonstrated methods describing the mixing of PEMFC and direct methanol cell catalyst inks that are also applicable to PEMWE catalyst ink formulation. The most used laboratory dispersion techniques are shear stirring, ultrasonication, and ball milling (Paipetis & Kostopoulos, 2013).

2.4.2.1. High Shear Mixing

High shear mixing is commonly used as a high intensity mixing method in applications where low speed agitation is not suitable such as dispersing solids into liquids, emulsifying liquids, breaking down aggregates (Handbook, 2003; Ross, 2015). High shear mixing uses motors that work between 3 600 to 10 000 rpm; this is achieved via hydraulic forces (Handbook, 2003). A typical example of a high shear machine is a high-speed disk disperser, as seen in Figure 2.4.1. This machine consists of a circular-saw-type disk mounted onto a vertical shaft (Ross, 2015).

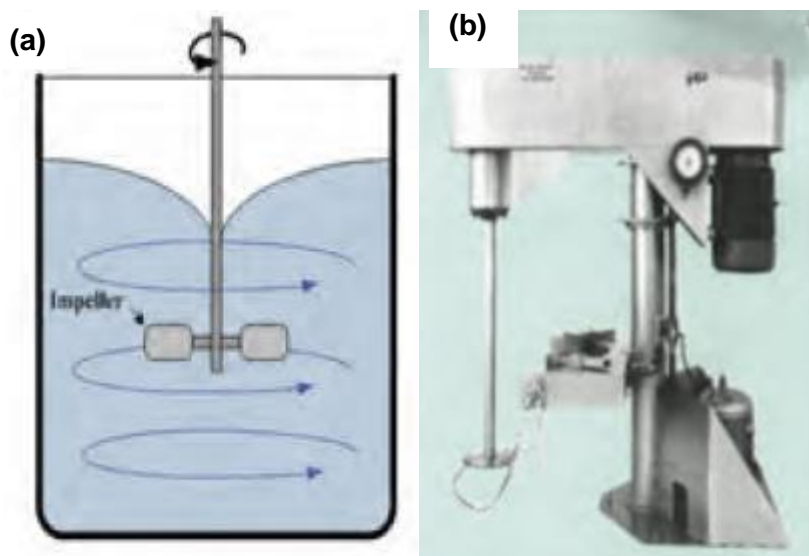


Figure 2.4.1: (a) Image of a High Shear Mixer. (b) Schematic diagram of the high shear mixing mechanism (Ross, 2015).

2.4.2.2. Ultrasonication

Ultrasonication is a well-established mixing method for the production of nanomaterial slurries, dispersions, and emulsions due to its potential in the de-agglomeration and the reduction of primary particles (Hielscher, 2007). This method uses sound waves with a frequency higher than 16 kHz (Conley, 1996) and can be used to accelerate chemical reactions by the cavitation energy, enhance nano-scale dispersion by destroying agglomerates (Ryu, et al., 2001). During high ultrasonication, sound waves spread into the liquid media resulting in compression and refraction cycles (Hielscher, 2007). An ultrasonic device consists of transducers vibrating at certain frequencies. A simple schematic diagram of an ultrasonic device setup is shown in Figure 2.4.2.

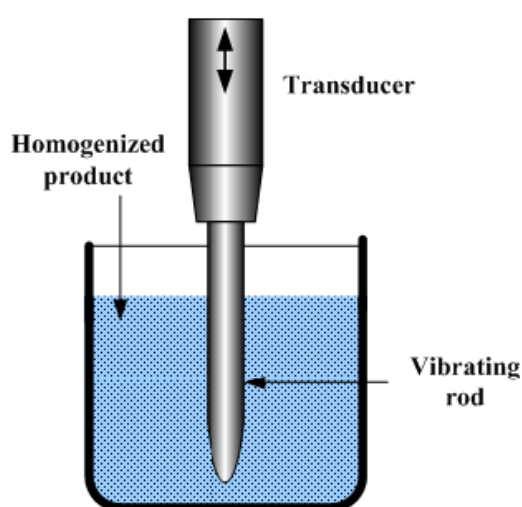


Figure 2.4.2: Schematic of an ultrasonic device with all the basic components (Kopeliovich, 2015).

2.4.2.3. Ball Milling

Milling is primarily used to reduce the size of solids suspended in fluids (Burmeister & Kwade, 2013). Ball Mill (also commonly named bead mill or pearl mill) is a type of size reduction process which produces high impact milling (Burmeister & Kwade, 2013). The working principle and key mechanism behind the ball milling method is shown in Figure 2.4.3. The dispersion matrix is rotated, producing collisional and frictional forces of the tumbling mill balls which results in breaking catalyst agglomerates (Paipetis & Kostopoulos, 2013), thereby decreasing the particle size, changing the particle shape, and increasing the surface area of the materials (Burmeister & Kwade, 2013). Zirconia balls are usually used due to their hardness and fracture resistance compared to the catalyst material (Burmeister & Kwade, 2013).

High energy ball milling assures a vital role in the synthesis of the catalyst inks, increasing the interfacial surface area of substrate and catalyst material while promoting the proper distribution of the catalyst (Burmeister & Kwade, 2013; Paipetis & Kostopoulos, 2013).

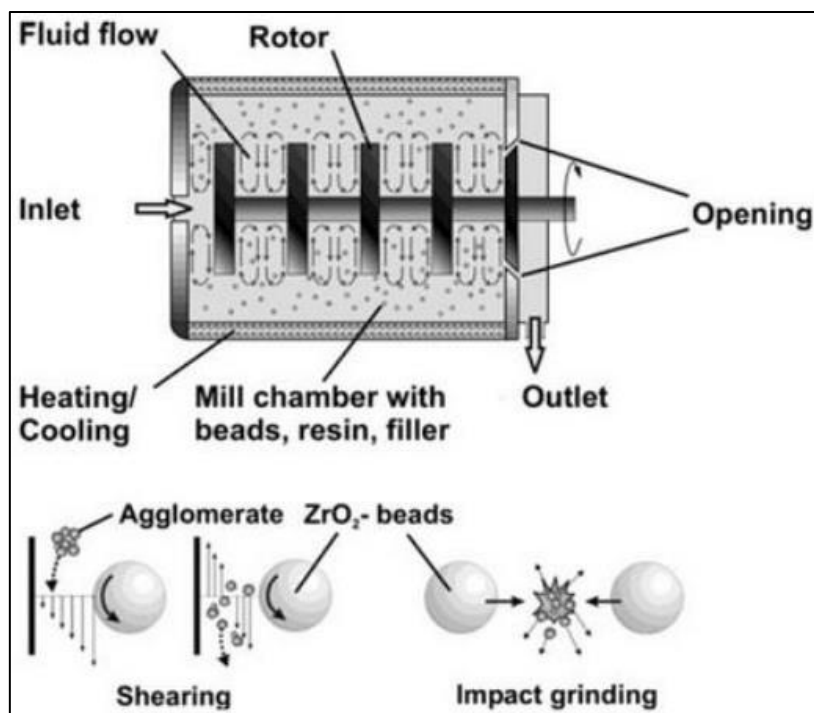


Figure 2.4.3: Image of a ball mill and diagram of its main operating mechanisms (Paipetis & Kostopoulos, 2013).

2.4.3. PEMWE Catalyst Ink Coating Methods

There are several documented methods describing the deposition of the catalyst ink onto a substrate (PTL, proton conductive membrane, Teflon). Published work shows numerous coating methods suitable for PEMWE catalyst ink coating such as ion-bean assisted deposition, inkjet printing, electro-spraying, sputter deposition. However, in this section we provide an overview of commonly used PEMWE electrodes fabrication methods at the laboratory scale.

2.4.3.1. Screen Printing

Screen printing is a well-known coating technique that has been used to deposit conductive pastes for many decades in the field of printed circuit boards (Santangelo, et al., 2019).

In screen printing, the ink in the form of highly viscous liquid is poured onto the surface of a screen fixed to the edges of a frame (Santangelo, et al., 2019). In comparison to other coating methods, screen printing is a less accurate coating method due to the feature sizes of its printed lines which are very high resulting in low print resolution (Santangelo, et al., 2019).

2.4.3.2. Ultrasonic Spray

Ultrasonic spray is widely used coating method for catalyst in the PEMFC technology due to its capability to produce ultra-low catalyst loadings and to operate a broad range of fluids rheology (Aziz & Ismail, 2015). In the ultrasonic spray method, coatings are done by forcing the ink solution through a nozzle whereby a fine aerosol is formed and splashed onto the substrate surface (Aziz & Ismail, 2015).

2.4.3.3. Mayer Rod Coating

Wire-wound rod coating, often called Mayer rod coating after its inventor Charles Mayer, is the simplest thin-film method used to apply accurate and repeatable layers of ink onto most substrates (O'Kane, 2017). The coating technique works by placing a wire-wound rod at fixed distance from the substrate surface that needs to be covered (Anette, et al., 2004; Cherrington & Liang, 2016). When a stable movement is established between the wire-wound rod and the substrate, the coating solution is then placed in front of the rod and spreads on the substrate surface creating a highly uniform wet thin film (Anette, et al., 2004; Cherrington & Liang, 2016). The Mayer rod coating method can operate at various speeds and is suitable for coating substrates with wide range of wet film thicknesses (Anette, et al., 2004; Cherrington & Liang, 2016). Gaps made between the wire and the substrate determine how much the coating solution is allowed through thus the film thickness (Anette, et al., 2004). The final thickness of the wet film will be influenced by the speed of coating and the physical properties of the coating solution (Anette, et al., 2004; Cherrington & Liang, 2016).

The scalability and simplicity of the Mayer rod coating method make it attractive for both manufacturing and research sectors (Anette, et al., 2004; Cherrington & Liang, 2016). Additionally, this method is easily adaptable which makes it ideal for the PEMWE electrodes fabrication (Cherrington & Liang, 2016).

2.4.4. Decal Transfer and Hot Pressing

The decal transfer is the most commonly used CCM method to deposit the catalyst layer in solid form on either side of the proton exchange membrane electrolyte (Firtina, et al., 2011).

In this approach, the catalyst ink is coated onto a decal (the widely used decal material is Teflon or fiberglass reinforced Teflon) then transferred to the proton conductive membrane by hot pressing (Firtina, et al., 2011). The decal material is then peeled away to leave the proton conductive membrane with the catalyst layer (Firtina, et al., 2011). The main challenge for the decal transfer method is to ensure complete catalyst layer transfer without significant residual catalyst material remaining on the decal material.

2.5. PEMWE Anode Electrode Catalyst Layer

The PEMWE anode electrode is comprised of thin catalyst layers, 10 to 100 μm thick (Carmo, et al., 2013). The performance of the PEMWE anode electrode is determined by the properties of its components; mainly by its catalyst layer structure (Feng, et al., 2017). The anode electrode catalyst layer is one of the most important components in the PEMWE technology as it is the location where the electrochemical driving reaction, OER, occurs (Zhang, et al., 2008).

2.5.1. Anode Catalyst Layer Structure

The anode catalyst layer, similar to the cathode catalyst layer, is mainly composed of catalyst particles and perfluorosulfonic acid ionomer (Feng, et al., 2017; Zhang, et al., 2008). The electrochemical reaction at the anode catalyst layer only takes place at confined spatial sites named triple-phase boundaries (TPB), as shown in Figure 2.5.1 (Feng, et al., 2017). This is because the TPB is the only place that allows all three species (water reactant, ionomer, and electrocatalyst particles) that participate in the OER to come into contact with one another (refer to Figure 2.5.1) (Bladergroen, et al., 2012; Zhang, et al., 2008).

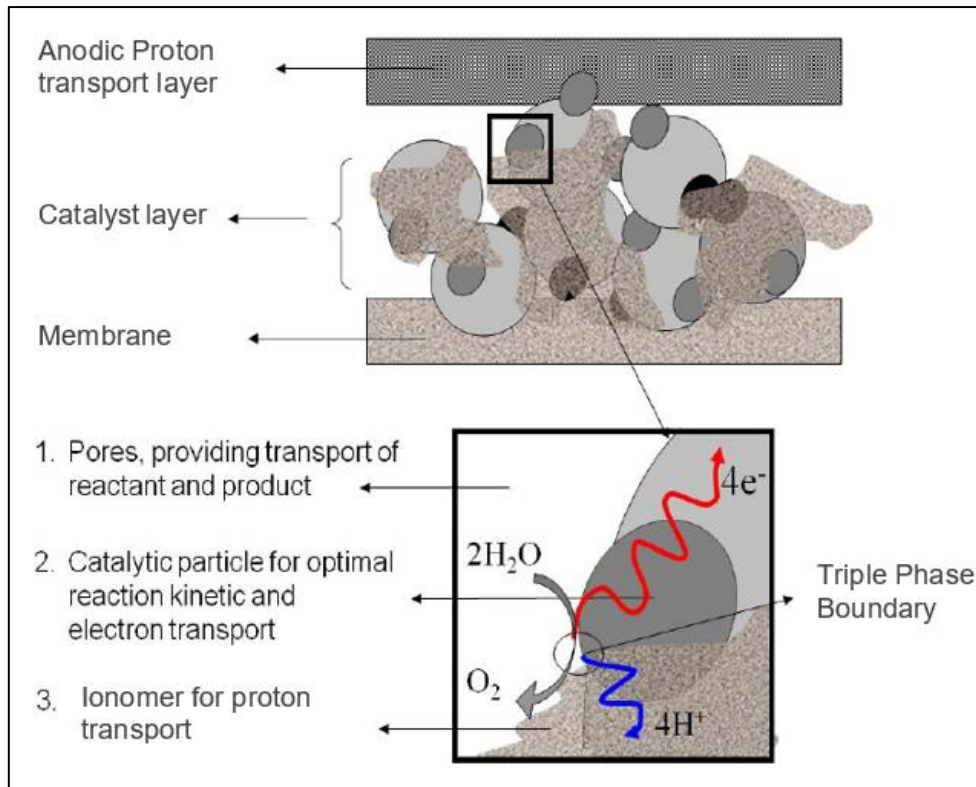


Figure 2.5.1: An overview of the anode electrode catalyst layer triple-phase boundary (Bladergroen, et al., 2012).

A good anode catalyst layer structure must assure (Bladergroen, et al., 2012; Zhang, et al., 2008):

- A path of sufficient voids (catalyst layer pores) is available to allow a continuous flow of water to the anode electrode catalyst sites, and to effectively remove product oxygen, which, if accumulated would prevent water molecules access to catalyst sites.
- A path of sufficient electrically conductive solids running from the anode electrode catalyst particle to the porous transport layer (PTL) surface is available to move electrons from the anode to the PTL layer.
- And concurrently, a path with sufficient proton conductivity is available to transport hydrogen cations from the anode catalyst particle, through the membrane, to the cathode catalyst particles so that the electrons and protons liberated at the anode catalyst active sites in accordance with Equation (1-1) find their way to the cathode catalyst active sites to recombine in accordance with Equation (1-2).

2.5.2. Anode Catalyst Layer Properties

The rate of the water electrolysis reaction depends on the properties of the catalyst layer properties. An ideal PEMWE catalyst layer should maximise the active surface area per unit mass of the electrocatalyst and minimize the obstacles for the oxygen removal from the cell (Feng, et al., 2017; Zhang, et al., 2008). Some of the most important properties of the PEMWE anode electrode catalyst layer include electronic and protonic conductivities, number and size of active reaction sites, and porosity (Zhang, et al., 2008). Making appropriate changes to the catalyst layer structure has proven to be an effective way to minimise transport resistances within the electrode catalyst layers and improve the overall performance at high current density operation in PEMFCs (Shen, et al., 2011; Zhao, et al., 2007).

Theoretically, one way to minimise the transport resistance in a PEMWE system is to introduce an increased range of appropriate porosities into the electrodes catalyst layers to allow for better mass transport within the catalyst layers (Song, et al., 2005). Highly porous electrodes exhibit greatly enhanced mass transport profile relative to smooth surface ones (Fischer, et al., 1998). One method to increase the porosity (pore size, pore quantity and distribution) in the catalyst layer is to add pore forming materials into the electrocatalyst-ionomer ink formulation (Song, et al., 2005; Zhao, et al., 2007).

2.6. An Overview of the PEMWE Electrodes Evaluation

2.6.1. Physical Characterisations

2.6.1.1. Scanning Electron Microscopy

Scanning electron microscopy (SEM) is used to produce vivid images of the topography of a sample's surface as shown in Figure 2.6.1. The images generated can provide important information such the morphological characteristics, the general size of tested component molecule agglomerates, surface variations of the sample (Xie, et al., 2004; Yu, et al., 2019). The functional principle of the SEM characterisation method is based on the fact that the electrons emitted from the electron source, accelerated to keV energies, are directed by several electromagnetic lenses towards the surface of the sample (Yu, et al., 2019). In the SEM method an electron beam with a wavelength of 0.12 Angstroms is shot across the sample surface (Yu, et al., 2019), interacting with the sample atoms, and produce various signals among which are secondary (SE) and backscattered (BSE) electrons (Xie, et al., 2004). The simultaneous detection of SEs and BSEs allows one to obtain the desired morphological

information. SE are essential for analysing of the sample's topography as they are collected from the first tenths of the nm area of the subsurface (Yu, et al., 2019).

BSEs are emitted from the deeper layers within the sample (i.e., 100-1,000 nm range) and are sensitive to the sample composition (Kúš, 2019). The secondary electron (SE) comes from surface regions of the analysed sample while backscattered electron (BSE) originates from deeper regions (Xie, et al., 2004). BSE images display high sensitivity to sample atomic number; the higher the atomic number, the brighter the material appears in the image (Kúš, 2019).

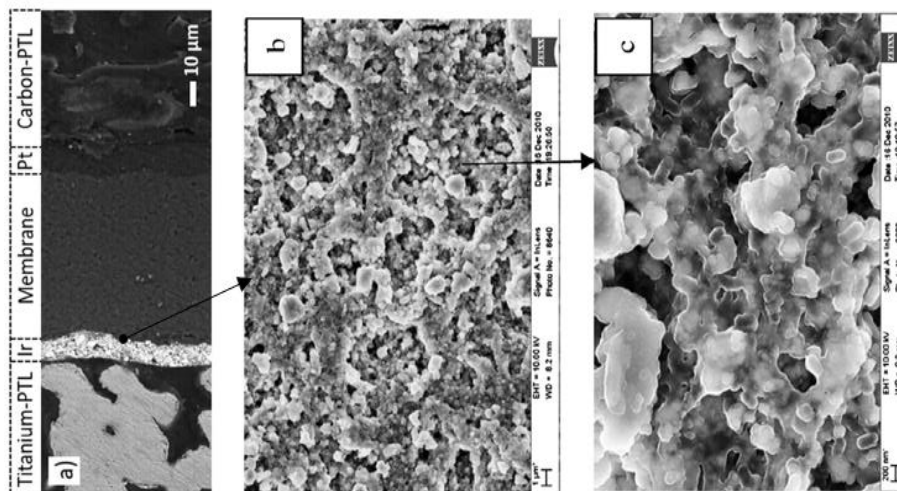


Figure 2.6.1: SEM image of PEMWE components with (Xu, et al., 2011): (a) From bottom to top, a cross-sectional image of anode PTL (titanium sintered), anode electrode catalyst layer composed of electrocatalyst particles and ionomer, membrane, cathode electrode composed of electrocatalyst particles and ionomer, cathode PTL (carbon paper). (b) & (c) Top view of the anode electrode catalyst layer at different image magnification.

In PEMWE, SEM measurements are typically performed to analyse an electrodes surface and cross-section which provide information on the electrode catalyst layer's physical properties and structure such as catalyst layer thickness, porosity distribution and degree of contact between membrane and electrode catalyst layer (Pasupathi, et al., 2015; Xie, et al., 2004; Yu, et al., 2019).

2.6.1.2. Energy Dispersive X-Ray Spectroscopy

Energy dispersive X-ray spectroscopy (EDX) is a standard technique used for the analysis of elemental composition and quantification of materials. Typically, EDX systems come attached to an electron microscopy such as an SEM or transmission electron microscope (TEM) (Colpan, et al., 2018; Ebnesajjad, 2004).

The EDX method relies on the emission of characteristic X-rays, that shows the composition of the elements present in the investigated sample (Colpan, et al., 2018). A high energy beam of charged electrons are focused into the tested element and emitting specific wavelengths of X-rays from the atoms on the surface that are a unique characteristic of the atomic structure of the investigated sample (Colpan, et al., 2018; Ebnesajjad, 2004). A photon-energy-sensitive detector then analyses these X-ray emissions and provides a spectrum of peaks correlated to the elemental surface composition of the tested sample (Ebnesajjad, 2004).

2.6.2. Electrochemical Characterisations

2.6.2.1. Current – Voltage Performance

The current – voltage performance measurement, also called polarisation curve, of the PEMWE electrodes is an in-situ electrolysis evaluation (Lettenmeier, et al., 2017). Since the polarisation performance depends on the temperature, the PEMWE cell must be kept at constant temperature by circulating water (with a minimum resistance of 1 M Ω cm) at the same temperature and at controlled flow rate (usually 0.02 L min⁻¹ to 0.2 L min⁻¹) through the PEMWE flow channels (Lettenmeier, et al., 2017). The performance of the PEMWE cell is characterised by applying incrementally different currents while recording their corresponding voltage values (Lettenmeier, et al., 2017). The current-voltage measurement is useful to identify important PEMWE system parameters such as feasible system current densities (Lettenmeier, et al., 2017). However, the polarisation curve provides no information about the system induced overvoltage (Lettenmeier, et al., 2017).

2.6.2.2. Electrochemical Impedance Spectroscopy

The electrochemical impedance spectroscopy (EIS) is a well-known diagnostic tool commonly used for the voltage resistance characterisation of both PEMFC and PEMWE components (Millet, et al., 2011; Orazem & Tribollet, 2008). The functional principle of EIS is based on applying, in the galvanostatic operation mode a small alternating current (AC), in addition to the operational direct current (DC), as a perturbation signal with known amplitude and frequency while measuring the voltage signal response, as a function of frequency

dependence of the impedance, including amplitude and phase (Bruce, et al., 1994; Dhirde, et al., 2010; Orazem & Tribollet, 2008). Whereas, in the potentiostatic operation mode, the voltage is applied, and the alternating current (AC) signal response is measured (Bruce, et al., 1994; Dhirde, et al., 2010). The frequency dependence of the impedance Z in galvanostatic mode can also be calculated by dividing the voltage by the current (Dhirde, et al., 2010).

$$Z(f) = \frac{U_{AC}(f)}{I_{AC}(f)} = |Z(f)| * e^{i\theta(f)} \quad (1-17)$$

The EIS characterisation perturbation can be measured over a wide range of frequencies (Bruce, et al., 1994). In PEMWE system, EIS measurements are preferentially performed in the frequency range of 0.1 – 10⁶ Hz and require the use of a four-electrode measurement configuration consisting of a working electrode, a counter electrode and two reference electrodes (Dhirde, et al., 2010; Millet, et al., 2011). This dynamic operation enables the observation of time degradation processes such as the double layer charging, charge transfer, interfacial capacitance as well as gas and water diffusion within the cell. Since it is a non-destructive and non-invasive technique, EIS can show, in the frequency domain, the various PEMWE losses associated with each component (Bruce, et al., 1994; Dhirde, et al., 2010; Latham, 2004). Those losses include the activation, ohmic and mass transport losses as aforementioned (Bruce, et al., 1994; Dhirde, et al., 2010; Malkow, et al., 2018).

A typical electrochemical reaction equivalent circuit of electroactive particles is simplified to Randles circuit, as shown in Figure 2.6.2a. Where R_S is the membrane resistance, C_{DL} is the double layer capacitance and R_{CT} is the charge transfer resistance and Z_W is a specific electrochemical element of diffusion, also called Warburg element (Randles, 1947). For analysing the EIS data for a PEMWE cell, a graphical representation denoted Nyquist plot, illustrated in Figure 2.6.2b, is normally used (Bruce, et al., 1994). The Nyquist chart is obtained by plotting the negative imaginary impedance Z'' against the real part of the impedance Z' , as shown in Figure 2.6.2 (b) & (c). The Nyquist plot is used as a mean to best visualise and define the Randles electrical circuit elements. The semicircles observed at high frequencies corresponds to the electron transfer limited process and linear part at lower frequencies represents the diffusion limited process (Dale, 2009; Dhirde, et al., 2010).

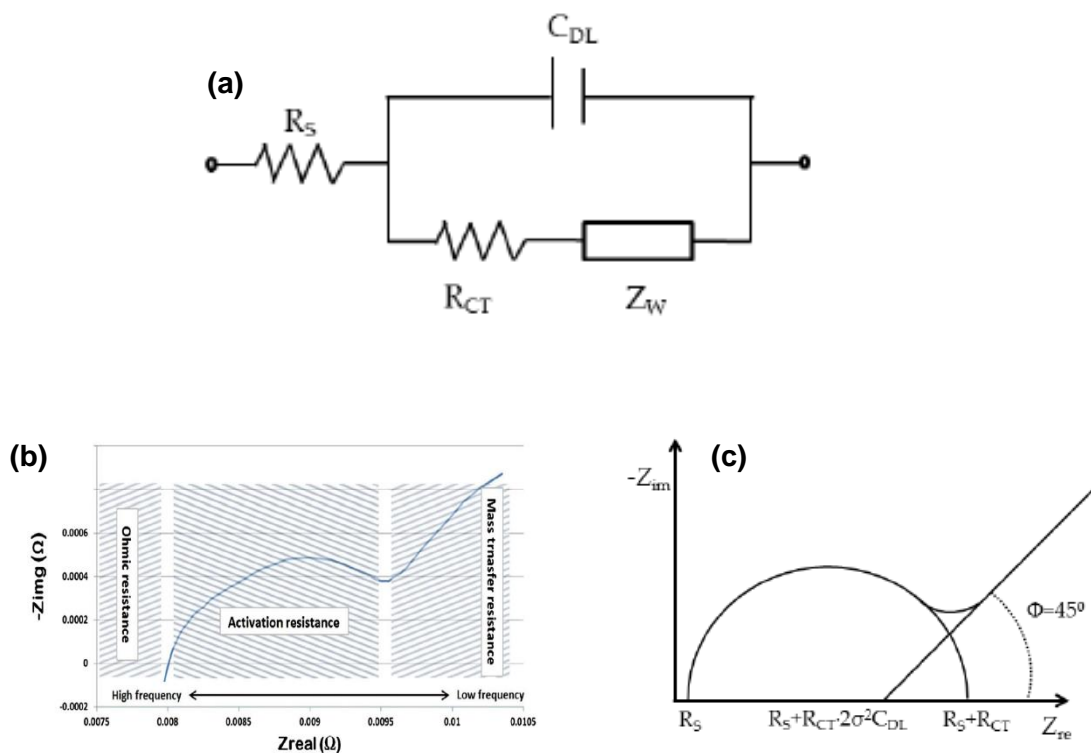


Figure 2.6.2: (a) Schematic representation of Randles circuit. (b) Typical impedance plot for a PEMWE cell with denoted resistance types for different regions. (c) Nyquist plot of Randles circuit frequency response (Bruce, et al., 1994; Merwe, et al., 2014; Randles, 1947).

2.7. Highly Porous Electrodes Catalyst Layers

The addition of pore forming substances to the catalyst inks of proton exchange membrane (PEM) systems enables the formation of electrodes catalyst layers with optimised porosity (Song, et al., 2005; Zhao, et al., 2007). This results in better accessibility of reactants to the electrocatalyst sites of the electrode catalyst layer; thus, increasing the catalyst utilisation within the catalyst layers and improving the performance of the overall PEM systems (Song, et al., 2005; Zhao, et al., 2007). Consequently, (Fischer, et al., 1998; Song, et al., 2005; Zhao, et al., 2007).

2.7.1. Pore Forming Additives Properties

For a solid substance to be chosen as a candidate for PEM system pore forming additive, some basic properties must be met to ensure that the PEM electrodes catalyst layers will not be poisoned (Fischer, et al., 1998). Physical and chemical properties such as pyrolysis

temperature, solubility, and particle size determine the use of the pore forming additive for a PEM systems electrodes optimisation (Reshetenko, et al., 2007; Song, et al., 2005).

The pyrolysis temperature indicates the pore forming additive's ability to decompose easily and fully at reasonable temperature during the extraction step of the PEM systems electrodes fabrication without requiring an additional chemical treatment (Reshetenko, et al., 2007; Song, et al., 2005). The solubility is a good indicator of the pore forming additive property to disperse uniformly and not dissolve during the catalyst ink mixing step. The particle size of the pore forming materials ensures that the introduction of additional porosity does not increase the ohmic resistance by spreading out the TPB sites (Reshetenko, et al., 2007; Song, et al., 2005; Tucker, et al., 2005).

2.7.2. Effects of Pore Forming Additives on Electrodes Structures and Overall PEM Systems Performance

Great efforts have been made in the development of the fabrication methods of optimised electrodes to improve the overall PEM systems performance and lower the total investment costs (Babic, et al., 2017). Fischer et al., (1998) disclosed a method for the preparation of PEMFC electrodes using the GDE method with lithium carbonate and ammonium carbonate as pore forming substances. It was found that additional coarse porosity from PEMFC electrodes catalyst layers was obtained by adding pore forming substances to the electrocatalyst inks which allowed for better access of oxygen inside the cathode layer and resulting to the enhancement of PEMFC system performance (Fischer, et al., 1998). Gamburgzev and Appleby (2002) demonstrated an improvement in PEMFC system performance by adding a pore forming composition of acetylene black/PTFE to their electrodes using GDE method. They found that at 0.7 V the current density of the PEMFC system improved from 0.2 A cm⁻² to 0.6A cm⁻² at 50°C; also, the electrodes porosity increased from 25 % to 50 % and the mass transport limitations decreased significantly (Gamburgzev & Appleby, 2002).

Furthermore, Song et al., (2005) reported that the addition of ammonium carbonate to the cathode electrode of a high-temperature PEMFC system enhanced the cathode catalyst activity, minimised the mass transport limitations within the cathode catalyst layer, and increased the overall cell voltage by 19% (Song, et al., 2005). In their study, Tucker et al., (2005) were able to improve the performance of the direct methanol fuel cell (DMFC) system, obtained an anode electrode with a higher porosity than the one without pore forming additives, and showed a 50 percent increase in power density by introducing lithium carbonate to the DMFC anode catalyst ink formulation. Also, Reshetenko et al., (2007) found that the

addition of ammonium carbonate and ammonium bicarbonate as pore forming substances to the cathode structure of an air-breathing DMFC yielded large amount of coarse pore, increased the current density as results from an increase in catalyst utilisation, increased the power density of the system at up to 75 mW cm⁻², and reduced the mass transport limitations. A sample of research findings from the addition of pore forming additives to electrodes catalyst inks formulations of PEM systems and their effects on the electrodes catalyst layers structures and overall systems performance studies is presented in Table 2.7.1.

Table 2.7.1: Summary of research studies on the effects of pore forming substances on the structure and properties of catalyst layers and performance.

Pore forming Additives	PEM Systems	Effects	Study
Lithium Carbonate and Ammonium Carbonate	PEMFC	<ul style="list-style-type: none"> - Additional electrode coarse porosity. - Performance enhancement. 	(Fischer, et al., 1998)
Acetylene black / PTFE	PEMFC	<ul style="list-style-type: none"> - System current density improvement. - Increase electrode porosity. - Decrease catalyst layer mass transport limitations. 	(Gamburzev & Appleby, 2002)
Ammonium Carbonate	PEMFC	<ul style="list-style-type: none"> - Enhanced the catalyst activity. - Minimized the mass transport limitations within the electrode catalyst layer. - Increase in cell voltage. 	(Song, et al., 2005)
Lithium Carbonate	DMFC	<ul style="list-style-type: none"> - System performance improvement. - Higher electrode porosity. - Enhanced system power density. 	(Tucker, et al., 2005)
Ammonium Carbonate and Ammonium Hydrogen carbonate	DMFC	<ul style="list-style-type: none"> - Creation of large amount of coarse pore in the electrode. - Increase of the system current density. - Increase in electrode catalyst utilisation. - Reduction of mass transport limitations within the electrode catalyst layer. 	(Reshетенko, et al., 2007)
Monodispersed Polystyrene Particles	PEMFC	<ul style="list-style-type: none"> - Improved system performance at high current densities. - Enhanced the mass transport properties of the catalyst layer. 	(Zlotorowicz, et al., 2015)

CHAPTER 3 DEVELOPMENT OF THE FABRICATION METHOD FOR PEMWE ELECTRODES

In this chapter, the experimental method developed in this study for the fabrication of the PEMWE electrodes is presented. This includes details on the PEMWE catalyst ink coating machine and ink formulation; the presentation of data obtained from the investigation of various anode electrode fabrication method parameters and their discussions; and the summary of the optimised PEMWE electrodes fabrication procedure. In this study, the PEMWE anode catalyst layers were prepared using the Mayer rod coating method. The Mayer rod method is a low cost, easy-to-use coating method for both laboratory and large-scale fabrication of PEMWE electrodes. The fabrication of the PEMWE electrodes was done using the catalyst coated membrane (CCM) method; where both the anode and cathode catalyst layers were applied from coated substrates through the decal transfer process, onto the surface of the proton exchange membrane.

3.1. Mayer Rod Coating

For the development of the fabrication method, a commercial Sb-doped SnO₂ (ATO) powder was used as a replacement for the PEMWE anode catalyst material. ATO is significantly affordable and more abundant compared to PEMWE electrocatalyst materials, making it an ideal alternative for these preliminary investigations. Furthermore, next generation PEMWE anode catalysts may comprise of ATO and similar doped oxides as catalyst supports (Rajan, et al., 2020). Therefore, by using this material, know-how and procedures for next generation PEMWE electrodes catalyst layers fabrication comprising ATO supported catalysts could be established in-house.

The anode electrode fabrication procedure used in this study was based on the published work by Maximilian & Gasteiger (2016) and expanded to the scope of this study through in-depth laboratory investigations and optimisation of fabrication method parameters such as ink components ratios, ink mixing and coating conditions with respect to the Mayer rod coating technique.

3.1.1. Mayer Rod Coater Parameters

The Mayer rod coater is the simplest ink coating machine that can be used to obtain reproducible, accurate, and uniform surface layer coatings onto varied number of substrates (Cherrington & Liang, 2016).

For this study, a readily available doctor blade spreader (COATMASTER 510 XL, ERICHSEN GmbH & Co. KG) was modified to accommodate wire-wound rods for a Mayer rod application to apply the ATO layers onto a substrate. Table 3.1.1 below shows the selection chart of different wire rods available in the lab and their corresponding diameters and expected coated layers thicknesses. The modified doctor blade machine was automated with standard coating speeds varied from 2.5 mm s⁻¹ to 80.0 mm s⁻¹.

Table 3.1.1: Wire-wound size selection chart for the Mayer Rod Coater (*R.D. Specialities, 2016*).

Wire-wound		Wet Film Thickness		Dry Coat Weight, g m ⁻² (% Solids) ^a		
No	Diameter, mm	Mm	µm	25%	50%	100%
10	0.25	1.00	25.40	6.35	12.70	25.40
12	0.30	1.20	30.48	7.62	15.24	30.48
13	0.33	1.30	33.02	8.26	16.51	33.02
15	0.38	1.50	38.10	9.53	19.05	38.10
24	0.61	2.40	60.96	15.24	30.48	60.96
25	0.64	2.50	63.50	15.88	31.75	63.50
30	0.76	3.00	76.20	19.05	38.10	76.20
70	1.78	7.00	177.80	44.45	88.90	177.80

^a. The dry coat weight calculations assume a coating density of 1.0 g cm⁻³ and the percentage solids is by volume.

To fabricate anode electrodes with catalyst loadings of > 1 mg_{cat} cm⁻², considering the limited availability of the commercial PEMWE anode catalyst, and accounting for at least 70 percent of solids loss during the Mayer rod coating, the rod size of 0.61 mm diameter (or rod No. 24) was selected. To determine the optimum Mayer rod coater speed, the ATO ink of 25 wt.% total solid particles was made with 6 g ATO. 0.8 g dry ionomer or 11.6 wt.% of the total solid particles mass was added, based on the formulation published by Maximilian & Gasteiger, (2016). The water to 2-propanol (IPA) solvent mixture mass ratios of 1:3 was selected as well as the ink mixing parameters of 12 hours and 100 rpm ball milling. The ATO ink then coated onto Teflon substrates with varied Mayer rod speeds. It was observed that coating speed has also an influence on the ATO coated layer quality and particles loading. Table 3.1.2 shows

different investigated Mayer rod coating speed conditions and their effects on the ATO layer quality and loading.

Table 3.1.2: Various Mayer rod coater speed values and their corresponding experimental ATO coated layer quality and loading.

Speed, mm/s	Solid Particles Retention	ATO Loading, mg _{ATO} cm ⁻²
2.5	2%	0.04 ± 0.01
5.0	4%	0.07 ± 0.012
10.0	12%	0.18 ± 0.01
20.0	16%	0.25 ± 0.002
40.0	21%	0.32 ± 0.004
50.0	31%	0.47 ± 0.01
60.0	35%	0.54 ± 0.012
70.0	47%	0.72 ± 0.02
80.0	35%	0.52 ± 0.011

For the fabrication of PEMWE electrodes using the Mayer rod coating, the challenges are to produce substrates with films that are evenly coated, have the highest ink retention and reproducible loadings. To operate in the best Mayer rod coating conditions, the Mayer rod coating speed of 70 mm s⁻¹ was selected for the subsequential development of the fabrication method for PEMWE electrodes.

3.1.2. Ink Formulation Parameters

The optical microscope was selected to determine the optimum ATO ink formulation parameters in relation to the Mayer rod coating technique to accelerate this study. This is because it is a simple and quick method to conduct observation of the fabricated ATO layer samples integrity.

3.1.2.1. Effects of Solvent Mixture Components Ratio

Recent studies showed that the rheology, stability and coatability of the catalyst ink depends greatly on the type and boiling point of the solvent utilised in the catalyst ink formulation (Therdthianwong, et al., 2010; Zhao & Liu, 2019; Park, et al., 2007). Therdthianwong et al., (2010) demonstrated that usage of solvents with low dielectric constant such as ethanol, isopropanol, and water, in the catalyst ink formulation produces electrodes with higher performances compared to when high dielectric constant solvents are utilised. They also indicated that inks using isopropyl alcohol (IPA) as solvent produced smooth layer surface and great attachment to the proton exchange membrane. Therefore, in this study isopropyl alcohol was selected as the solvent for all the subsequent ink formulations.

To investigate the effects of solvent mixture ratio, water to 2-propanol (IPA) solvent mixture mass ratios of 1:3, 1:1 and 3:1 was selected. The ATO ink comprised 25 wt.% solid particles (Sb-doped tin oxide and dry ionomer). With the dry ionomer weight percentage of 11.6 wt.% of the total solid particles mass (Maximilian & Gasteiger, 2016). The ATO ink was mixed for 12 hrs at 100 rpm, then dried at a temperature of 75°C and coated onto a Teflon sheet substrate. The loading was kept at $0.7 \pm 0.02 \text{ mg}_{\text{ATO}} \text{ cm}^{-2}$ for all samples. Figure 3.1.1 shows optical microscope images of ATO ink coated onto Teflon substrates obtained from varying water to IPA solvent mixture mass ratios in the ATO ink formulation. The coated substrates from the ATO ink formulation of 1:3 water-IPA mixture mass ratio produced ATO layers with big triangular shaped ATO coarse separated by large uncoated areas, as shown in Figure 3.1.1a, which flaked off when handled in the lab. This was the result of the total delamination of the ATO catalyst layer from the Teflon substrate.

After increasing the water-IPA mixture mass ratio from 1:3 to 1:1, the coated substrates generated ATO layers with small spherical shaped ATO coarse separated by small uncoated areas in some sections and smaller-to-none uncoated areas in other sections, as observed in Figure 3.1.1b. Also, when handled in the lab, it was noticed that the delamination of the ATO catalyst layers from the Teflon substrates decreased significantly. When the mass of water in the solvent mixture was increased by three-fold to obtain a water-IPA mixture mass ratio of 3:1, the coated substrates produced ATO layers with similar ATO coarse properties as those from the water-IPA mixture mass ratio of 1:1 and the same degree of ATO layers delamination. However, the uncoated substrate areas separating the ATO coarse were evenly distributed throughout the entire surface layer compared to ATO layers produced from the water-IPA mixture mass ratio of 1:1, as shown in Figure 3.1.1c.

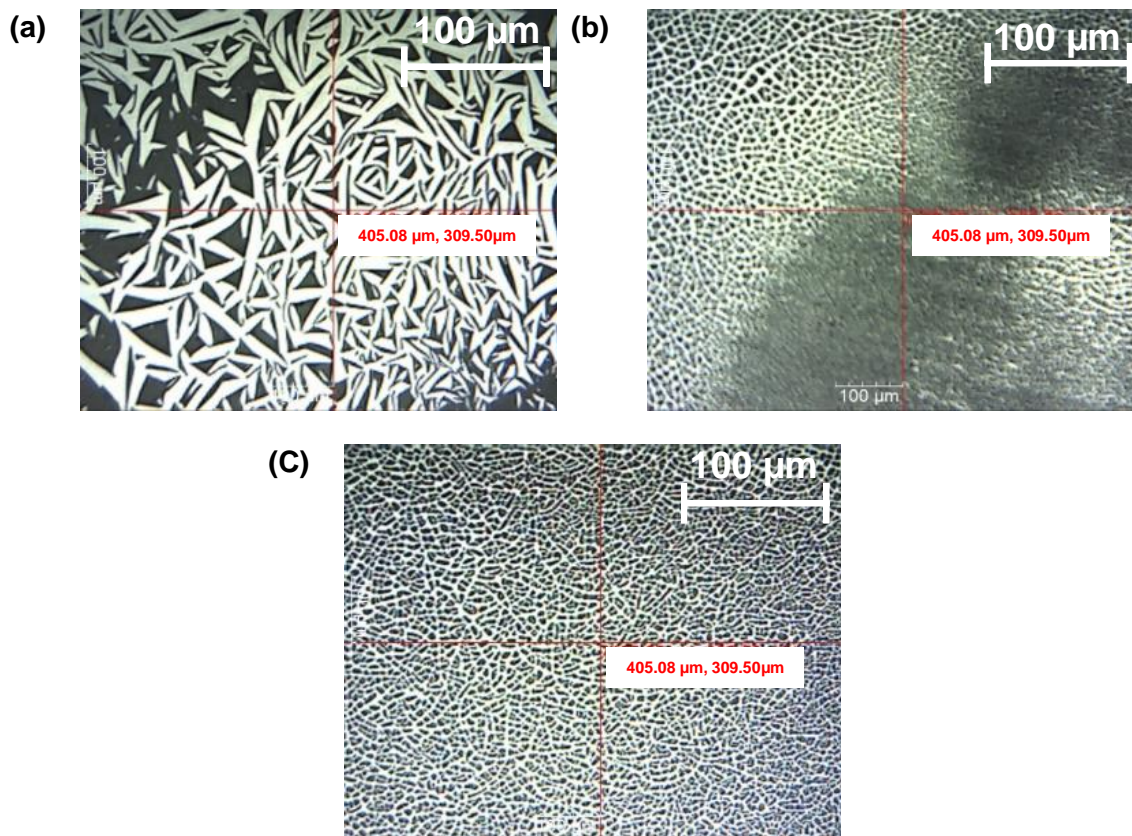


Figure 3.1.1: Optical microscope images of ATO coated substrates showing differences in the coated film surface obtained from ATO ink formulations solvent mixture of: (a) Water : IPA ratio of 1:3, (b) Water : IPA ratio of 1:1, and (c) Water : IPA ratio of 3:1.

The findings from this investigation show that the homogeneity the ATO surface layer, the degree of contact between the catalyst layer and its substrate were greatly influenced by the amount of the organic substance (in this case, isopropyl alcohol) present in the solvent mixture of ink formulation. This can be explained as the water quantity in the solvent mixture solution increased so is the total solvent solution boiling point which consequently reduced the rate of evaporation of the solvent mixture. This allowed for a better retention of the organic colloidal substance in the ink solution during the ink mixing step; therefore, improving the formation of the proton conduction network and consequently the intimate contact between the catalyst of the proton conduction network and consequently resulting to an intimate contact between the catalyst layer and its substrate.

Furthermore, a slower organic solvent evaporation rate during the drying step thus resulting in more uniform ATO surface layer. This agrees with the findings published by Therdthianwong et al., (2010) which stipulates that the smoothness of the catalyst layer greatly depends on the boiling point of the solvent mixture.

As the surface layer delamination and inhomogeneity can be undesirable, the water to IPA solvent mixture mass ratio of 3:1 was selected for all the ensuing ATO ink formulation.

3.1.2.2. Effect of the Solid Content

In this study, the total solids content was varied as follows 25 wt.%, 30 wt.%, 35 wt.% and 40 wt.% with the corresponding maximum attainable catalyst loading of $0.7 \pm 0.02 \text{ mg}_{\text{ATO}} \text{ cm}^{-2}$, $1.3 \pm 0.05 \text{ mg}_{\text{ATO}} \text{ cm}^{-2}$, $2.2 \pm 0.13 \text{ mg}_{\text{ATO}} \text{ cm}^{-2}$, and $3.0 \pm 0.25 \text{ mg}_{\text{ATO}} \text{ cm}^{-2}$; respectively. The dry ionomer weight percentage was 11.6 wt.% of the total solid particles mass (Maximilian & Gasteiger, 2016). To complete the ATO ink formulation, water to IPA ratio of 3:1 was selected while keeping the mixing parameters the same (12 hrs and 100 rpm) as well the drying temperature (75°C). The loading was kept at $0.7 \text{ mg}_{\text{ATO}} \text{ cm}^{-2}$ for all varied solid content samples for an accurate surface layer comparison. The total solid content was determined by dividing the sum of the mass of dry ATO particles and dry ionomer in the ink over the total weight of ATO ink. Figure 3.1.2 shows the optic microscope images of the surface layers from various solid content ATO inks coated onto Teflon substrates.

The samples with 25 wt.% solid content produced delaminated ATO layer and inhomogeneous surface layer as shown in Figure 3.1.2a. This is similar to what was observed and discussed in the effect of solvent mixture components ratio section. The solid content of 30 wt.% in the ink formulation produced coated substrates with surface layers without the presence of uncoated ATO areas as shown in Figure 3.1.2b resulting in homogeneous surface layers. The solid content of 35 wt.% provided coated substrates with the presence of small cracks from the surface layer as seen in Figure 3.1.2c. Lastly, the solid content of 40 wt.% produced coated substrates with irregularly distributed ATO, forming concentrated ATO spots shown with the darker coloured areas in Figure 3.1.2c. Furthermore, the concentrated ATO areas showed the presence of cracks. These resulting in uneven ATO surface layers.

The irregularities in the ATO surface layer observed from coated substrates of 25 wt.%, 35 wt.% and 40 wt.% solid contents can be partially attributed to the ink rheology and the coating instrument specifications and limitations. The Mayer rod coater requires a coating fluid of viscosity ranging between 1000 to 4000 mPa s to produce evenly coated surfaces (Hoth, et al., 2013). Liquids with lower viscosity values produce coated surfaces with uncoated areas as observed in Figure 3.1.2a; and liquids with higher viscosities produce coated surfaces with concentrated areas as shown in Figure 3.1.2 c & d.

This is due to the shear force applied by the rod onto the coated fluid and the resistance from the fluid to flow which is dependent of its viscosity. The viscosity of the catalyst ink fluid is influenced by the solid content in the catalyst ink formulation.

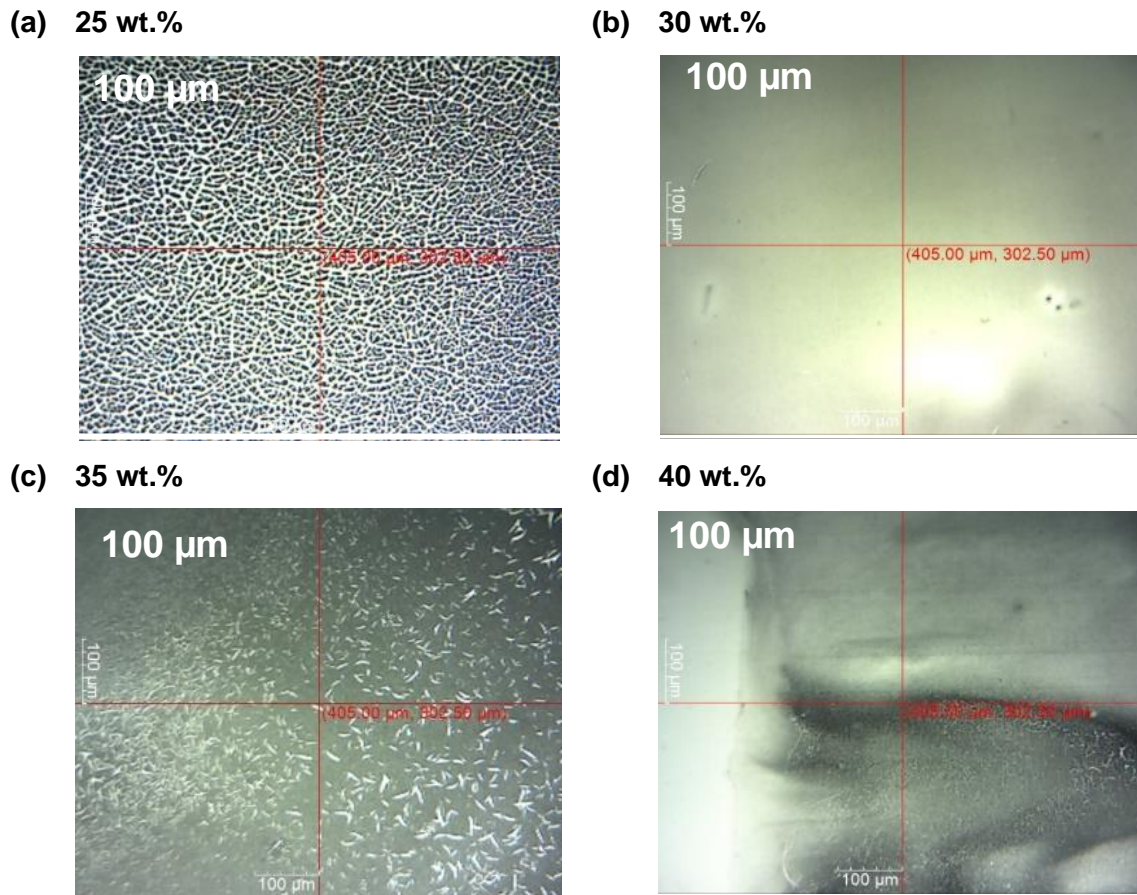


Figure 3.1.2: Optical microscope images of AT0 coated substrates surface showing the difference in AT0 layers obtained from the ink solid content of (a) 25 wt.%, (b) 30 wt.%, (c) 35 wt.% and (d) 40 wt.%.

With no access to conduct viscosity measurements of the various AT0 ink prepared in-house, it is assumed that the ink formulation with the solid content of 30 wt.% produced a fluid viscosity that fell within the Mayer rod coated requirement, thus resulting in a uniform coated surface. In contrast, the AT0 ink with 25 wt.% solid content produced lower viscosity fluid, and AT0 inks with 35 wt.% and 40 wt.% solid contents produced higher viscous fluids with respect to the Mayer rod fluid viscosity desired range. This also agrees with findings from Therdthianwong et al., (2010) work which showed that the viscosity of the catalyst ink can affect the catalyst layer surface quality.

The catalyst ink with very low viscosity flows freely on the substrate resulting in poor surface coverage whereas the catalyst ink with very high viscosity causes a poor catalyst ink distribution on the coating substrate (Therdthianwong, et al., 2010). As the surface layer cracks and uniformity can be undesirable, the solid content of 30 wt.% was selected in all subsequent ink formulations.

3.1.3. Ink Mixing Parameters

The ball mill method was selected for the mixing of the ink due to its abilities to decrease the solid particle size, increase particle surface area and disperse the nanoparticle catalyst and Nafion ionomer (Burmeister & Kwade, 2013). To obtain reproducible ink formulations which are independent of solid particle types, it was important to understand the effects of mixing conditions on the liquid catalyst processing. In this study, ink mixing times of 12, 18 and 24 hours were investigated and compared by observing their corresponding coated surface layer images generated using the scanning electron microscopy. This investigation was conducted using the water to IPA ratio of 3:1; the solid content of 30 wt.% (Sb-doped tin oxide and dry ionomer) with the dry ionomer weight percentage of 11.6 wt.% of the total solid particles mass (Maximilian & Gasteiger, 2016); mixed at 100 rpm; dried at 75°C and coated onto a Teflon substrate. The loading was kept at $1.1 \pm 0.018 \text{ mg}_{\text{ATO}} \text{ cm}^{-2}$ for all samples. **Error! Reference source not found.** shows SEM images of catalyst layer surface from varying commercial Sb-doped tin oxide powder ink mixing times.

It can be observed that the 12 hours mixing time of the ATO ink solution resulted in the formation of large ATO agglomerates with the presence of big ATO lump-like-shapes on the surface of the relatively smooth ATO layer as shown in Figure 3.1.3a. The increase of the mixing time to 18 hours lowered the number and size of the ATO agglomerates (refer to Figure 3.1.3b). Furthermore, using a 24-hour mixing time provided a much-refined ATO nanoparticle agglomerates sizes which were uniformly distributed across the ATO surface layer as shown in Figure 3.1.3b. The main aim of the ink mixing process is to break up catalyst particle aggregates and reduce catalyst agglomerates to a desired nanoparticle size (Paipetis & Kostopoulos, 2013). In this investigation, by submitting the ATO ink formulation to longer mixing times, more ATO aggregates were efficiently broken up whilst enough energy was produced to overcome bonding forces between solid nanoparticles resulting in an effective de-agglomeration of the ATO nanoparticles. Hence, the ATO coated layers from the 24-hour mixing time presented fewer ATO aggregates, and smaller ATO nanoparticle agglomerates (Figure 3.1.3c) compared to 18 (Figure 3.1.3b) and 12 hours (Figure 3.1.3a), respectively.

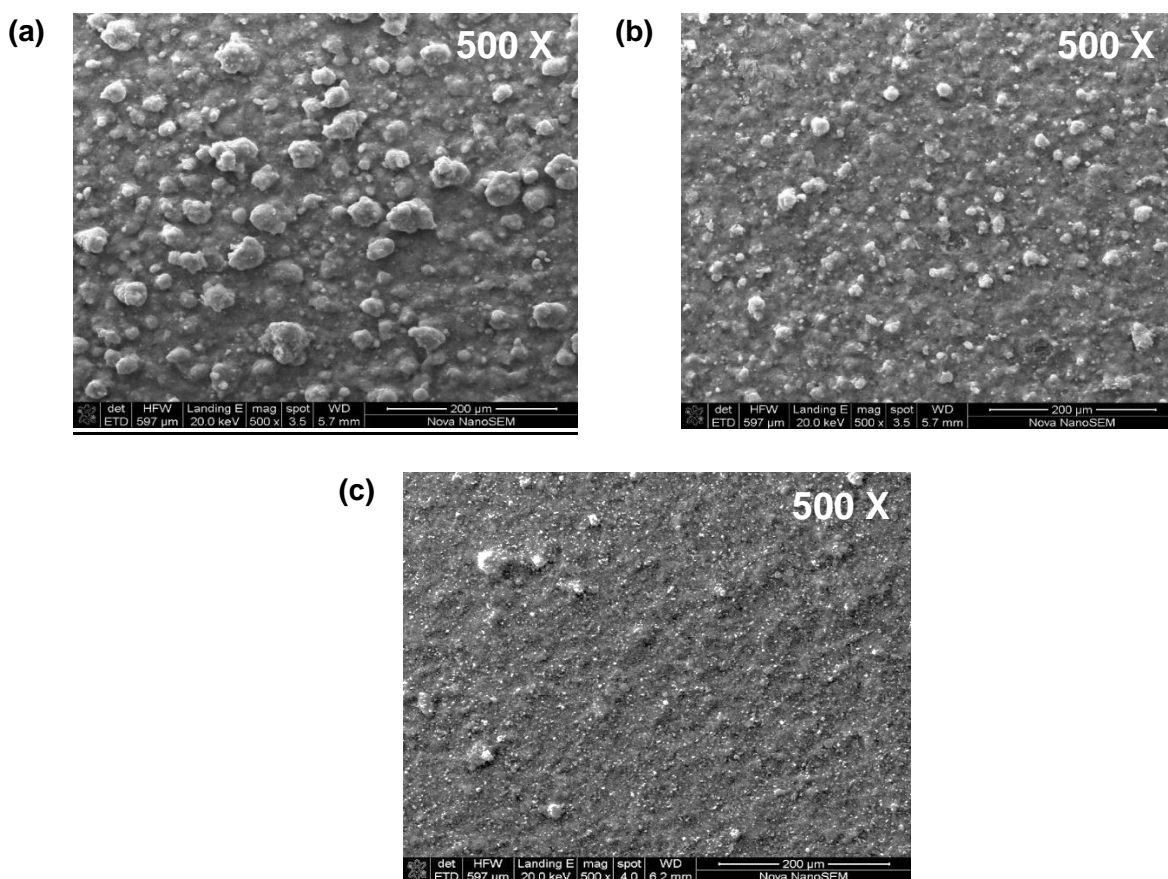


Figure 3.1.3: SEM images of ATO surface layer form the ink mixing time of: (a) 12 hours, (b) 18 hours, and (c) 24 hours.

3.2. Decal Transfer Process

The full transfer of the catalyst layer from the coated substrate onto the proton exchange membrane, while maintaining the integrity of the catalyst layer triple phase boundary, requires the understanding of the decal process parameters and their effects on the catalyst layer structure. The use of high pressures during the hot-pressing process can result in structural deformation of the catalyst layer while low pressures can result in the incomplete transfer of the catalyst layer and thereby cause a loss of catalyst material (Liang, et al., 2015). In this study, hot pressing parameters were varied to determine the lowest hot-pressing pressure possible for a full integral catalyst layer transfer. An ATO coated substrate was prepared using the optimal parameters obtained from the Mayer rod coating method development study.

The ATO ink comprised of 3:1 water to IPA mass ratio, 30 wt.% solids (with 11.6 wt. % dry ionomer). The slurry was mixed at 100 rpm for 24 hours and coated onto a Teflon substrate

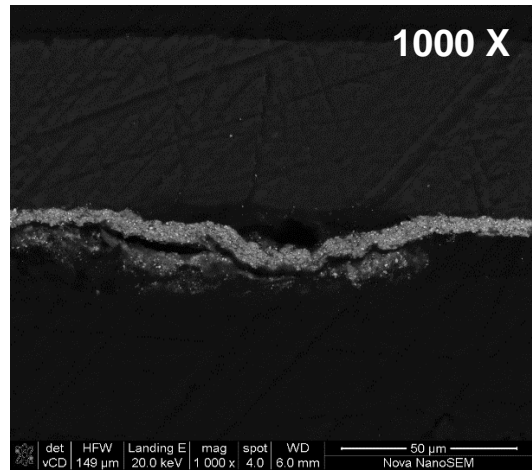
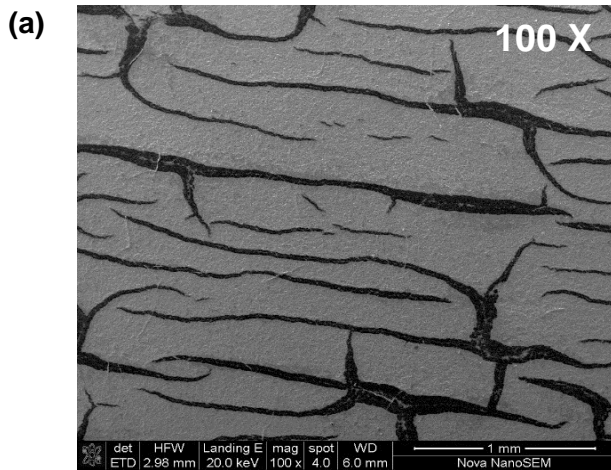
and dried at 75°C in a conventional oven. Table 3.2.1 shows the summary of the investigated hot-pressing parameters and their effects on the anode and cathode ATO layers transfer.

From these findings (refer to Table 3.2.1), it can be observed that the full transfer of anode and cathode ATO layers from their coated substrates onto the proton exchange membrane was achieved with hot-pressing pressure of as low as 500 Kg cm⁻² and time of 3 minutes with an average reproducibility of 97%. However, observations from Figure 3.2.1, which illustrates the SEM images of the ATO coated films prepared with different hot-pressing pressures, show that considerable distortions and compressions of the ATO layer structure from higher hot-pressing pressures of 11000 Kg cm⁻², 5000 Kg cm⁻², 2000 Kg cm⁻² and 1000 Kg cm⁻² occurred. This is due to higher tensions imposed on the ATO layers by the hot-pressing plates during the decal transfer operation which was also reported by Prasanna et al., (2004) and Xiong and Manthiram, (2005).

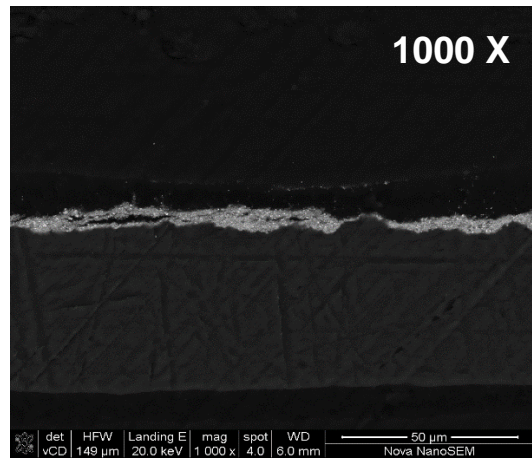
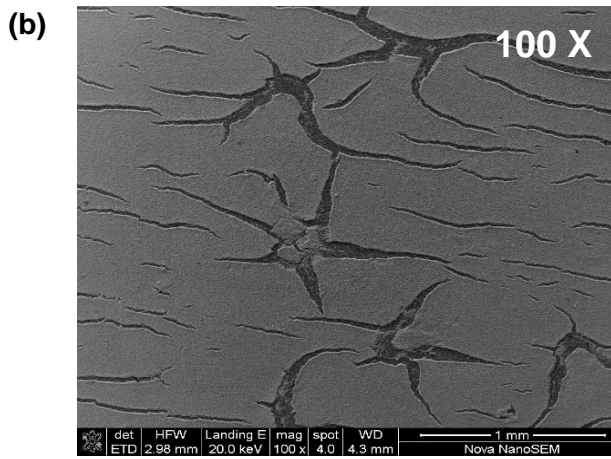
Table 3.2.1: Summary of hot-pressing parameters and their effects on the ATO layer transfer.

Hot-pressing Parameters			ATO Loading ($\text{mg}_{\text{ATO}} \text{cm}^{-2}$)				Layer Transferred		Process Reproducibility
Temperature	Pressure	Time	Initial		Final		%		%
$^{\circ}\text{C}$	Kg/cm^2	min	Anode	Cathode	Anode	Cathode	Anode	Cathode	
155	11000	6	1.3 ± 0.02	1 ± 0.07	1.3 ± 0.05	1 ± 0.01	100	100	100
155	5000	6	1.3 ± 0.02	1 ± 0.07	1.3 ± 0.06	1 ± 0.05	100	100	100
155	2000	6	1.3 ± 0.02	1 ± 0.07	1.3 ± 0.03	1 ± 0.03	100	100	100
155	1000	6	1.3 ± 0.02	1 ± 0.07	1.3 ± 0.01	1 ± 0.01	100	100	96
155	500	6	1.3 ± 0.02	1 ± 0.07	1.3 ± 0.04	1 ± 0.09	100	100	94
155	500	3	1.3 ± 0.02	1 ± 0.07	1.3 ± 0.01	1 ± 0.06	100	100	96
155	400	6	1.3 ± 0.02	1 ± 0.07	1.21 ± 0.07	0.85 ± 0.01	93.1	85	95
155	400	3	1.3 ± 0.02	1 ± 0.07	1.15 ± 0.05	0.8 ± 0.02	88.5	80	95

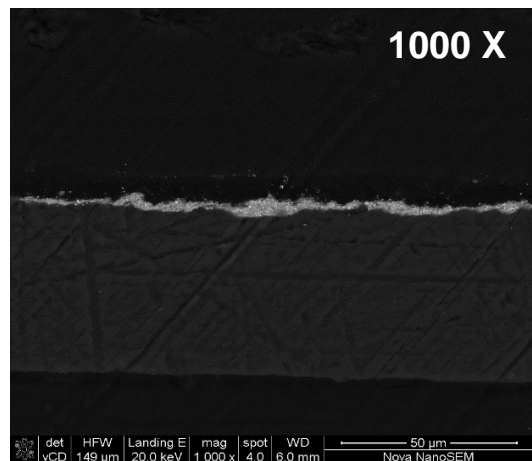
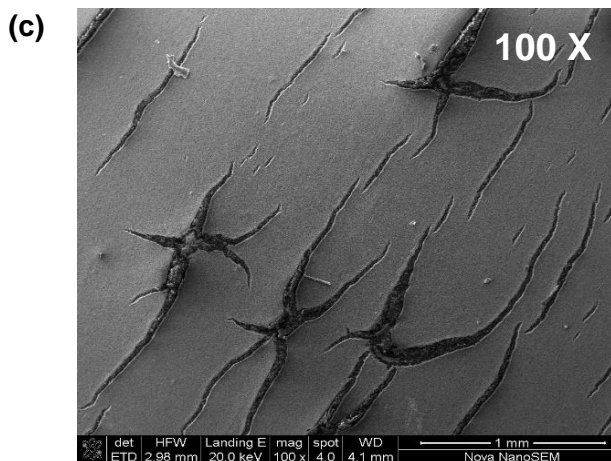
11000 Kg/cm²



5000 Kg/cm²

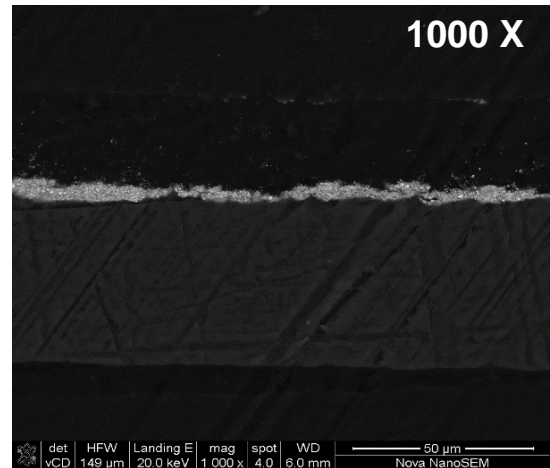
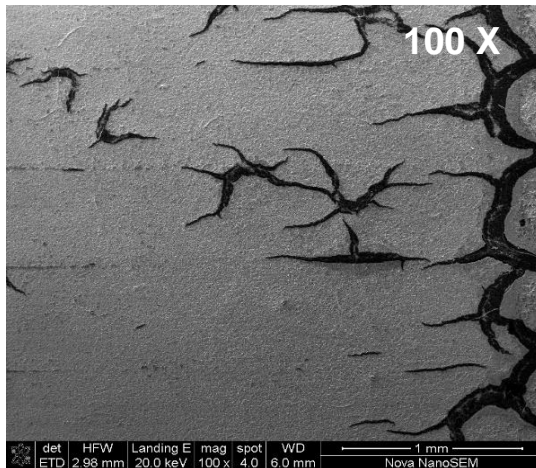


2000 Kg/cm²



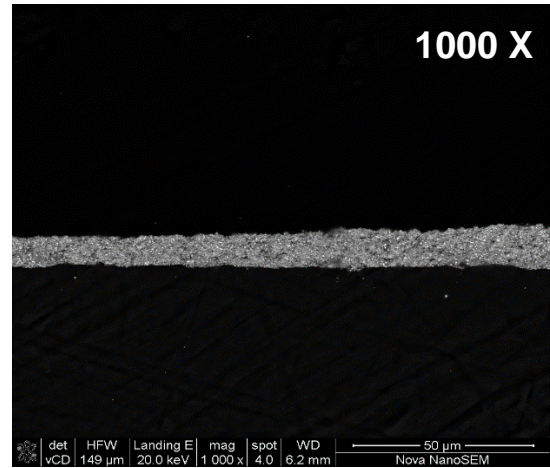
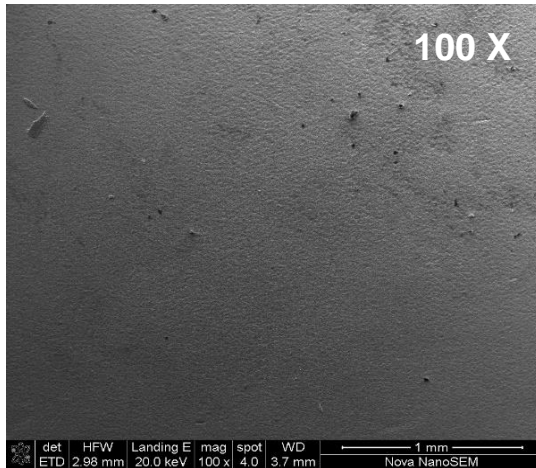
1000 Kg/cm²

(d)



500 Kg/cm²

(e)



400 Kg/cm²

(f)

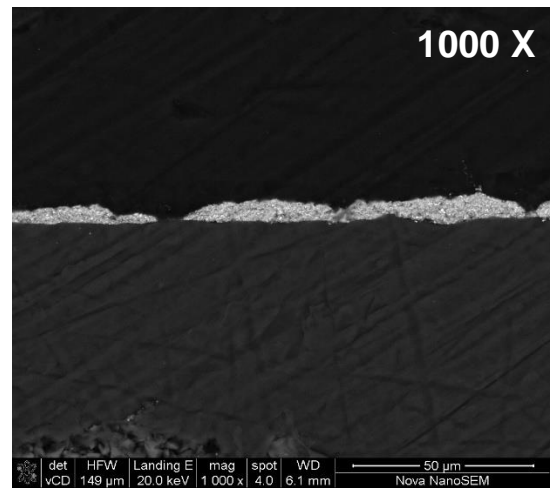
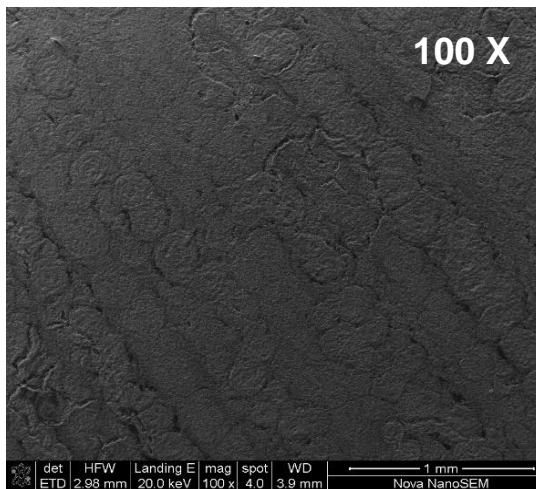


Figure 3.2.1: SEM images of ATO anode coated substrate layer surfaces and cross-sections form various decal transfer pressures, hot pressed for 6 minutes.

3.3. Fabrication of PEMWE Electrodes Using Mayer Rod Coating

This section details the materials and chemicals, as well as the sequential procedure used for the fabrication of the PEMWE electrodes using commercial electrocatalysts. The fabrication of the PEMWE electrodes was done using the catalyst coated membrane (CCM) method where both the prepared anode catalyst layers and purchased cathode catalyst layers were applied from their respective coated substrates, through the decal transfer process, onto the surface of the proton exchange membrane.

3.3.1. Chemicals and Materials Specifications

The summary of all the materials used for the preparation of the PEMWE electrodes is presented in Table 3.3.1. For the anode electrode catalyst layer, a commercial $\text{IrO}_x\text{-TiO}_2$ was selected as the OER electrocatalyst (refer to Table 3.3.1). The cathode catalyst layer was purchased from HyPlat Ltd, South Africa and comprised 60 wt.% Pt on high surface area carbon (HSAC) support with an ionomer content of 12 wt.% (long side chain 1100EW). The cathode electrode catalyst layer was coated on a 300 mm thick fibre glass reinforced Teflon with an active area of 200 cm².

Table 3.3.1: Chemicals and Materials for PEMWE electrodes fabrication.

Component	Grade	Function	Supplier
Iridium(IV) Oxide on Oxidic Support	75 wt.% IrO _x	Anode Electrocatalyst	Umicore
Nafion© Perfluorinated Resin Solution, D2021	20 wt.% Nafion Content 34 wt.% Water 44 wt.% 1-propanol	Anode Ionomer	Ion Power
Propan-2-ol	99.99% extra pure	Catalyst Ink Solvent	Sigma-Aldrich
Platinum on High Surface Area Carbon Support	60 wt.%	Cathode Electrocatalyst	Mintek
Ionomer Long Side Chain 1100EW	12 wt.%	Cathode Ionomer	-
De-ionised Water	18 MΩ cm	Catalyst Ink Solvent	In-house
Zirconia Beads	-	Mixing	-
Ceramic Jar	-	Mixing	-
Roller Mill	-	Mixing	-
Fiberglass Reinforced Teflon	-	Catalyst Ink Coating Substrate	EASYTAPE PTY LTD
Mayer Rod Coater	-	Anode Catalyst Ink Coating Machine	ERICHSEN GmbH & Co. KG

3.3.2. Catalyst Coated Membrane Method

In this study, the fabrication of the anode and cathode electrodes was done using the catalyst coated membrane (CCM) method where both the anode and cathode catalyst layers were applied indirectly, through the decal transfer process, onto the surface of the proton exchange membrane. Figure 3.3.1 shows the summary of the entire fabrication procedure of PEMWE electrodes with the anode catalyst ink with and without pore forming additive developed in this study.

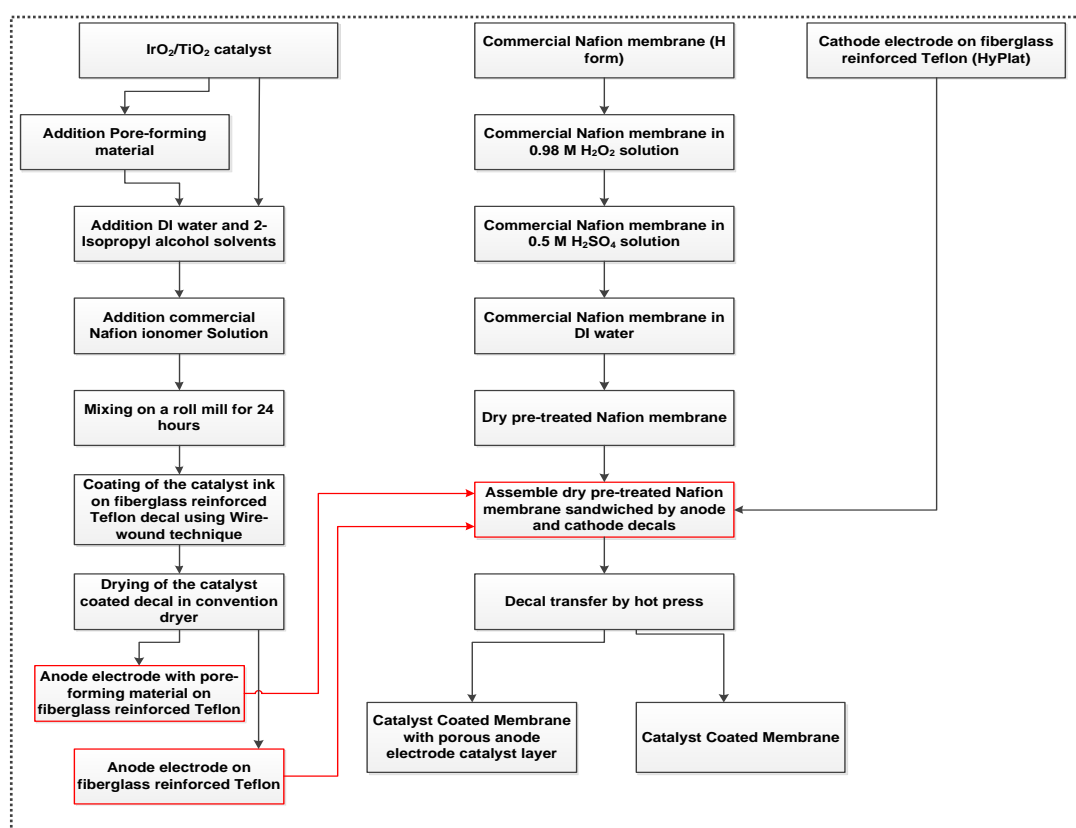


Figure 3.3.1: Schematic representation of the experimental procedures of the PEMWE electrodes fabrication developed in this study.

3.3.2.1. Anode Catalyst Ink Formulation Procedure

A lab coat, nitrile gloves and a mask were worn when working with the iridium catalyst. An amount of IrO_x on oxidic support catalyst (75 wt.% iridium; Elyst Ir75 0480 from Umicore, Germany) was added into a 15 mL ceramic jar, the weight of the catalyst was determined by weighing the jar before and after the addition of the dry catalyst powder.

Then, de-ionised (DI) water (18 M Ω cm) was added to the catalyst powder, followed by the addition of propan-2-ol solvent (purity \geq 99.9%, from Sigma Aldrich) and Nafion[®] ionomer solution (20 wt.% ionomer in water and 1-propanol; D2021 from Ion Power, USA). After investigation of the effects of the water to isopropanol mass ratio in the solvent mixture and catalyst solid content, the following component weight ratios of 1/1.8/0.4/0.64, was selected for the IrO_x-TiO₂ catalyst powder, water, isopropanol, and ionomer solution, respectively. Finally, 26.4g of 2 mm diameter ZrO₂ balls were added to the other components and the jar was then closed. The purchased chemicals and materials, used for the PEMWE anode catalyst ink preparation, are shown in Figure 3.3.2.

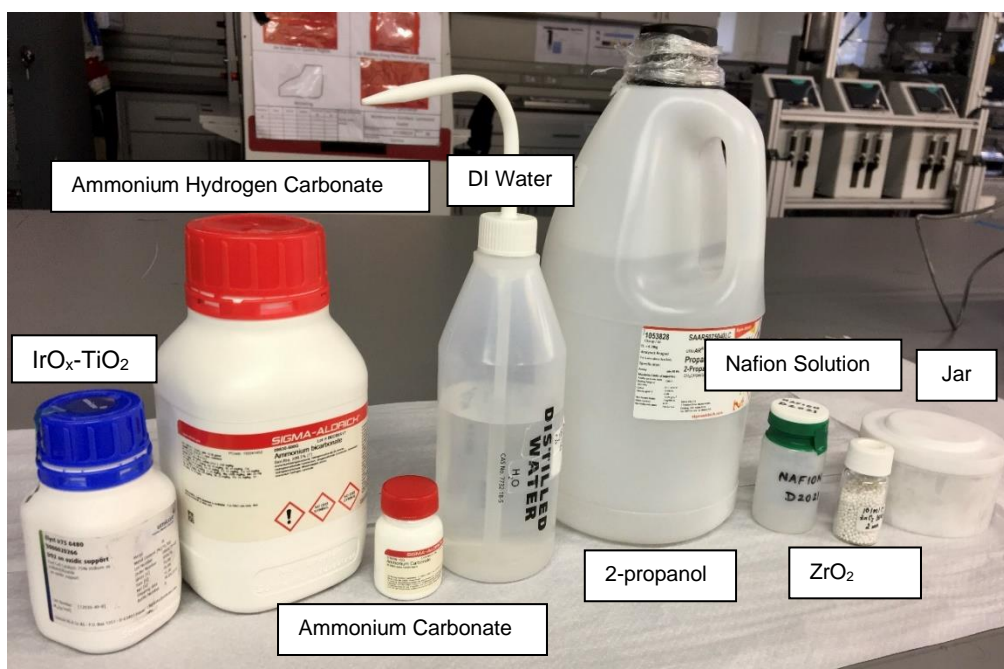


Figure 3.3.2: Image of chemicals and materials used in the anode electrode catalyst ink preparation.

3.3.2.2. Anode Catalyst Ink Mixing Procedure

The ceramic jar containing the TiO₂ supported IrO_x catalyst ink mixture was placed on a roller mill, as shown in Figure 3.3.3, and sealed. Then the rotation speed of the ball miller was adjusted to a rate of 100 rpm so that the balls would travel up the side of the jar before tumbling. Based on the findings obtained from investigation of the influence of the ink mixing time, 24 hours of catalyst ink mixing time was selected to achieve a homogeneous catalyst ink suspension.



Figure 3.3.3: Roller mill machine used for anode electrode catalyst ink fabrication.

3.3.2.3. Anode Catalyst Ink Coating Procedure

After the mixing step, the homogeneous IrO_x on oxidic support catalyst ink was transferred into a 100 mL glass beaker and mixed continuously with a micro-stir bar throughout the coating step. To do so, a 1000 mm x 2000 mm 300 μm thick fiberglass reinforced Teflon substrate (TF005SQM; from EASYTAPE PTY LTD, South Africa) was weighed and cleaned with isopropanol on both sides and then fixed on a clean glass plate with a position holder. All dust and air bubbles were removed beneath the substrate, and it was ensured that the surface of the substrate was perfectly flat with no wrinkles. The desired rod was placed on the Mayer rod coating machine, touching the substrate surface. The catalyst ink was then deposited right in front of the Mayer rod, as shown in Figure 3.3.4a, using a disposable plastic pipette. A coating speed of 70 mm s^{-1} was set on the machine the start button was pushed to distribute the ink homogeneously on the Teflon substrate as illustrated in Figure 3.3.4b. The film thickness of the coating and the resulting catalyst loading was controlled by varying the volume of the catalyst ink deposited.

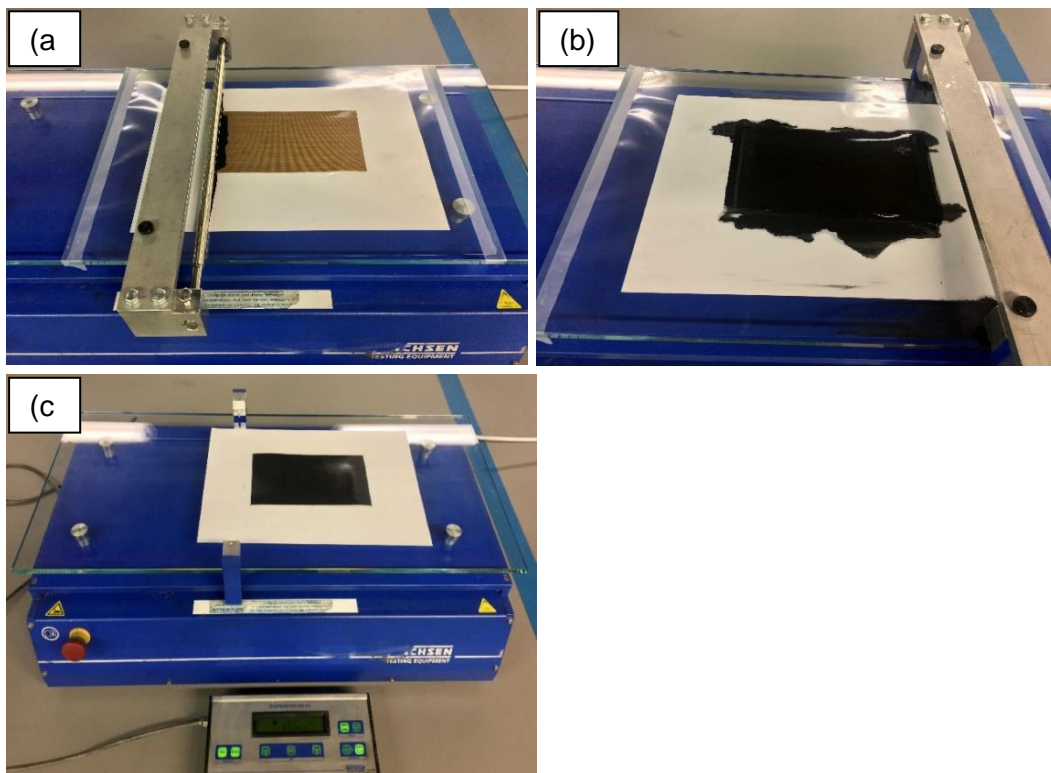


Figure 3.3.4: (a) Anode catalyst ink deposited onto the Teflon substrate. (b) Teflon substrate after the coating of the anode electrode catalyst ink. (c) Slightly

The glass plate with the coated substrate, as shown in Figure 3.3.4c, was removed from the Mayer rod machine and left in atmospheric conditions for few minutes then dried at 75°C in a conventional oven until all the solvent was evaporated. To remove ink residue, the wire-wound rod was cleaned right after usage while the ink was still wet. After drying, the coated substrate (refer to Figure 3.3.5) was weighed using a microbalance then preserved in a plastic container for the next fabrication step.

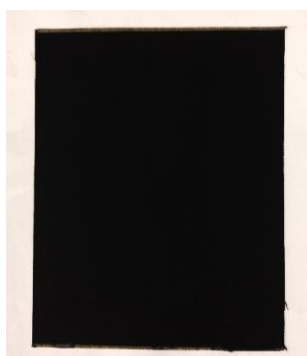


Figure 3.3.5: Images of IrO_x-TiO₂ anode electrode catalyst layer coated on Teflon sheet.

3.3.2.4. PEMWE Electrodes Fabrication Procedure

The PEMWE electrodes were fabricated by applying the solid anodic and cathodic catalyst layers onto the proton conductive membrane using the decal transfer method. Proton conductive membranes (50.8 μm thick Nafion[®] 212 and 135 μm thick Nafion 115, from Ion Power Inc, New Castle, DE) were cut into 5 cm x 5 cm squares and pre-treated following conventional method to remove impurities and activate the membrane before the decal transfer process. The Nafion membrane was cleaned in 0.98 mol/L hydrogen peroxide solution for 1 hour, then transferred into 0.5 mol/L sulfuric acid solution for two hours, and finally washed in de-ionised water for another 2 hours. The Nafion membrane was dried overnight in air in a covered petri dish at room temperature before use. All treatment steps were conducted at 80°C. After that, the anode and cathode decals were cut into 2.5 cm x 2.5 cm active areas. One side of the dry pre-treated proton exchange membrane was labelled to easily differentiate the cathode to the anode electrode after the decal transfer process. The Nafion membrane was then placed onto the anode decal followed by putting the cathode decal on top of the membrane with the catalyst coated sides facing each other. It was important to ensure that the Nafion membrane was flat without wrinkles and that anode and cathode decals were perfectly aligned. The coated substrates-membrane assembly was enveloped between two sheets of fiberglass-reinforced Teflon, to reduce sticking, followed by sandwiching between five “office copy” papers and then compressed using a preheated hot hydraulic press at 155 °C and 500 Kg cm⁻² for 3 minutes. Figure 3.3.6 shows the overview decal transfer process that was used to prepare all the catalyst coated membranes samples in this study.

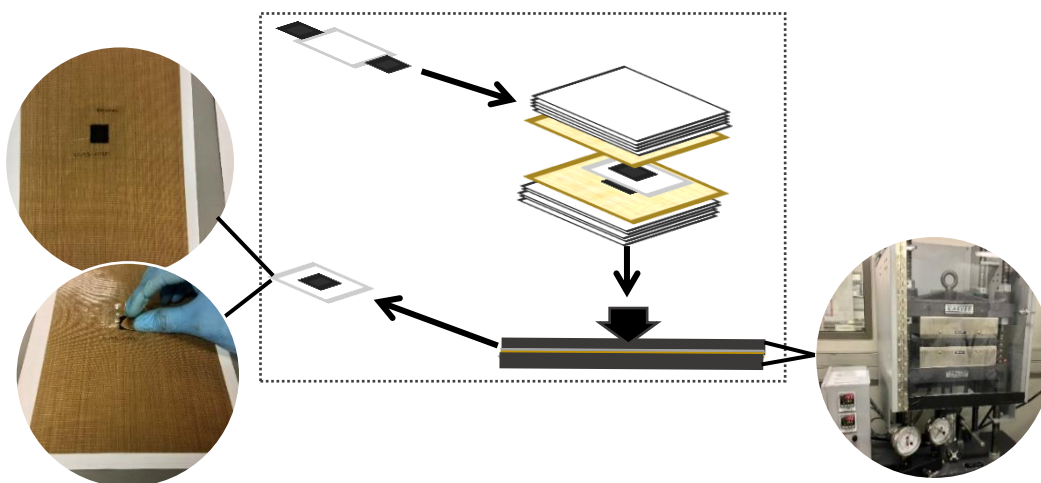


Figure 3.3.6: Overview of the decal transfer process for the fabrication of the PEM water electrolyser electrodes using the CCM method (not drawn to scale).

The decal transfer temperature of 155 °C was selected because it was well above the pyrolysis temperature of ammonium carbonate and ammonium hydrogen carbonate pore formers molecules, which should allow them to easily and fully be removed from the anode electrode catalyst layer. The decal transfer pressure and hot-pressing time were selected after the investigation of their influence on the ATO layers. After cooling the hot-pressed coated substrate-membrane assembly to room temperature, the substrates were peeled off from the membrane and thin 5 cm² casting layers of anode and cathode catalyst layers were left on each side of the proton exchange membrane forming the catalyst coated membrane as shown in Figure 3.3.7. The catalyst coated membrane was then covered with PTFE sheets to avoid contamination and stored in a plastic bag.

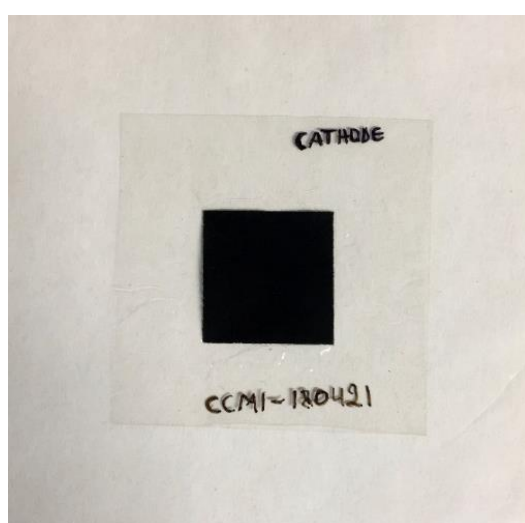


Figure 3.3.7: Image of IrO_x-TiO₂ anode catalyst layer and Pt/C cathode catalyst layer on a proton exchange membrane after decal transfer process forming a catalyst coated membrane (CCM).

The samples catalyst loadings were determined by weighing the Teflon substrates before and after the decal transfer using a microbalance. For the cathode electrodes, the loading was $0.95 \pm 0.15 \text{ mg}_{\text{Pt}} \text{ cm}^{-2}$. For the anode electrodes, the catalyst loadings were $1.01 \pm 0.1 \text{ mg}_{\text{Ir}} \text{ cm}^{-2}$ for Nafion 212 membrane and $1.31 \pm 0.11 \text{ mg}_{\text{Ir}} \text{ cm}^{-2}$, $0.59 \pm 0.03 \text{ mg}_{\text{Ir}} \text{ cm}^{-2}$ for Nafion 115 membrane. With the anode electrode ionomer content of 11.6 wt.% total solid mass for all CCM samples.

3.4. Fabrication of Highly Porous Anode Catalyst Layers Using Mayer Rod Coating

3.4.1. Catalyst Coated Membrane Method

The fabrication of the PEMWE electrodes with highly porous anode catalyst layers was done following the same procedure and conditions used to fabricate the PEMWE electrodes without pore formers. The only exception, in this instant, was the addition of pore forming materials (ammonium carbonate or ammonium hydrogen carbonate) after adding iridium(IV) oxide catalyst powder during the anode catalyst ink formulation step. The ratio of pore forming material to $\text{IrO}_x\text{-TiO}_2$ catalyst in the total dry anode electrode was varied between 1:10 and 1:1. The image of the anode electrode catalyst layer from the catalyst ink formulation with 1:10 ammonium bicarbonate to $\text{IrO}_x\text{-TiO}_2$ ratio is shown in Figure 3.4.1.

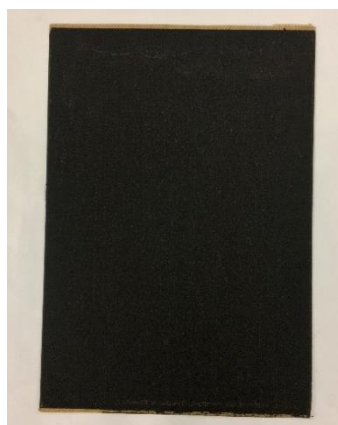


Figure 3.4.1: Images of $\text{IrO}_x\text{-TiO}_2$ anode electrode catalyst layer catalyst layer coated on a Teflon substrate with 1:10 NH_4HCO_3 pore forming additive to $\text{IrO}_x\text{-TiO}_2$ catalyst weight ratio.

Granular spots of white-ish colour can be noticed from Figure 3.4.1. These are because of the presence of ammonium bicarbonate particle aggregates in the anode electrode layer. After drying, the coated anode electrode substrate was weighed using a microbalance then preserved in a plastic sheet for the next step. The PEMWE electrodes with highly porous anode catalyst layers were fabricated using the same decal transfer conditions as the PEMWE electrodes without pore formers.

After cooling the hot-pressed coated substrate-membrane assembly at room temperature, the substrates were peeled off from the membrane and thin 5 cm² casting layers of anode and cathode catalyst layers were left on each side of the proton exchange membrane then covered with PTFE sheets to avoid contamination and stored in a plastic bag.

The catalyst loadings of the fabricated electrodes samples were determined by weighing the Teflon substrates before and after the decal transfer using a microbalance. For the cathode electrodes, the loading was $0.95 \pm 0.15 \text{ mg}_{\text{Pt}} \text{ cm}^{-2}$. For the Nafion 212 anode electrodes, the catalyst loadings were $1.016 \pm 0.012 \text{ mg}_{\text{Ir}} \text{ cm}^{-2}$ and $0.39 \pm 0.011 \text{ mg}_{\text{Ir}} \text{ cm}^{-2}$ for 1:10 and 1:1 (NH₄)₂CO₃ to IrO_x-TiO₂ catalyst weight ratios, respectively. $1.013 \pm 0.03 \text{ mg}_{\text{Ir}} \text{ cm}^{-2}$ and $0.39 \pm 0.01 \text{ mg}_{\text{Ir}} \text{ cm}^{-2}$ for 1:10 and 1:1 NH₄HCO₃ to IrO_x-TiO₂ catalyst weight ratios, respectively. For the Nafion 115 anode electrodes, the catalyst loadings were $0.95 \pm 0.1 \text{ mg}_{\text{Ir}} \text{ cm}^{-2}$ and $0.72 \pm 0.2 \text{ mg}_{\text{Ir}} \text{ cm}^{-2}$ for 1:10 wt.% NH₄HCO₃ to IrO_x-TiO₂ catalyst weight ratios; $0.5 \pm 0.011 \text{ mg}_{\text{Ir}} \text{ cm}^{-2}$, $0.4 \pm 0.01 \text{ mg}_{\text{Ir}} \text{ cm}^{-2}$ for 1:1 NH₄HCO₃ to IrO_x-TiO₂ catalyst weight ratios.

3.4.2. Removal of Pore Forming Materials

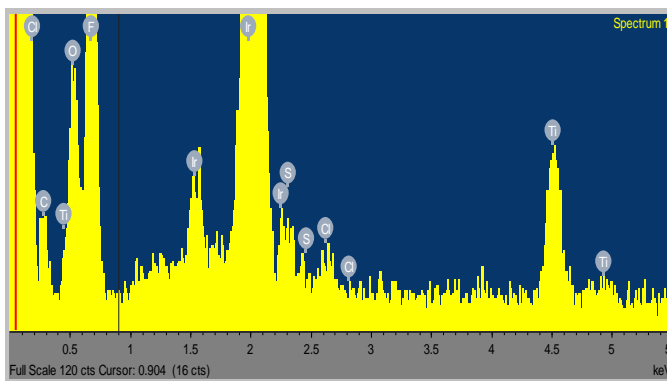
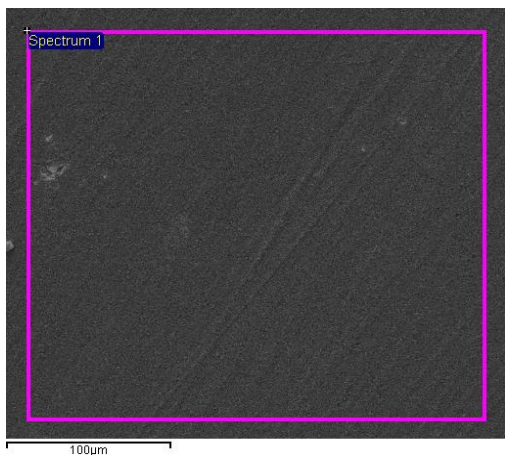
The investigation of the removal of pore forming additives through decal transfer process from PEMWE anode catalyst layer was conducted. Using Iridium(IV) oxide on oxidic support catalyst from Umicore. The catalyst ink formulation comprised a 2 g of IrO_x-TiO₂ catalyst powder, 11.6 wt.% total solid content dry ionomer and a water to IPA solvent mixture ratio of 3:1. The solid content was kept at 30 wt.% total weight anode catalyst ink solution. One set of samples was fabricated without adding pore formers and the other with each (NH₄)₂CO₃ and NH₄HCO₃. The pore former to catalyst weight ratio were kept at 1:1. For all the samples, the catalyst ink was mixed for 24 hours at 100 rpm, coated using the Mayer rod coater onto a Teflon substrate then dried in the oven at 75°C. The coated anode catalyst layers were transferred from substrates onto the proton exchange membranes on both sides at 155°C and 500 Kg/cm².

The energy-dispersive X-ray spectroscopy (EDX) was used to analyse the chemical compositions of the IrO_x-TiO₂ catalyst layers. The results of samples chemical compositions from the EDX analysis are summarised in Table 3.4.1 and their corresponding catalyst layer images are shown in Figure 3.4.2. Figure 3.4.2 shows that the similarities in chemical compositions among all anode electrode catalyst layer samples observed from the energy-dispersive X-ray analysis indicates that the complete decomposition and removal of pore forming substances under the decal transfer conditions of 155°C, 500 Kg/cm² and 3 minutes of hot-pressing was achieved.

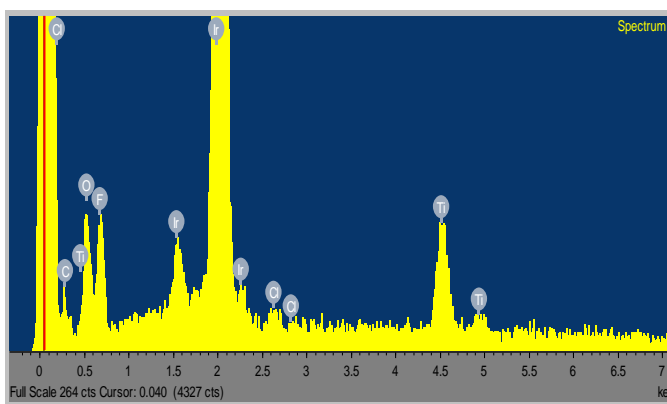
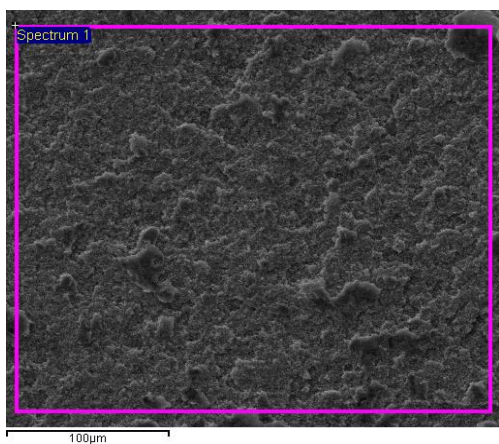
Table 3.4.1: Summary of chemical composition from EDX of the IrO_x-TiO₂ electrode samples after decal transfer process.

Element	CCM without Pore Former			CCM with Ammonium Carbonate 1:1 (NH ₄) ₂ CO ₃ to IrO _x -TiO ₂ catalyst weight ratio			CCM with Ammonium Bicarbonate 0.469 wt.% NH ₄ HCO ₃ to IrO _x -TiO ₂ catalyst weight ratio		
	App. Concentration	Weight%	Atomic%	App. Concentration	Weight%	Atomic%	App. Concentration	Weight%	Atomic%
C	0	0	0	0	0	0	0	0	0
O	19.37	19.43	46.83	17.57	17.88	35.02	0	0	0
F	6.84	18.12	36.79	11.94	32.54	53.69	6.77	51.79	87.24
S	-	-	-	0.72	0.89	0.87	-	-	-
Cl	0.58	0.71	0.78	0.42	0.58	0.51	0.22	1.09	1.09
Ti	6.16	5.31	4.28	4.16	4.19	2.74	4.07	3.72	2.75
Ir	66.52	56.43	11.32	42.95	43.92	7.16	42.63	43.39	8.92
Totals		100			100			100	

(a) CCM without Pore Former



(b) CCM with 1:1 Ammonium Carbonate to IrO_x-TiO₂ catalyst weight ratio



(c) CCM with 1:1 Ammonium Bicarbonate to IrO_x-TiO₂ catalyst weight ratio

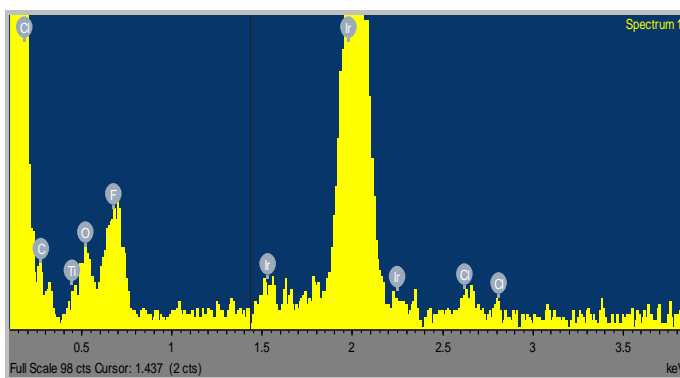


Figure 3.4.2: Anode catalyst layer surface images and their corresponding chemical compositions obtained from EDX analysis of (a) sample without pore former, (b) sample with Ammonium Carbonate and (c) sample with Ammonium Bicarbonate.

3.5. Chapter Summary

The development of a scalable fabrication process for PEMWE electrodes at HySA Catalysis CoC is critical for the achievement of the centre's national goal. In this chapter, the fabrication method for the PEMWE electrodes using Mayer rod coating machine was developed. Various fabrication method parameters influencing the physical characteristics of the electrode layer were investigated using ATO powder in replacement to $\text{IrO}_x\text{-TiO}_2$ electrocatalyst. For the ink formulation investigation, the solvent mixture components mass ratio and the solid content were found to significantly influence the physical quality of the ATO coated substrate layers. With water to IPA solvent mixture ratio of 1:3 and 1:1 resulted in the delamination of the ATO layer from the substrate after coating and a highly inhomogeneity surface coated ATO layers. However, the water to IPA solvent mixture ratio of 3:1 showed considerable improvement of the ATO coated surface layer homogeneity and binding capability to the substrate.

The ink viscosity was investigated by varying the ink solid content from 25 wt.% to 40 wt.% total ink weight, with a gradual increment of 5 wt.%. It was found that only 30 wt.% solid content ink formulation produced ATO layer with uniform surface, while 25 wt.%, 35 wt.% and 40 wt.% produced ATO layers of inhomogeneous surfaces. For the ink mixing investigation, the mixing times of 12, 18 and 24 hours were investigated and compared using their coated surface layer images from SEM. It was found that 24 hours ATO ink mixing time provided a better ATO aggregates sizes and uniform distribution of ATO particle agglomerates.

To maintain the triple-phase boundary of the catalyst layer during the decal transfer process, it was important to understand the effects of various decal transfer parameters on the catalyst layer structure. Hence, the hot-pressing pressure of 11000 Kg/cm^2 , 5000 Kg/cm^2 , 2000 Kg/cm^2 , 1000 Kg/cm^2 , 500 Kg/cm^2 and 400 Kg/cm^2 and time of 6 minutes and 3 minutes were investigated using the ATO coated films fabricated. It was found that the full transfer of the catalyst layer from the substrate to the proton exchange membrane was achieved with hot-pressing pressure of as low as 500 Kg/cm^2 and the time of 3 minutes with an average reproducibility of 97%, as shown in Table 3.2.1. Furthermore, the extent SEM analysis of the hot-pressed catalyst layers structures showed that higher hot-pressing pressures considerably distorted and compressed the catalyst layers structures compared to lower hot-pressing pressures of 500 Kg/cm^2 and 400 Kg/cm^2 as shown in Figure 3.2.1.

Using the optimum parameters obtained from the development of the fabrication method for the PEMWE electrodes study with ATO, PEMWE electrodes samples with Pt/C for the cathode catalyst layer and $\text{IrO}_x\text{-TiO}_2$ for the anode catalyst layer without pore forming additives and with ammonium carbonate and ammonium bicarbonate were prepared.

Furthermore, an investigation into the pore forming materials removal via decal transfer process was conducted using the energy-dispersive X-ray spectroscopy. From the EDX results of the anode catalyst layers without pore forming additives and with highly porous anode electrodes catalysts layers indicated that the complete decomposition and removal of pore forming particles under the decal transfer conditions of 155°C, low pressure of 500 Kg/cm², and 3 minutes of hot-pressing was achieved.

CHAPTER 4 DEVELOPMENT OF THE ELECTROCHEMICAL EVALUATION PROTOCOLS FOR PEMWE SYSTEM

In this chapter, experimental procedures developed for the electrochemical characterisation of the CCM samples are presented. This includes the identification and establishment of the minimum testing equipment requirements, investigation of operating conditions, development of data measuring conditions and procedures, and commercial CCMs benchmarking. The development of the electrochemical evaluation study was conducted using commercial PEMWE CCMs of 25 cm², Nafion 115 membrane, catalyst loadings of 3 mg_{IrRuOx} cm⁻² and 3 mg_{Pt} cm⁻² for the anode and cathode electrode, respectively. All the graphical data presented and discussed in this study are average of two or more repeats evaluation tests.

4.1. Development of the Current-Voltage Performance Evaluation Protocols

In this section, the work done on the development of the electrochemical characterisation protocols for the PEMWE electrodes is presented. It includes details on the PEMWE cell and test station hardware; instructions for the cell assembly along with the current-voltage cell performance evaluation protocols; as well as the description and discussion of the findings obtained from the current-voltage testing protocols development study. These protocols were developed through literature reviews and exhaustive laboratory investigations of the effects of different operating conditions, cell conditioning and I-V measurement parameters on the PEMWE cell performance. It should be noted that preliminary cell conditioning and data measurement protocols were done using the initial CCM benchmarking method published by Bender, et al., (2019).

4.1.1. PEMWE System Hardware

4.1.1.1. PEMWE Test Bench

The electrochemical characterisation of the PEMWE electrodes was performed with an automated test station from Greenlight Innovation using Emerald automation software. The electrolyser test station (ETS) was equipped with a fully automated power supply, inert gas and pressurised control on both anode and cathode electrodes. The ETS software enabled automatic control of the anode water supply flow rate and temperature. The overall Greenlight electrolyser test station system with a connected electrolyser cell is illustrated in Figure 4.1.1. Some of the PEMWE bench test specifications are presented in the Table 4.1.1 below.

Table 4.1.1: Greenlight innovation electrolyser test station equipment specifications.

Specifications^a	
Power Range	50W – 1MW
Water Flows	Anode and cathode DI water supply with metering pumps
Pressure Control	Up to 50 bars
System Cooling	Anode and Cathode DI water cooling with recirculation
Power Supply	Constant current, constant voltage, up to 1000 A and 3 V
Data Acquisition System	Cell voltage and temperature

^a The test station Specifications were obtained from the Greenlight Equipment Manual provided by the manufacturer.

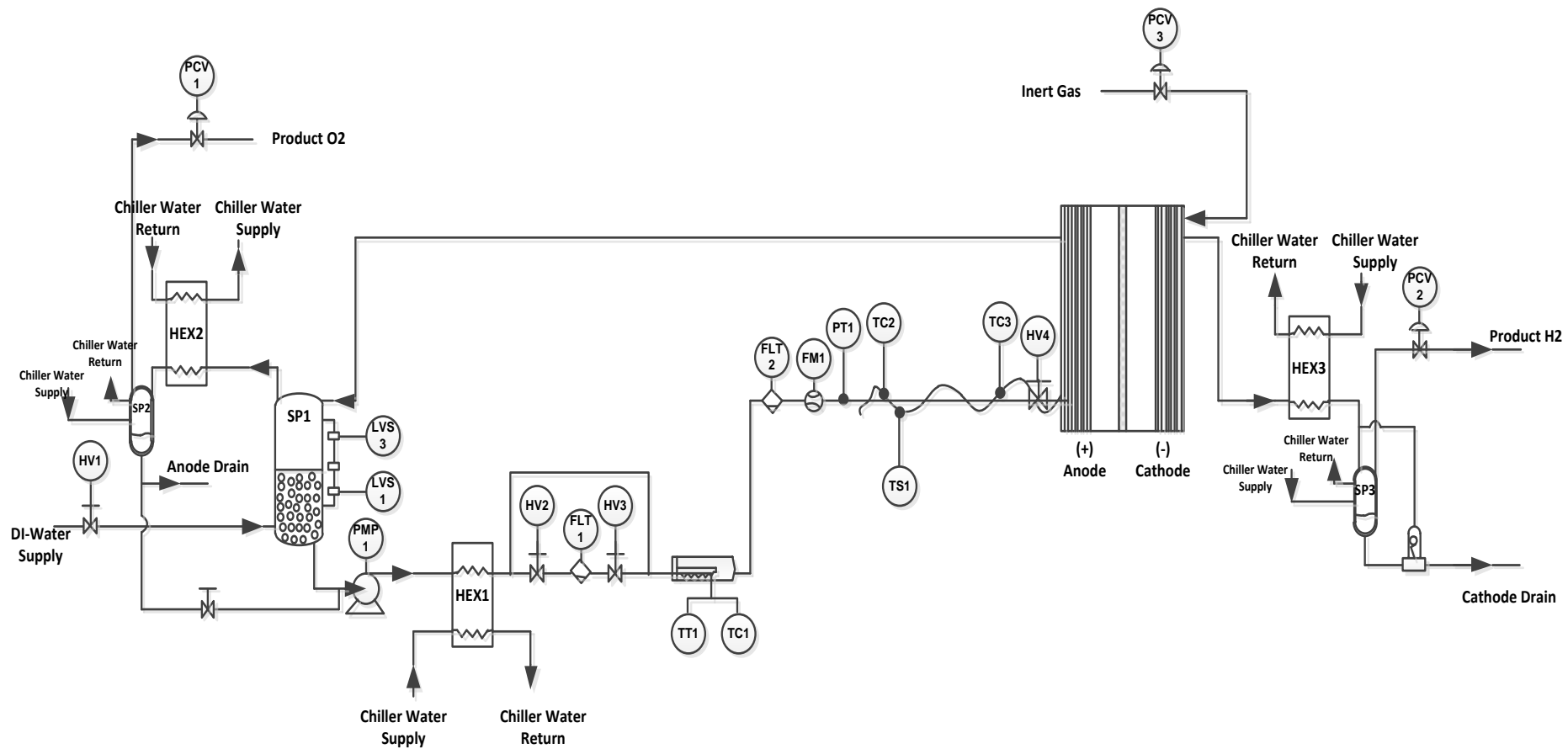


Figure 4.1.1: Process flow diagram of the PEMWE electrochemical test bench used at HySA Catalysis Centre.

4.1.1.2. PEMWE Cell

A schematic drawing of the PEMWE cell components (From Fraunhofer ISE, Germany) used in this study is shown in Figure 4.1.2. The hardware featured a typical single cell design with flat sheet gaskets for electric insulation and a more uniform pressure distribution, titanium bipolar plates with a thickness of 23.1 mm was manufactured and parallel flow-fields pins to distribute the flow inlet and outlet over the active area of the cell. The anode and cathode flow-fields were both made of titanium and consisted of evenly spaced 2 mm x 0.3 mm pins. The active area was 20 mm x 20 mm, and the hardware featured 4 mm voltage sense ports, cell voltage and temperature sensor ports, and flow inlets and outlets integrated into the flow-fields.

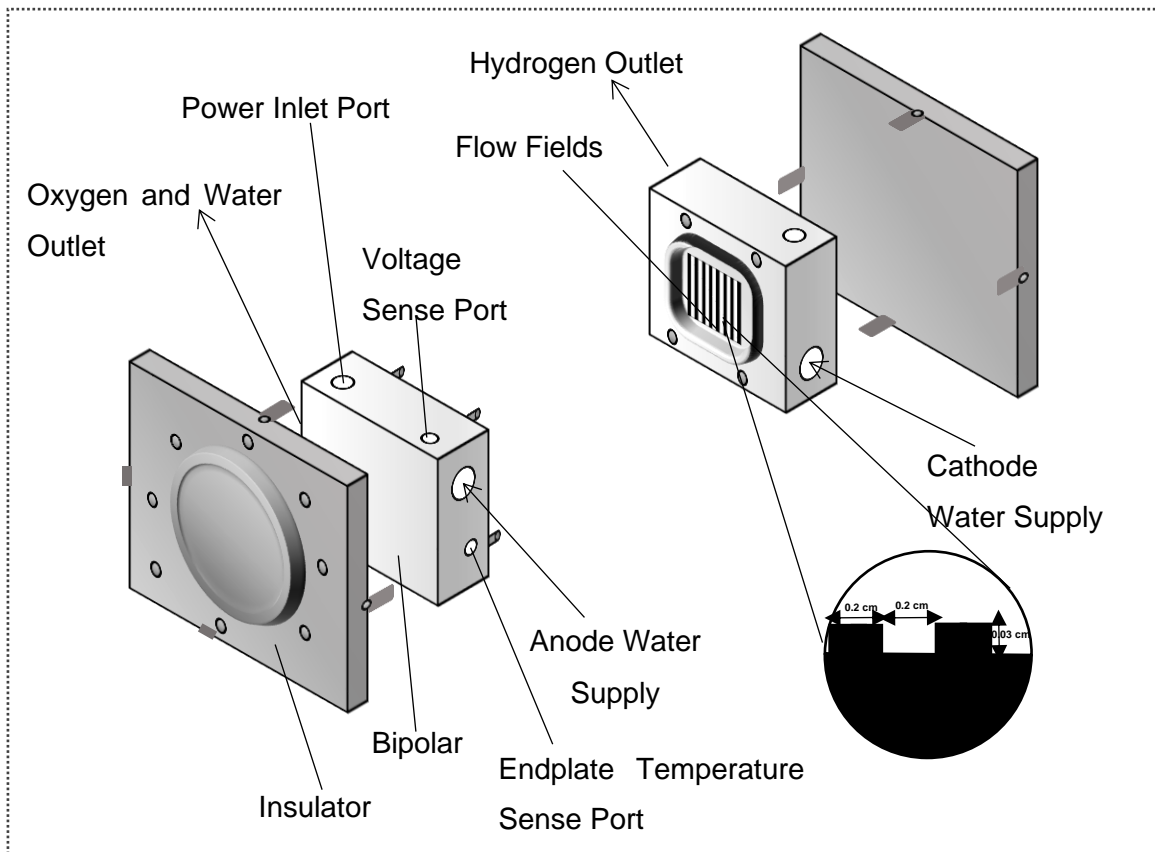


Figure 4.1.2: Schematic illustration of a PEMWE single cell (not drawn to scale).

The PEMWE cell used for this study was designed for balanced pressure conditions. The mechanical compression of the cell can be adjusted by a manual screw and the corresponding clamping force can be monitored with a force sensor. Some of the PEMWE cell important technical specifications are shown in Table 4.1.2 below.

Table 4.1.2: PEMWE cell specifications.

Technical Data	PEM electrolysis cell
Weight	± 10 Kg
Operating temp. range	20°C - 90°C
Operating pressure (max)	6 bar, balanced pressure
Active fuel cell area	3.98 cm ²
Flow-fields	Titanium
Endplate	Titanium grade 2

4.1.2. PEMWE Cell Assembly Protocols

4.1.2.1. PEMWE CCM Preparation

Before conducting the current-voltage evaluation, the commercial PEMWE CCM was gasketed to provide correct compression and prevent potential water leaks. One layer of PET sub-gasketing materials with a nominal thickness of 43 µm, judiciously cut into window-frame squares (6 cm x 6 cm outer square and 2 cm x 2 cm inner square), was used on each side of the anode and cathode, laminated to themselves and the periphery of the CCM to form a flat sealing surface. An additional thin bead of adhesive sealing material (6 cm x 6 cm outer square and 2 cm x 2 cm inner square) was placed on both side of the flat sealing surface to form a gas-and-liquid-tight seal between the PTL and the sub-gasket material. The gasketed CCM was prepared by washing it in ≤ 300 mL of 0.1 M H₂SO₄ solution for at least 1 hour to clean the catalyst layer film from any impurities. Then the clean CCM was rinsed and put in de-ionised water for 2h to remove all the sulphate radicals from the catalyst layer surface and hydrate the membrane. The PTLs were cut into 4 cm² surface area pieces with rounded corners. The metallic PTLs, when used, were sonicated in deionised water for 10 minutes. PTLs of 1 mm thickness was preferred for a maximum and optimum contact between different MEA components. Before the PEMWE components connection, the surfaces of the flow fields, bipolar plates and PEEK-frames were cleaned using fuzz-free tissues with ethanol and deionized water.

4.1.2.2. PEMWE Cell Connection

After the preparation of the PEMWE CCMs, the sonicated anode and cathode PTLs were placed in their respective half-cells (see Figure 4.1.3a). The catalyst coated membrane while still swollen was placed on top of the anode half-cell through the alignment pins. The CCM was ensured to lie flat on the PTL and not buckle as shown in Figure 4.1.3b. The anode half-cell was then turned and placed on top of the cathode half-cell while ensuring the alignment pins were aligned to the respective holes of the cathode compartment as illustrated in Figure 4.1.3c. A schematic illustration of the overall PEMWE cell with the membrane electrode assembly (PTLs and gasketed CCM) is illustrated in Figure 4.1.4.

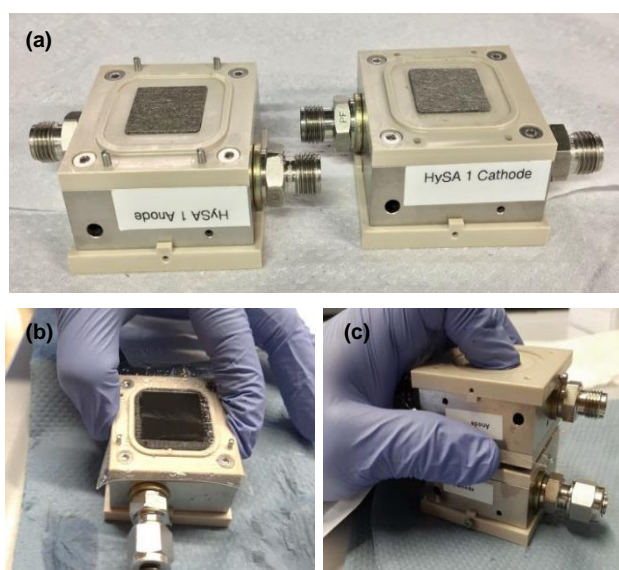


Figure 4.1.3: PEM water electrolyser cell assembly with titanium (Pt) PTLs.

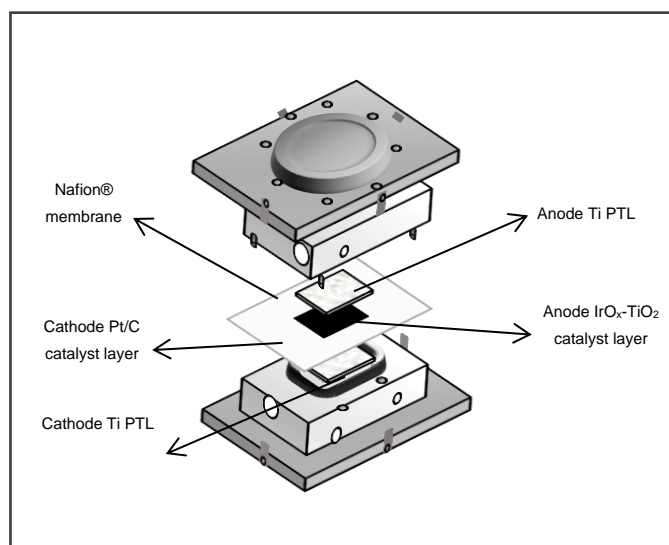


Figure 4.1.4: Schematic illustration of the PEM water electrolyser cell assembly components (not drawn to scale).

Once the two halves of the PEMWE cell were connected, the cell was quickly put into the cell compression frame with the notch for the force sensor on the anode half-cell facing upward as shown in Figure 4.1.5 . Then the force sensor was placed on top of the cell into the well on the PEEK part (refer to Figure 4.1.5). After the force sensor was placed into the notch the big screw on top of the compression frame was turned down, using a torque wrench the sensor, until it showed a force of approximately 1 kN. This was to prevent water coming out of the cell. The PEMWE cell was then transported to the test bench.



Figure 4.1.5: PEMWE cell insertion into compression frame.

After integration of the PEMWE cell, the water circulation was started on the anodic side. Thermocouples was inserted into the endplates sense ports and the cell was connected electrically to the power supply.

4.1.3. Investigation of the PEMWE CCM Testing Parameters

4.1.3.1. PEMWE Cell Compression

It has been shown that the cell compression plays an important role in the evaluation of the PEMWE cell performance. In this study, the PEMWE cell compression was varied to investigate its influence on the overall cell performance. This investigation was carried out in a single PEMWE cell at 60 °C, 0.1 L/min water flowrate, and standard pressure using carbon paper PTL on both anode and cathode electrodes sides. The polarisation curves obtained from the PEMWE cell performance tests at various cell compressions are shown in

Figure 4.1.6.

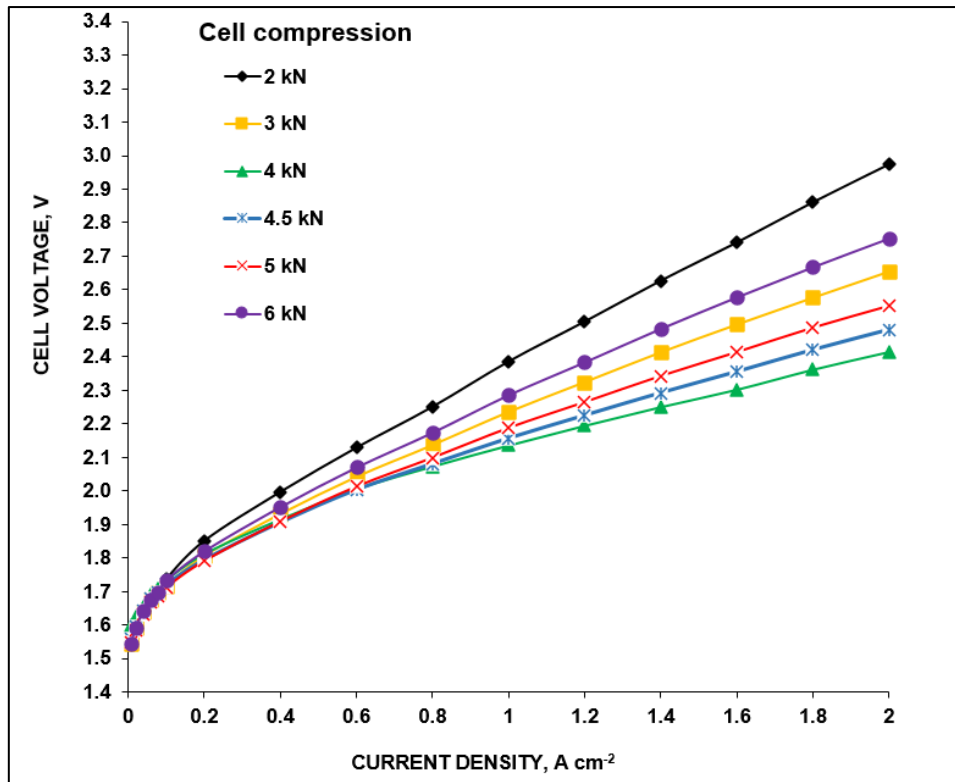


Figure 4.1.6: Current-voltage performance of commercial PEMWE CCMs at different cell compressions. Testing conditions: cell T.= 60°C, cell P = 1 bara, 0.1 L/min water flowrate, carbon paper PTLs.

From

Figure 4.1.6, it can be seen that the PEMWE CCMs tested at 4 kN cell compression provided the best PEMWE cell performance, with 2.136 V at 1 A cm⁻². While at lower cell compressions of 2 kN and 3 kN showed a PEMWE cell performance decrease of 2.386 V, 2.236 V at 1 A cm⁻², respectively. At higher cell compressions of 4.5 kN, 5 kN and 6 kN, the PEMWE cell also showed a performance decrease of 2.157 V, 2.188 V, 2.287 V at 1 A cm⁻², respectively. This can be explained by the reasoning that at lower cell compressions, the contact between the electrode's catalyst layers and PTLs interfaces is insufficient thereby increasing the ohmic resistance of the PEMWE system. At higher cell compression conditions, the porous transport layer structure is crushed resulting in uneven supply and evacuation of water reactant and oxygen gas respectively, thereby also increasing the ohmic and mass transport losses which affect the overall PEMWE cell performance.

This was further confirmed from the electrochemical impedance spectroscopy analysis results obtained from the EIS analysis of the PEMWE cell at varied compression pressures as shown in Figure 4.1.7.

According to Merwe, et al., (2014) the real impedance values obtained from the EIS analysis of PEMWE cell at 0.2 A cm^{-2} at high frequency is influenced primarily by the ohmic overvoltage induced losses. As It can be observed from Figure 4.1.7, the PEMWE system set-up of 2 kN, 3 kN, 4.5 kN, 5 kN and 6 kN cell compression have higher real impedance values of $1.26 \Omega \text{ cm}^{-2}$, $0.916 \Omega \text{ cm}^{-2}$, $0.802 \Omega \text{ cm}^{-2}$, $0.835 \Omega \text{ cm}^{-2}$ and $1.07 \Omega \text{ cm}^{-2}$, respectively. Compared to the PEMWE system of 4 kN cell compression which exhibits the lowest real impedance value of $0.73 \Omega \text{ cm}^{-2}$. Due to its lower ohmic resistance; 4 kN PEMWE cell compression was selected for all subsequent electrochemical evaluations.

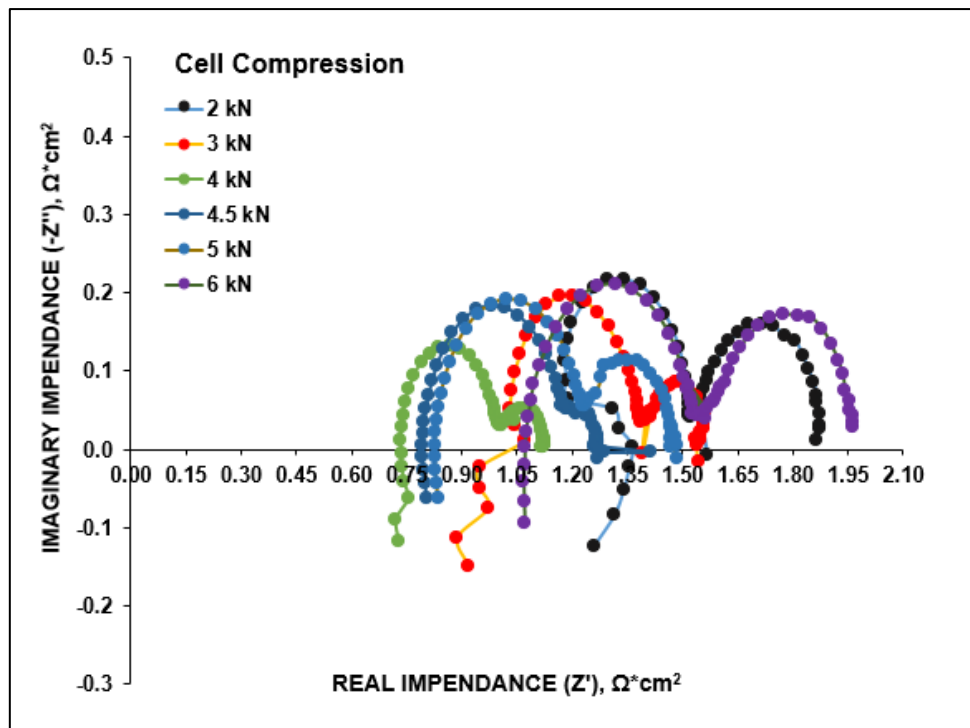


Figure 4.1.7: EIS semicircles of a commercial CCM showing the effects of different cell compressions performed at 0.2 A cm^{-2} . Testing conditions: frequency= 100 mHz to 100 kHz, cell T = 60°C , cell P = 1 bara, 0.1 L/min water flowrate, carbon paper PTLs.

4.1.3.2. PEMWE System Water Flow Rate

In this study, the effects of water flow rate on the overall PEMWE cell performance were investigated. The study was conducted at 60°C and standard pressure, with the cell compression of 4 kN. Due to the electrolyser test station system limitations, only 0.1 L/min and 0.2 L/min water flow rates could be investigated.

Figure 4.1.8 shows the current-voltage performance graphs of commercial CCMs at water flow rate of 0.1 L/min and 0.2 L/min, and their corresponding system temperature gradient during the electrochemical tests. From these graphs, it can be observed that 0.2 L/min water flow rate produced an unsteady cell temperature profile throughout the testing and failed to reach the desired set temperature of 60°C (with the highest system temperature of 53°C) as seen in Figure 4.1.8b. While 0.1 L/min water flow rate system provided a better temperature gradient represented in Figure 4.1.8b with a constant temperature profile.

Furthermore, the 0.1 L/min water flow rate system showed a better cell performance with 2.136 V at 1 A cm⁻² compared to 0.2 L/min water flow rate system which produced 2.196 V at 1 A/cm². This agrees with findings from Dedigama, et al., (2014) and Majasan, et al., (2018) that showed the water flow rate has a significant effect on the PEMWE system performance at low temperature operations ($\geq 70^{\circ}\text{C}$). Additionally, they analysed mass transfer, the heat distribution and current density distribution at the PEMWE electrodes catalyst layers at different water flow rates and found that oxygen void fraction (the volume of the product oxygen occupied in a pore to the total volume of the pore in the catalyst layer) decreased with increasing water flow rate. In addition, they also reported non-uniform distribution of temperature and current density at high water flow rates. These can be attributed to the relationship between the PEMWE system water flow rate and the joule heating effect. The joule heating effect is defined as the rise of thermal energy in a system due to the flow of current (Dedigama, et al., 2014; Majasan, et al., 2018).

It can be concluded that high water flow rates allow for bigger and inconsistent presence of the water reactant at the reaction sites which limit the flow of oxygen products out of the electrode catalyst layer. This results in low reaction rate, low current flow, and catalyst layer flooding thus decreasing the membrane proton conductivity and catalyst layer mass transport promoting high ohmic and mass transport resistance. As a water flow rate of 0.1 L/min showed a positive impact on the PEMWE cell performance, all the ensuing electrochemical evaluations would be performed at this flow rate.

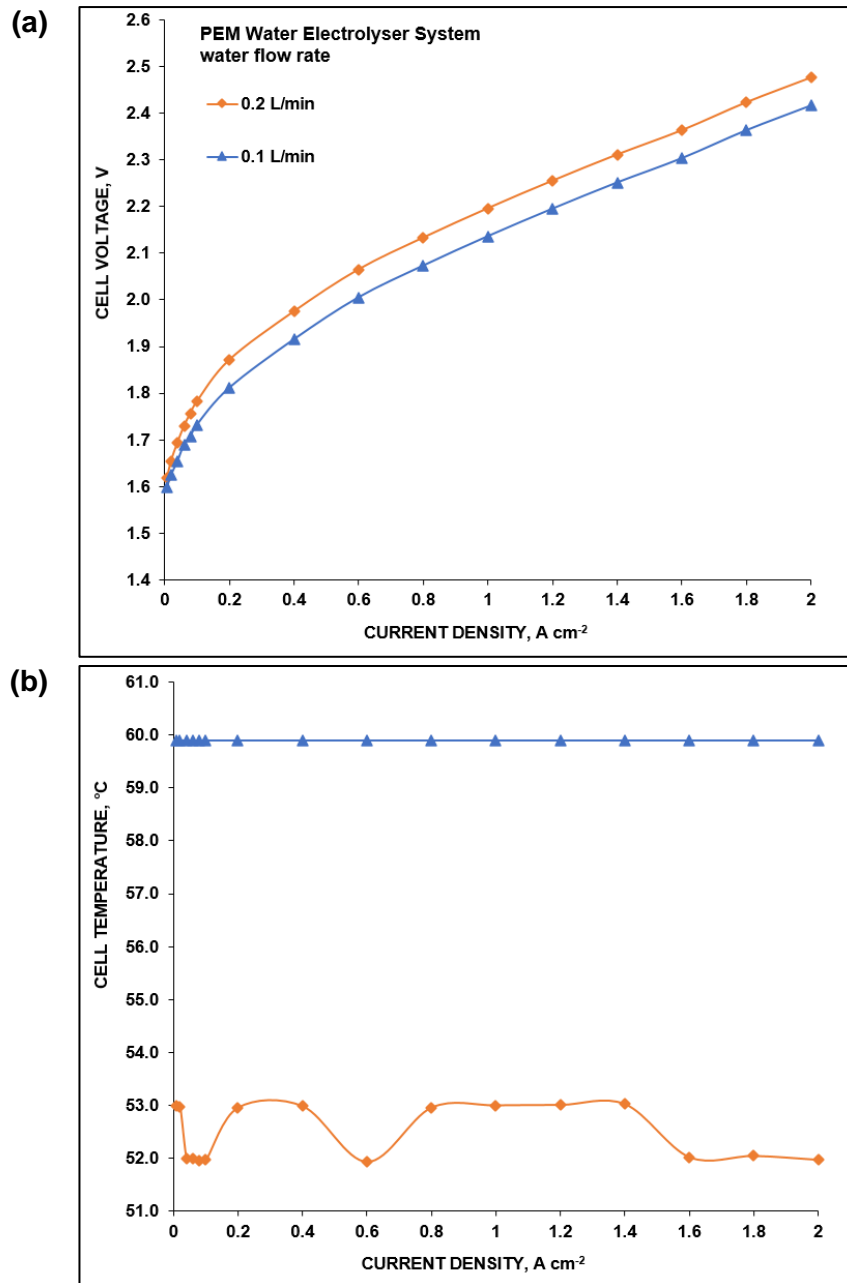


Figure 4.1.8: (a) Current-voltage PEMWE cell performance curves for 0.1 L/min and 0.2 L/min water flow rates with (b) their corresponding temperature gradients. Testing conditions: cell T = 60°C, cell P = 1 bara, cell compression= 4 kN, carbon paper PTLs.

4.1.3.3. PEMWE Porous Transport Layer

Various porous transport layer materials were investigated to determine the PTL material best suited for the in-house PEMWE testing system. Figure 4.1.9 shows the current-voltage performance of the PEMWE cell with different PTL material combinations.

The electrochemical evaluations were conducted in a single PEMWE cell at 60 °C, standard pressure, with a cell compression of 4 kN and 0.1 L/min water flow rate. It was found that the use of Titanium powder sintered PTLs on both the anode and cathode sides provided a better overall electrolysis performance with 1.919 V at 1 A cm⁻². Followed closely by the Platinum coated Titanium PTLs PEMWE cell setting with the performance of 1.946 V and 1 A cm⁻². The use of carbon paper (Toray paper 120, 5wt.%) PTLs or its combination with other PTL materials showed a decrease in cell performance as seen in Figure 4.1.9. This can be attributed to the physical properties and microporous structure of each PTL material.

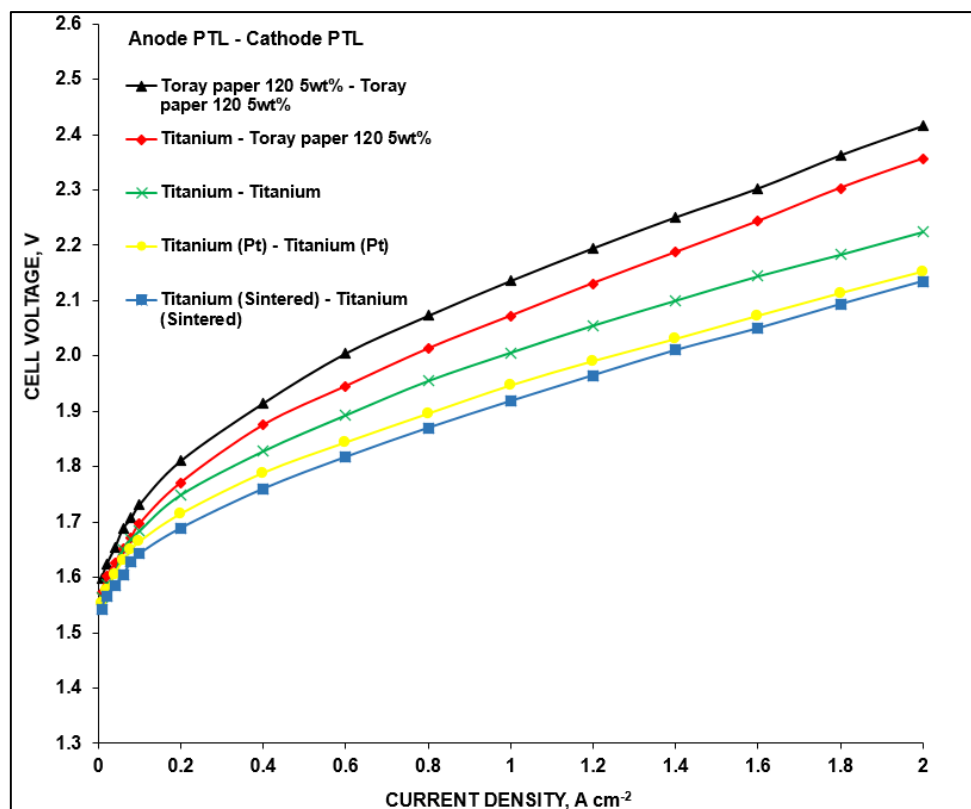


Figure 4.1.9: Current-voltage performance curves of PEMWE cell with different PTL materials. Testing conditions: cell T.= 60°C, cell P.= 1 bara, 0.1 L/min water flowrate.

PTLs made of Titanium materials or Platinum coated Titanium are expected to be less corrosive in acidic media and incompressible compared to carbon PTLs. These allowed Titanium PTLs and Platinum coated Titanium PTLs to generate less resistance resulting in a minimisation of losses caused by ohmic and mass transport resistances as shown in Figure 4.1.10 with the real impedance values of 0.73 Ω cm⁻², 0.68 Ω cm⁻², 0.578 Ω cm⁻², 0.519 Ω cm⁻² and 0.32 Ω cm⁻² for the Cell PTLs combinations of carbon, titanium - carbon, titanium,

platinum coated titanium and titanium sintered PTLs, respectively. This is in agreement with findings from Metz, et al., (2019).

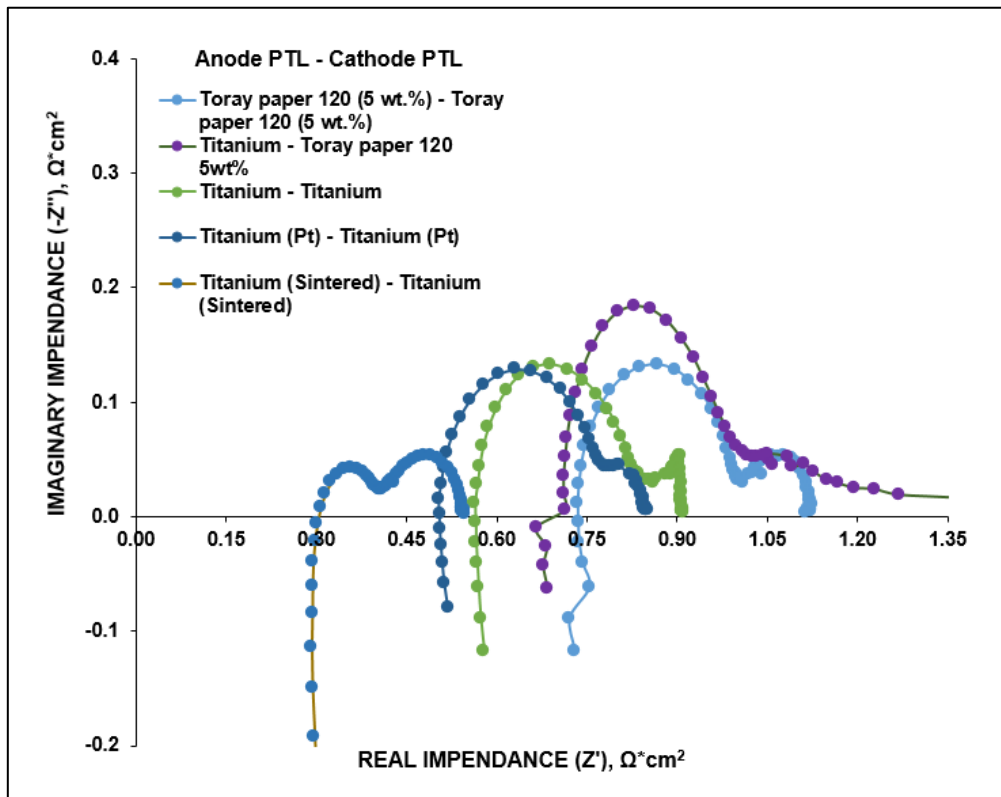


Figure 4.1.10: EIS semicircles of PEMWE cell showing the effects of different PTLs combinations performed at $0.2 \text{ A}\cdot\text{cm}^{-2}$. Testing conditions: frequency= 100 mHz to 100 kHz, cell T = 60°C , cell P = 1 bara, 0.1 L/min water flowrate.

Despite providing the best performance, Titanium powder sintered PTLs were not used in the subsequential PEMWE electrochemical evaluations due to their limited availability in the lab and its difficulties at being downsized. Instead, platinum coated titanium PTLs were selected as they provided the closest performance to titanium sintered material at higher current densities and were easily malleable.

4.1.4. PEMWE Cell Conditioning and Current-Voltage Measurement Parameters

The cell conditioning and electrochemical performance measurement procedure used thus far in this study is based on the published work from Bender G et al., (2019).

However, the effects of different electrolyser cell conditioning and evaluation measurement parameters on the overall PEMWE performance are still not well understood. In this section, the cell conditioning and current-voltage measurement parameters were varied to better understand their impacts on the PEMWE cell performance and consequently develop an optimised PEMWE cell conditioning and measurement process for in-house testing. This investigation was carried out in a single PEMWE cell at 60 °C, 0.1 L/min water flowrate, and standard pressure using titanium sintered PTL on both anode and cathode electrodes sides. Figure 4.1.11a shows the polarisation curves obtained from the investigation of various PEMWE cell conditioning and current-voltage measurement steps times. The details of the parameters investigated are summarised in Table 4.1.3.

From the polarisation curves (refer to Figure 4.1.11a), it can be noticed that for the cell activation steps at 1.7 V for 4 hours, 0.2 A cm⁻² and 1 A cm⁻² for 5 min (FCA-2) provided the lower performance of 1.949 V at 1 A cm⁻². While the cell activation steps at 1.7 V for 4 hours, 0.2 A cm⁻² and 1 A cm⁻² for 15 min (FCA-3), 0.2 A cm⁻² and 1 A cm⁻² for 30 min (FCA-1), and 0.2 A cm⁻² and, 1 A cm⁻² for 45 min (FCA-4) showed no significant differences in the cell performance with 1.918 V, 1.919 V and 1.92 V at 1 A cm⁻², respectively as seen in Figure 4.1.11a. Furthermore, when the activation step time at 1.7 V was decreased from 4 hours to 2 hours, 0.2 A cm⁻² and 1 A cm⁻² for 15 min (FCA-5) and 0.2 A cm⁻² and 1 A cm⁻² for 30 min (FCA-6), the PEMWE cell still showed no significant differences in performance with 1.917 V and 1.919 V at 1 A cm⁻², respectively.

The analysis of the performance profile of different conditioning and measurement parameters, as seen in Figure 4.1.11b, showed that the PEMWE systems at 1.7 V for 4 hours, 0.2 A cm⁻² and 1 A cm⁻² activation steps for 5 min and 0.2 A cm⁻² and 1 A cm⁻² activation steps for 45 min were not able to stabilise over time. While the PEMWE systems at 1.7 V for 2 hours, 0.2 A cm⁻² and 1 A cm⁻² activation steps of 15 min and 0.2 A cm⁻² and 1 A cm⁻² activation steps of 30 min reached steady state then deteriorated afterwards. However, the addition of the OCV activation step for 5 min to the 1.7 V for 2 hours activation step and the decrease in the measurement interval time from 5 min to 2.5 min to 0.2 A cm⁻² and 1 A cm⁻² for 15 min activation steps (FCA-7) showed the best cell performance of 1.777 V at 1 A cm⁻². Furthermore, the analysis of the performance profile of CCM FCA-7 showed the PEMWE system achieved performance stability from the start of the electrolysis test.

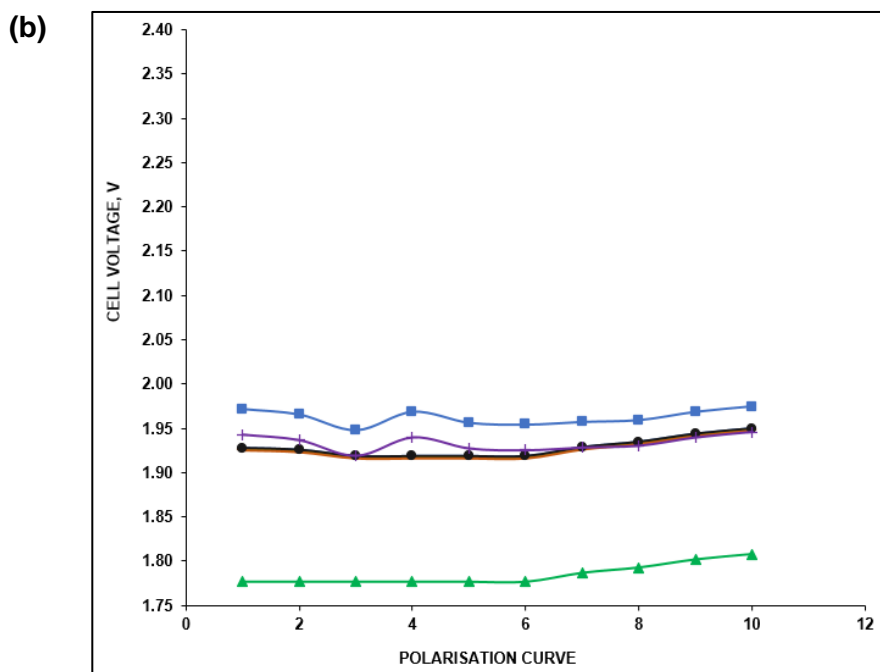
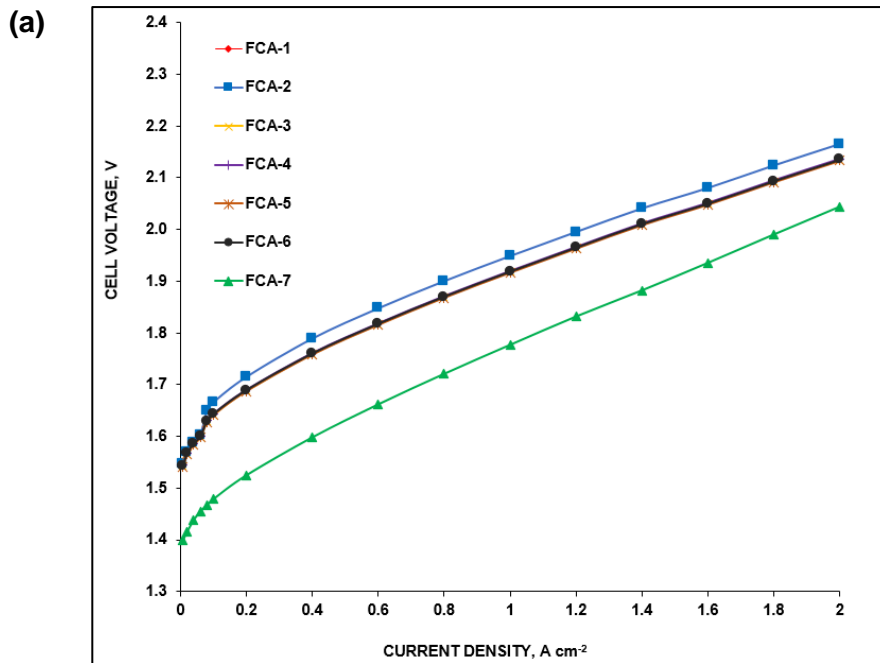


Figure 4.1.11: (a) Polarisation curves of PEMWE cell with different cell conditioning and I-V measurement parameters and (b) their corresponding performance profiles throughout the I-V test. Testing conditions: cell T = 60°C, cell P = 1 bara, 0.1 L/min water flowrate, Titanium (Pt-coated) PTLs.

Table 4.1.3: Summary of commercial CCMs with their corresponding cell conditioning and I-V measurement parameters investigated.

Commercial CCM Code	Cell Conditioning (Investigated Steps in min)				I-V Measurement (Investigated Pol Curve Interval in min)
	0 A cm ⁻²	0.2 A cm ⁻²	1 A cm ⁻²	1.7 V	
FCA-1	0	30	30	240	5
FCA-2	0	5	5	240	5
FCA-3	0	15	15	240	5
FCA-4	0	45	45	240	5
FCA-5	0	15	15	120	5
FCA-6	0	30	30	120	5
FCA-7	5	15	15	120	2.5

4.2. Commercial PEMWE CCMs Benchmarking

With the testing parameters and measurement protocols optimised, a commercial CCM benchmarking with known electrochemical performance was conducted to evaluate the accuracy and reproducibility of the developed current-voltage characterisation with respect to water electrolysis performance evaluation. 4 identical commercial CCMs of N115 membrane, catalyst loadings of 2 mg_{Ir} cm⁻² for the anode and 1 mg_{Pt} cm⁻² for cathode were used for this study. The physical characterisation of the commercial anode catalyst layer was performed using SEM.

4.2.1. Physical Characterisation

The structure of the commercial CCM anode electrode catalyst layers was examined by means of the scanning electron microscopy (SEM) at $\sim 1 \times 10^{-5}$ mbar. The anode electrode catalyst layer physical characterisation protocols used in this study were obtained from HySA Catalysis internally developed procedure by Mawungwe, et al., (2022) using the FEI NovaNano SEM 450. The anode electrode catalyst layer surface and cross-sectional structured were evaluated as the following:

- For the catalyst layer surface, the images were recorded using the SE detector to capture enhanced compositional contrast images showcasing the difference between iridium and support materials.
- For the catalyst thickness, the cross-sectional cuts of the samples were embedded in epoxy, polished then imaged using a backscatter electron detector to create a cross-sectional image for thickness evaluation.

The SEM surface and cross-section images of the commercial anode catalyst layer are shown in Figure 4.2.1. From the SEM image, it can be seen that the commercial anode electrode from the commercial CCM has a homogeneous surface and contains catalyst nanoparticle agglomerates that are uniformly distributed across the catalyst layer.

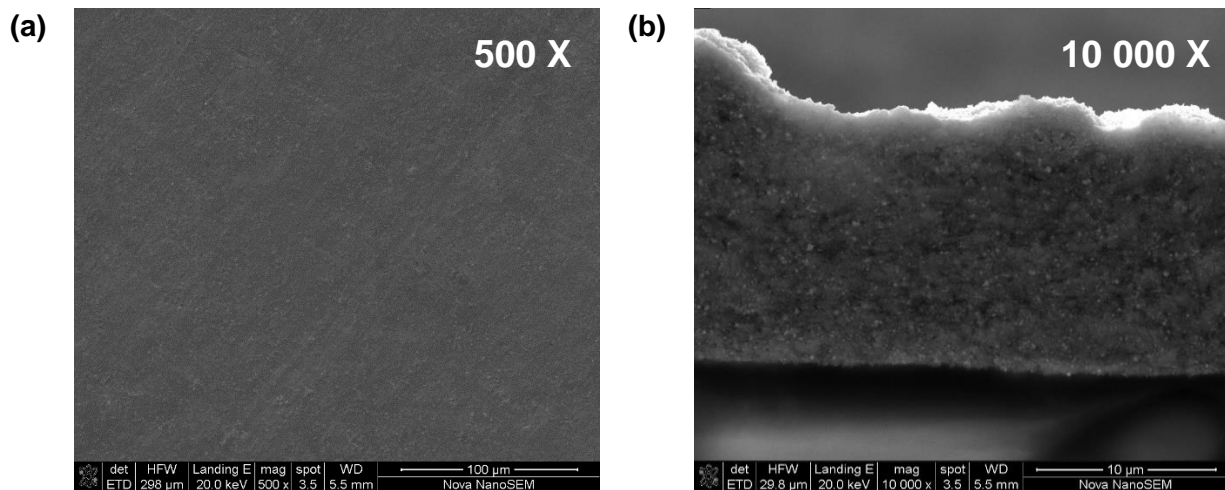


Figure 4.2.1: SEM images of a commercial CCM anode catalyst layer with (a) catalyst layer surface and (b) catalyst layer cross section.

4.2.2. Electrochemical Characterisations

The electrochemical characterisation of the commercial CCMs was conducted in a single PEMWE cell at 60°C and standard pressure, with a cell compression of 4 kN and 0.1 L/min water flow rate, using Pt coated titanium PTLs on both cathode and anode sides. The I-V measurement was done following the optimised electrochemical characterisation procedures developed in this study. The electrochemical characterisation of the commercial CCMs was conducted as follows: once the desired temperature was reached and stable, the system's circuit was opened, and its corresponding voltage was allowed to reach the theoretical cell voltage for a PEM water electrolysis single cell for 2.5 min.

Then after a 0.2 A cm^{-2} current density was applied to the cell for 15 min. Next, 1.0 A cm^{-2} for another 15 min. Then the PEMWE cell was operated at a constant voltage of 1.7 V for 120 min. Afterward, I-V performance curves were measured using 2.5 min steps. Starting from open circuit the current was increased in 0.02 A cm^{-2} steps up to 0.1 A cm^{-2} . The next was 0.2 A cm^{-2} and current densities were stepped up in 0.2 A cm^{-2} steps until a maximum current density of 2 A cm^{-2} was reached. Current densities were stepped down again, using the same current density steps. The applied current densities and their corresponding voltage responses were automatically recorded. The electrochemical evaluation procedures used to characterise the commercial CCMs are summarized in Table 0.3 (Appendix).

Figure 4.2.2 shows the polarisation curves of the commercial CCMs from the benchmarking study. It is clear that the current-voltage testing method developed in this study produced precise and reproducible performance results as the total standard deviations was of 10 mV. Also, when compared to the manufacturer performance data, it was found that the I-V evaluation method produced accurate and reliable results with performance at 1 A cm^{-2} of 1.709 V and 1.708 V from the in-house tests and manufacturer data, respectively.

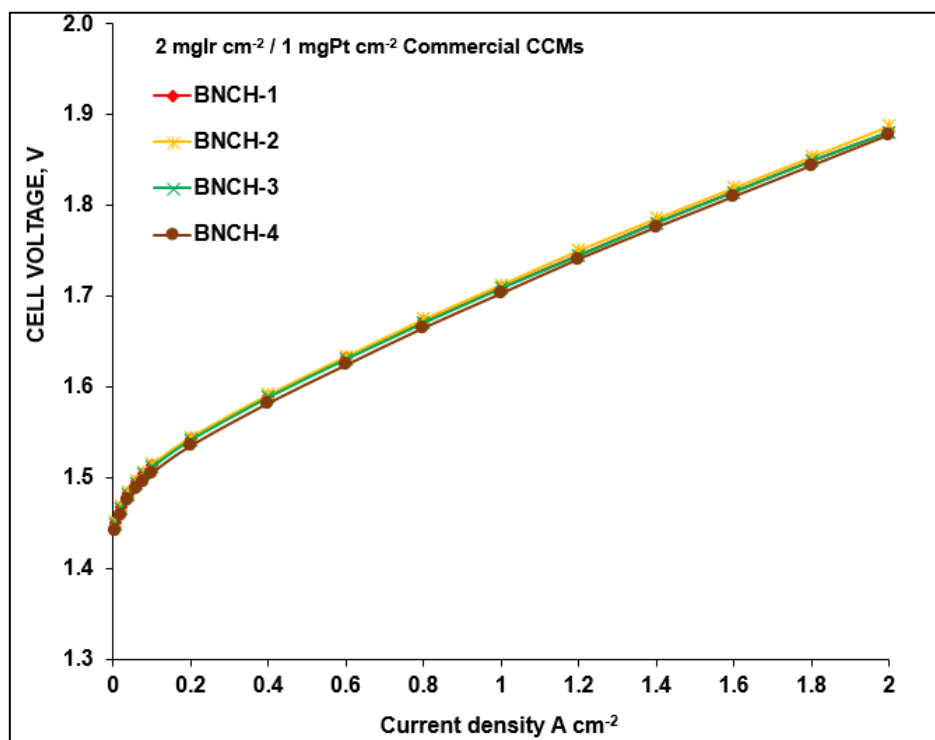


Figure 4.2.2: Current-voltage performance graphs of N115 commercial CCMs from in-house benchmarking results. Testing conditions: cell T = 60°C , cell P = 1 bara, 0.1 L/min water flowrate, Titanium (Pt) PTLs.

The electrochemical impedance spectroscopy test was conducted at 0.2 A cm^{-2} after the current-voltage performance measurements for each commercial CCM sample. Using an Autolab PGSTAT100 potentiostat under a current perturbation of $\pm 5\%$ and frequency range of $100 \text{ kHz} - 100 \text{ mHz}$. The HFR is then obtained from the high-frequency intercept with the real axis in a Nyquist plot. The EIS results of the commercial CCMs are shown in Figure 4.2.3.

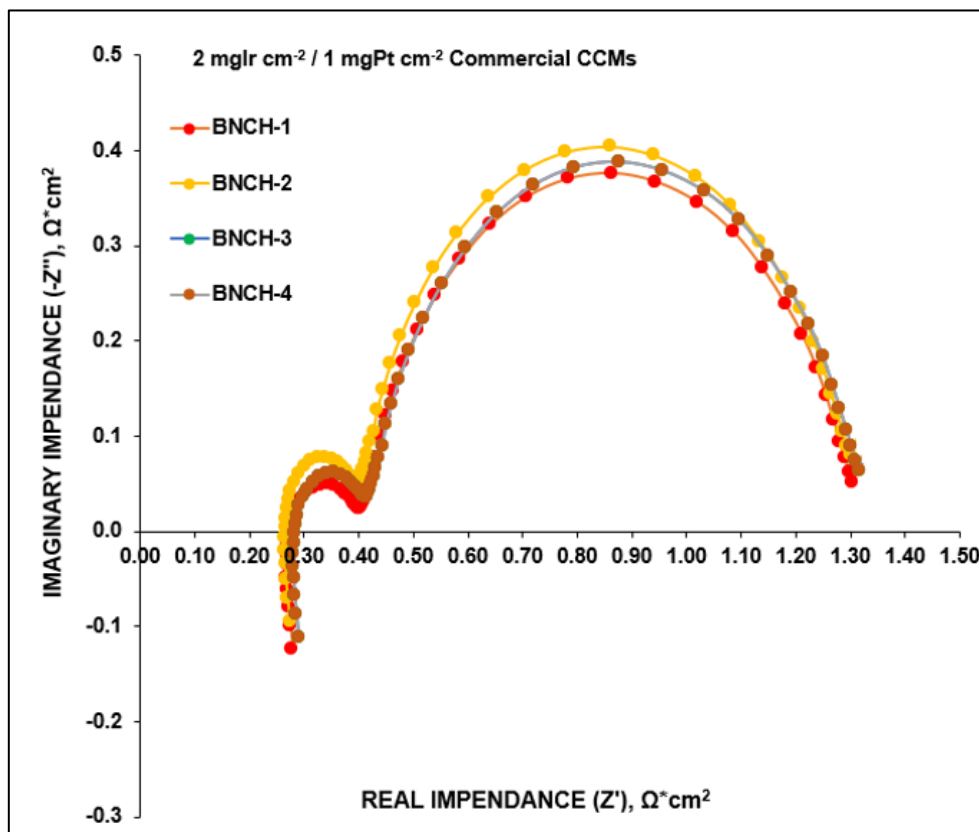


Figure 4.2.3: The electrochemical impedance spectra of commercial CCMs conducted at 0 A cm^{-2} . Testing conditions: frequency= 100 mHz to 100 kHz , cell $T = 60^\circ\text{C}$, cell $P = 1 \text{ bara}$, 0.1 L/min water flowrate, Titanium (Pt) PTLs.

For the EIS measurements, the data shows that precise and reproducible EIS results can be collected. However, measured values were expected in the range below $0.15 \text{ } \Omega \cdot \text{cm}^2$ at 60°C . Results measured in our lab using our instrument and protocols were on average about 2 times higher. It is apparent by the electrochemical impedance spectra of commercial CCMs, as shown in Figure 4.2.3, that the measured HFRs data collected so far in this study may not represent actual variations of the cell resistances. This can be attributed to erroneous cell assembly procedure and instrument specifics (Bender, et al., 2019).

Investigations into the cell wiring setup, EIS instrument software and measurement protocols were insufficient to mitigate the erroneous data. Therefore, it was decided not to perform EIS tests for the pore forming additives effects study as more work is required to identify the proper equipment and measurement protocols to perform accurate, reliable, and meaningful HFR and EIS data measurements.

4.3. Chapter Summary

In this chapter, experimental procedures developed for the electrochemical characterisation of the PEMWE system is presented. Two different commercial CCMs were used to investigate the effects of various electrochemical evaluation parameters and conditions on the performance measurements accuracy and reproducibility. A commercial CCM of Nafion 115 membrane with catalyst loadings of $3 \text{ mg}_{\text{IrRuOx}} \text{ cm}^{-2}$ for the anode electrode and $3 \text{ mg}_{\text{Pt}} \text{ cm}^{-2}$ for the cathode electrode, and a commercial CCM of Nafion 115 membrane with $2 \text{ mg}_{\text{Ir}} \text{ cm}^{-2}$ and $1 \text{ mg}_{\text{Pt}} \text{ cm}^{-2}$ for the anode and cathode loadings were used for the current-voltage testing protocols development and CCMs benchmarking studies, respectively.

For the cell compression study, it was found that 4 kN cell compression provided the best cell performance with 2.136 V at 1 A cm^{-2} . At lower cell compressions of 2 kN and 3 kN and higher cell compression of 6 kN the PEMWE performance decreased with 2.386 V, 2.236 V and 2.287 V at 1 A cm^{-2} , respectively compared to 4 kN cell compression. The investigation of the influence of water flow rate in PEMWE system showed that the water flow rate has a significant effect on the PEM system performance at low temperature operations. As the 0.2 L/min water flow rate produced an overall unsteady cell temperature profile and lower CCM performance while 0.1 L/min water flow rate generates better temperature gradient and overall CCM performance. The porous transport layer investigation showed that the titanium powder sintered PTLs on anode and cathode sides provided a better overall electrolysis performance in-house with 1.919 V at 1 A cm^{-2} followed closely by the platinum coated titanium PTLs performance with 1.946 V at 1 A cm^{-2} . While the carbon paper (Toray paper 120 5 wt.%) PTLs showed a decrease in performance at high current densities with 2.136 V and 2.416 V at 1000 mA cm^{-2} and 2000 mA cm^{-2} , respectively.

Furthermore, the effects of various PEMWE cell conditioning and I-V evaluation measurement parameters on the overall cell performance were investigated. It was found that the cell activation steps at 1.7 V for 4 hours, 0.2 A cm^{-2} and 1 A cm^{-2} for 5 min produced the lower performance with 1.949 V at 1 A cm^{-2} while the cell activation steps at 1.7 V for 4 hours, 0.2 A cm^{-2} and 1 A cm^{-2} of 15 min, 30 min and 45 min showed no significant differences in the cell

performance. The analysis of the PEMWE systems performance profiles showed that the cell performances at 1.7 V for 4 hours, 0.2 A cm⁻² and 1 A cm⁻² activation steps for 5 min and 45 min with 4 hours were unable to reach performance stabilisation during the I-V tests. The addition of the OCV step for 5 min and the change in the measurement interval time from 5 min to 2.5 min to 1.7 V for 2 hours, 0.2 A cm⁻² and 1 A cm⁻² for 15 min activation steps provided the best cell performance of 1.777 V at 1 A cm⁻² and improved significantly the cell stability over time.

To ensure that the optimised electrochemical evaluations developed in this study is accurate and reproducible, a commercial CCM benchmarking test was conducted. It was found that the current-voltage testing method developed in this study provided precise, accurate and reproducible performance results as the total standard deviation from the commercial PEMWE cell performance at 1 A cm⁻² was ~10 mV with 1.709 V, 1.709 V and 1.708 V, respectively. However, EIS measurements obtained in our lab using our instrument and protocols were on average about 2 times higher than the expected published values. Showing that the HFRs data collected may not represent actual variations of the cell resistances. Therefore, it was decided not to continue with the electrochemical evaluation of the fabricated PEMWE electrodes as more work is required to identify the proper equipment and measurement protocols to perform accurate, reliable, and meaningful HFR and EIS data measurements.

CHAPTER 5 EFFECTS OF PORE FORMING ADDITIVES ON THE PEMWE ANODE ELECTRODE CATALYST LAYER

Pores in the catalyst layer provide structural configuration that promote water electrolysis with improved reaction kinetics, pathways for electrons and protons transport, and networks for water reactant delivery and oxygen gas management. These can contribute to the increase of the utilisation of electrocatalysts in an electrode, lowering the quantity of noble metal required, and the decrease of resistances within the electrode catalyst layer, lowering the energy requirement of PEMWE system further contributing to the development of efficient and low cost PEMWE technology. In this chapter, findings obtained from the addition of pore forming substances into the anode electrode catalyst ink formulation and its effects on the catalyst layer structure and overall cell performance are presented and discussed.

5.1. Highly Porous Anode Catalyst Layer on a Thin Proton Exchange Membrane

The electrode samples were fabricated using the optimised parameters and conditions for Mayer Rod method discussed in Chapter 3. The anode electrodes all contained 11.6 wt.% ionomer, with the catalyst loadings of $1.01 \text{ mg}_{\text{Ir}} \text{ cm}^{-2}$ for anode electrodes without pore formers and $1.016 \text{ mg}_{\text{Ir}} \text{ cm}^{-2}$ and $0.39 \text{ mg}_{\text{Ir}} \text{ cm}^{-2}$, $1.013 \text{ mg}_{\text{Ir}} \text{ cm}^{-2}$ and $0.39 \text{ mg}_{\text{Ir}} \text{ cm}^{-2}$ for anode electrodes with pore forming material of $\text{IrO}_x\text{-TiO}_2$ weight ratio of 1:1 and 1:10 for ammonium carbonate and 1:1 and 1:10 ammonium bicarbonate, respectively.

5.1.1. Anode Catalyst Layer Physical Characterisation

The SEM was used to investigate the fabricated anode electrodes catalyst layers structures and porosities.

5.1.1.1. Anode Catalyst Layer Structure

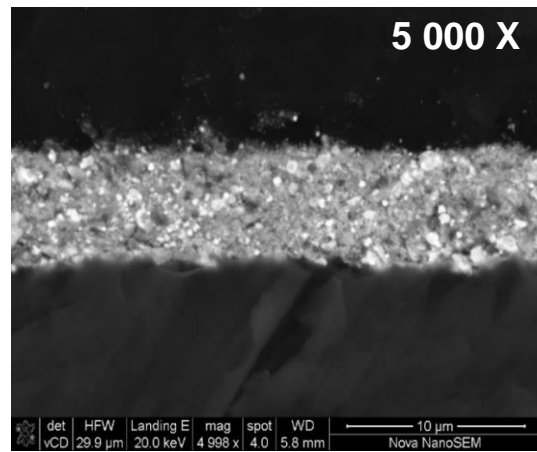
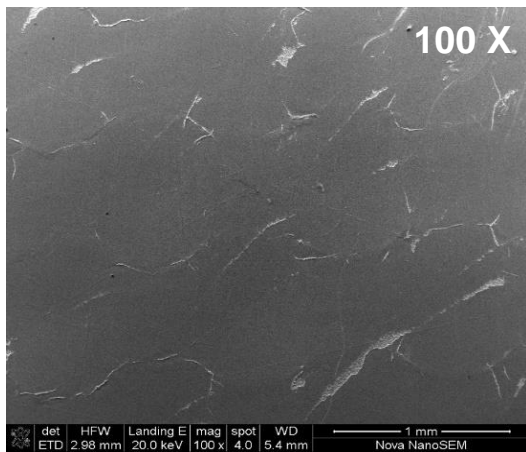
Figure 5.1.1 shows the SEM surface and cross-section images of the $\text{IrO}_x\text{-TiO}_2$ anode catalyst layer from various CCM samples prepared for the investigation of the effects of pore forming additives on the anode electrode catalyst layer's morphology. It can be seen that the addition of pore formers produced inhomogeneities in the catalyst layer surface morphology. Anode catalyst layers of 1:1 pore forming substance to catalyst weight ratio had the most visible cracks compared to the anode electrodes catalyst layers of 1:10 pore forming substance to

catalyst weight ratio and without pore forming additives, which produced uniform catalyst layers.

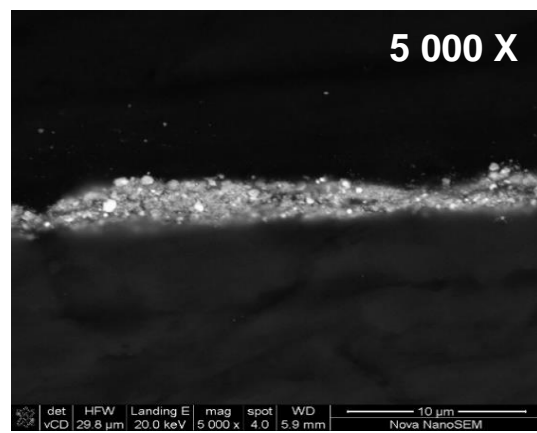
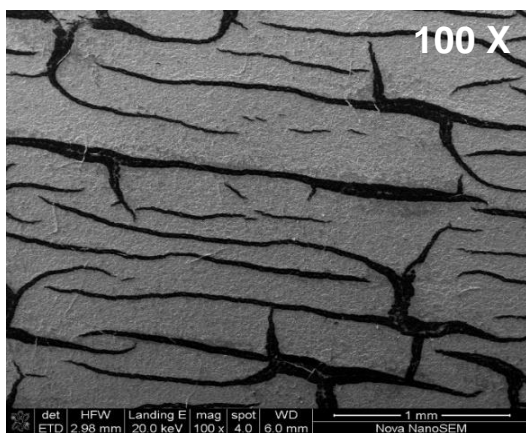
Furthermore, from the cross-sectional SEM images of the catalyst layers, as shown in Figure 5.1.1, it is noticeable that the anode catalyst inks containing the largest amount of pore forming additives produced anode electrodes catalyst layers structures with a large number of IrO_x-TiO₂ catalyst aggregates and an uneven distribution of the agglomerates compared to the ones with a lower amount of pore forming additives and without pore forming additives. However, it was also observed that the anode electrodes with ammonium bicarbonate showed fewer cracks on the catalyst layer surface, and they had smaller catalyst aggregates and showed better distribution of catalyst nanoparticle agglomerates compared to anode electrodes with ammonium carbonate (refer to Figure 5.1.1).

The presence of surface inhomogeneity in the anode electrodes with pore forming substances may result from the decal transfer process. As the pore forming substances decompose through pyrolysis, they leave voids in catalyst layer structure therefore creating cracks on the surface. The uneven distribution of the catalyst agglomerates can be explained as the addition of pore forming substances into the anode catalyst ink formulations that prevents the effective break-up of catalyst aggregates and the reduction of catalyst agglomerates sizes. This creates catalyst inks with large catalyst aggregates and unevenly dispersed catalyst agglomerates resulting, after coating, in catalyst layers structures with large catalyst aggregates and catalyst layer surface areas with concentrated catalyst nanoparticles agglomerates.

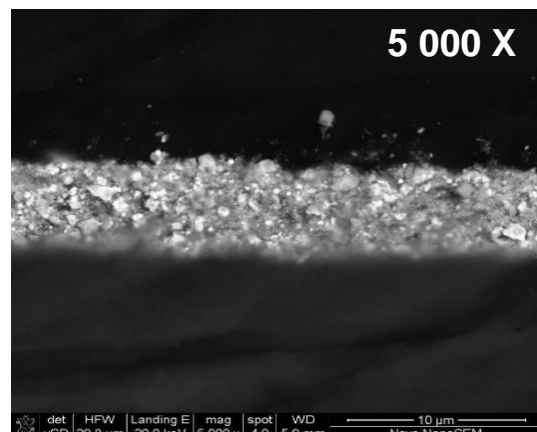
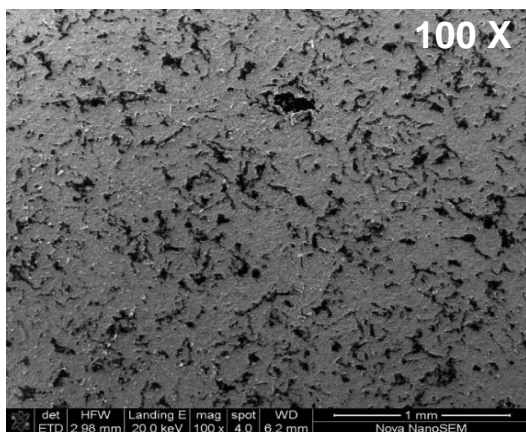
CCM without pore forming material



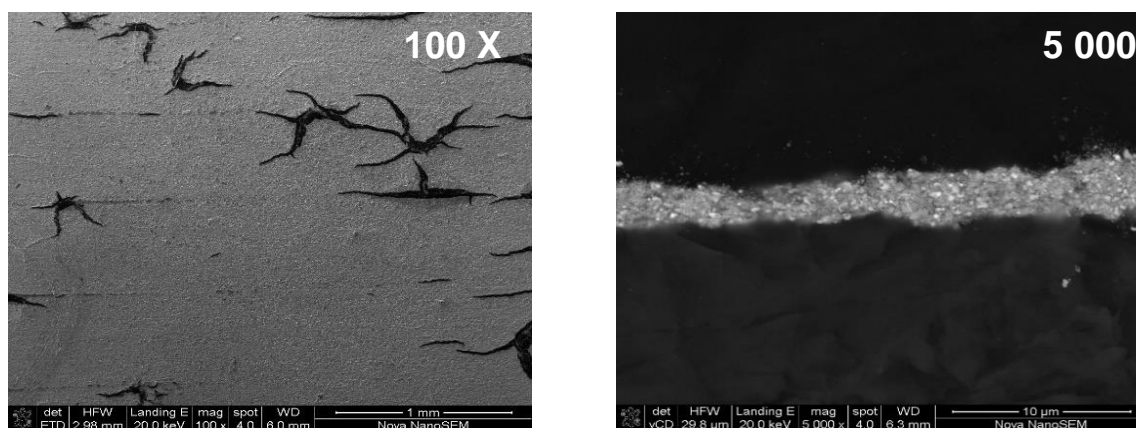
CCM with 1:1 Ammonium carbonate to IrO_x-TiO₂ catalyst weight ratio



CCM with 1:10 Ammonium carbonate to IrO_x-TiO₂ catalyst weight ratio



CCM with 1:1 Ammonium bicarbonate to IrO_x-TiO₂ catalyst weight ratio



CCM with 1:10 Ammonium bicarbonate to IrO_x-TiO₂ catalyst weight ratio

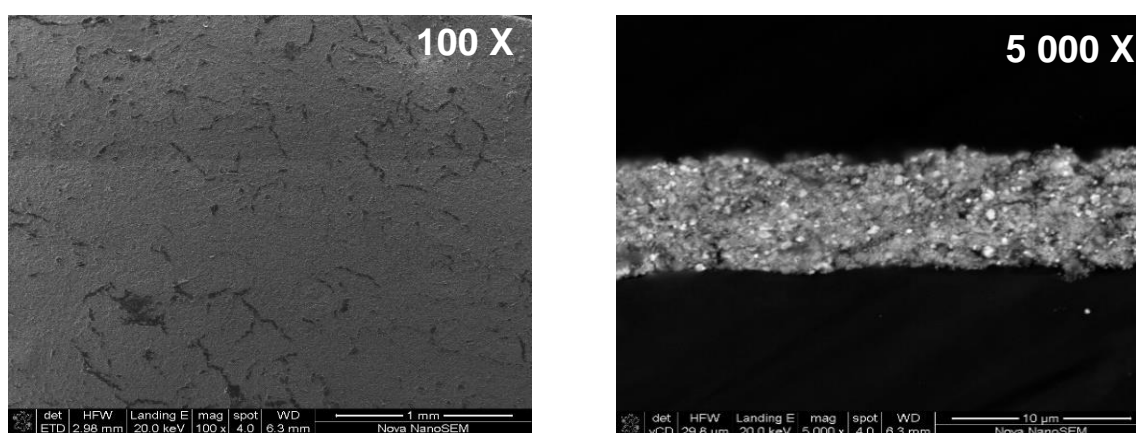


Figure 5.1.1: SEM images of IrO_x-TiO₂ anode catalyst layer surface and cross-section obtained from N212 CCM samples without pore formers and with ammonium carbonate at varying pore former to catalyst mass ratio.

To determine the catalyst layer thickness, cross-sectional SEM images at 5000x magnification from epoxy embedded CCMs were used along with an internally developed image processing procedure using ImageJ™ software. Table 5.1.1 contains the summary of CCM samples anode catalyst layers physical properties including their thicknesses. From Table 5.1.1, It can be seen that all catalyst coated membranes with the anode catalyst loading of $1.13 \pm 0.03 \text{ mgIr cm}^{-2}$ have an anode catalyst layer thickness of $6.3 \pm 0.02 \text{ } \mu\text{m}$. This is in agreement with the expected electrode thickness of $12 \pm 1 \text{ } \mu\text{m}$ for an iridium loading of $2 \pm 0.25 \text{ mgIr cm}^{-2}$ (Bernt & Gasteiger, 2016). The high average standard deviation observed from the calculations of the anode electrodes thickness films of anode electrode catalyst layer with 1:1 pore forming substance to IrO_x-TiO₂ anode catalyst showed that their catalyst layer structures were inhomogeneous, further supporting the observations deduced from the SEM analysis of anode electrodes catalyst layers.

Table 5.1.1: Summary of anode electrode catalyst layer physical properties for all fabricated N212 CCM samples.

CCM	Catalyst Loadings, mg cm ⁻²		Anode Catalyst Layer Specifications	
	Anode	Cathode	Thickness, μm	Standard Deviation (n = 5), μm
Sample-1	1.01	0.87	6.3	0.3
Sample-2	0.39	0.85	2.1	1.1
Sample-3	1.013	0.86	6.3	0.5
Sample-4	0.39	0.85	2.1	1.03
Sample-5	1.016	0.85	6.3	0.7

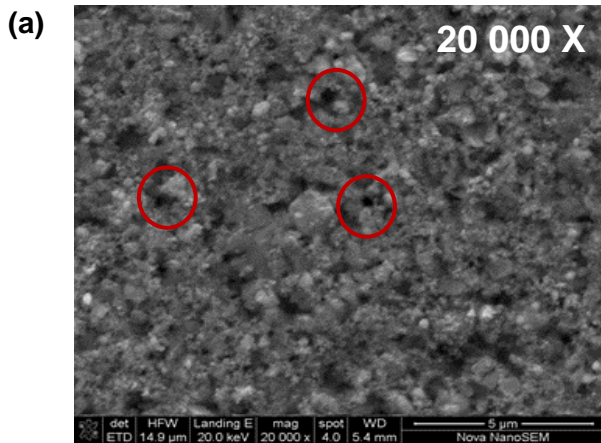
5.1.1.2. Anode Catalyst Layer Porosity

The porosity of the prepared anode electrodes was examined using the SEM images of their catalyst layer surfaces as shown in Figure 5.1.2. Furthermore, mathematical equations, used by Bernt and Gasteiger (2016), were employed to calculate the volume fractions of the catalyst and ionomer of each anode electrode catalyst layer prepared. The values obtained were used to determine the pore quantity in the respective anode electrode catalyst layer. The mathematical equation used is as follows:

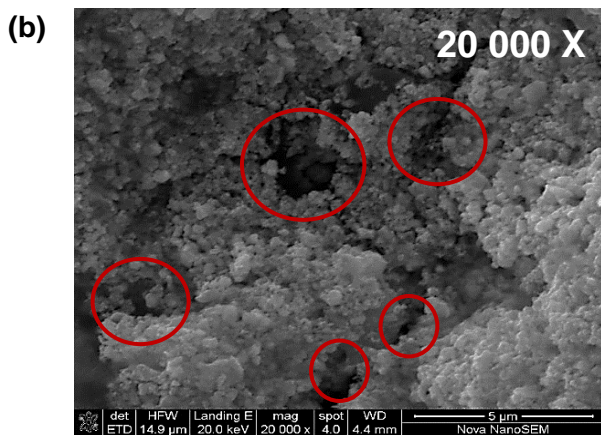
$$V = \frac{L}{\rho \times t_{an}} \quad (1-19)$$

Where V is the volume fraction, L is the weight percentage, ρ is the average density of the catalyst layer component. t is the thickness of the anode electrode. Results from the calculations are presented in Table 5.1.2.

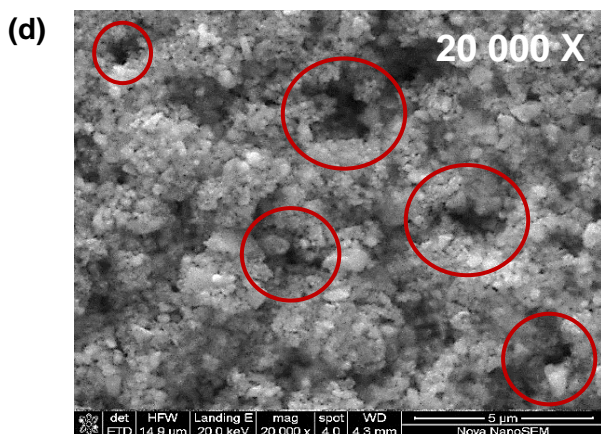
No Pore forming Substance



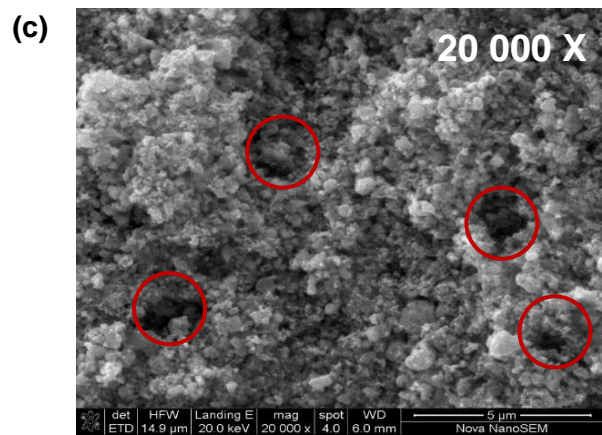
CCM with 1:1 Ammonium carbonate to IrO_x-TiO₂ catalyst weight ratio



CCM with 1:1 Ammonium bicarbonate to IrO_x-TiO₂ catalyst weight ratio



CCM with 1:10 Ammonium carbonate to IrO_x-TiO₂ catalyst weight ratio



CCM with 1:10 Ammonium bicarbonate to IrO_x-TiO₂ catalyst weight ratio

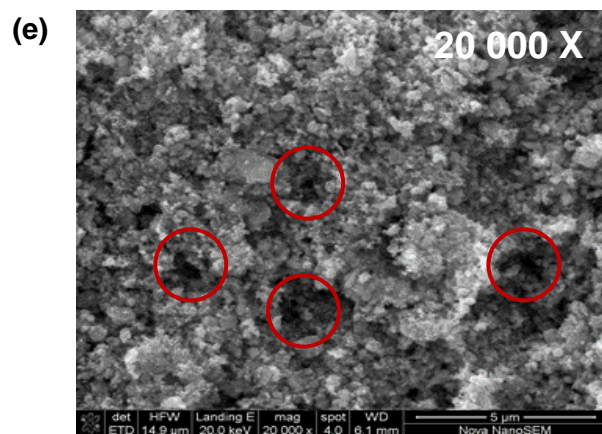


Figure 5.1.2: SEM images of IrO_x-TiO₂ anode electrode surface showing catalyst layer porosity obtained from Nafion 212 CCM samples without pore formers and with ammonium carbonate and ammonium bicarbonate at varying pore forming substance weight ratio.

Table 5.1.2: Summary of anode electrode catalyst layer component volume fraction for the prepared Nafion 212 CCM sample.

CCM	Pore Forming Additives		Anode Catalyst Layer volume fraction		
	Type	Weight pore forming material to anode electrode catalyst	Ionomer	IrO _x -TiO ₂	Pore
Sample-1	No pore former	No pore former	0.2	0.4	0.3
Sample-2	(NH ₄) ₂ CO ₃	1:1	0.15	0.11	0.74
Sample-3	(NH ₄) ₂ CO ₃	1:10	0.3	0.25	0.45
Sample-4	NH ₄ HCO ₃	1:1	0.2	0.15	0.75
Sample-5	NH ₄ HCO ₃	1:10	0.2	0.3	0.4

From Figure 5.1.2 and Table 5.1.2 it can be seen that an increase of porosity (pore size, pore quantity and pore distribution) in the anode catalyst layer was achieved in this study. From the SEM images of the anode catalyst layer surfaces and pore volume fraction results, it can be noticed that the addition of pore forming substances increased the quantity of pores in the catalyst layer by 2.5-fold (from 30% to $74 \pm 1\%$ of the total catalyst layer volume) and ≈ 1.3 -fold (from 30% to $45\% \pm 0.5\%$ of the total catalyst layer volume) for pore forming materials to catalyst weight ratios of 1:1 and 1:10, respectively. Furthermore, from the anode electrode SEM surface images it appears that the catalyst layer mesopore size and their amount are linked to the quantity of pore forming substance added to the catalyst ink formulation. As shown in Figure 5.1.2 the catalyst layer structure of 1:1 pore forming additives to catalyst weight ratios exhibited the formation of more mesopores compared to the catalyst layer structure with 1:10 pore forming additives to catalyst weight ratios. Ammonium carbonate formed bigger mesopores than ammonium bicarbonate as shown in Figure 5.1.2. Also, the anode electrode catalyst layer with 1:10 pore forming additives to catalyst weight ratio had a well distributed porosity in its structure compared to the anode electrode catalyst layer with 1:1 pore forming additives to catalyst weight ratio.

5.1.2. PEMWE Current-Voltage Performance

In this section the current-voltage performance evaluation of the prepared all CCM samples is presented and discussed. The current density of 1 A cm^{-2} is used as a performance metric in this discussion because it is high enough to be relevant at analysing the relationship between anode catalyst layer structure and overall cell performance and can be reached at reasonably low cell voltages with CCM samples that contain low iridium loadings. Figure 5.1.3 & Figure 5.1.4 show the current-voltage plots of the CCMs with and without pore forming additives, tested under optimised testing protocols developed and discussed in Chapter 4. It can be seen that the addition of pore forming material at 1:10 pore forming additives to catalyst weight ratio improved the cell voltage from 2.163 V anode electrode without pore forming additives (refer to Figure 5.1.3) to 2.009 V and 1.954 V at 1 A cm^{-2} for ammonium carbonate and ammonium bicarbonate (refer to Figure 5.1.4), respectively. Anode electrodes with ammonium bicarbonate performed better than ammonium carbonate at both 1:1 and 1:10 pore forming additives to catalyst weight ratios. With 1:1 and 1:10 ammonium bicarbonate to catalyst weight ratios performance of 2.217 V and 1.954 V, respectively; and 1:1 and 1:10 ammonium carbonate to catalyst weight ratios performance of 2.272 V and 2.009 V as shown in Figure 5.1.4.

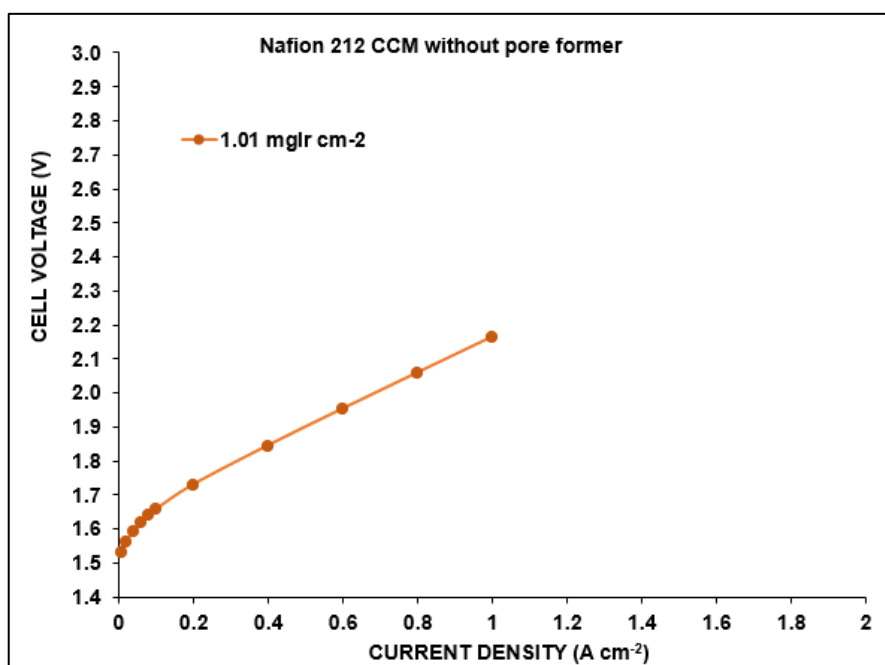


Figure 5.1.3: Current-voltage performance curves of Nafion 212 CCMs with anode electrode without pore forming additives Testing conditions: cell T = 60°C , cell P = 1 bara, 0.1 L/min water flowrate, Titanium (Pt coated) PTLs.

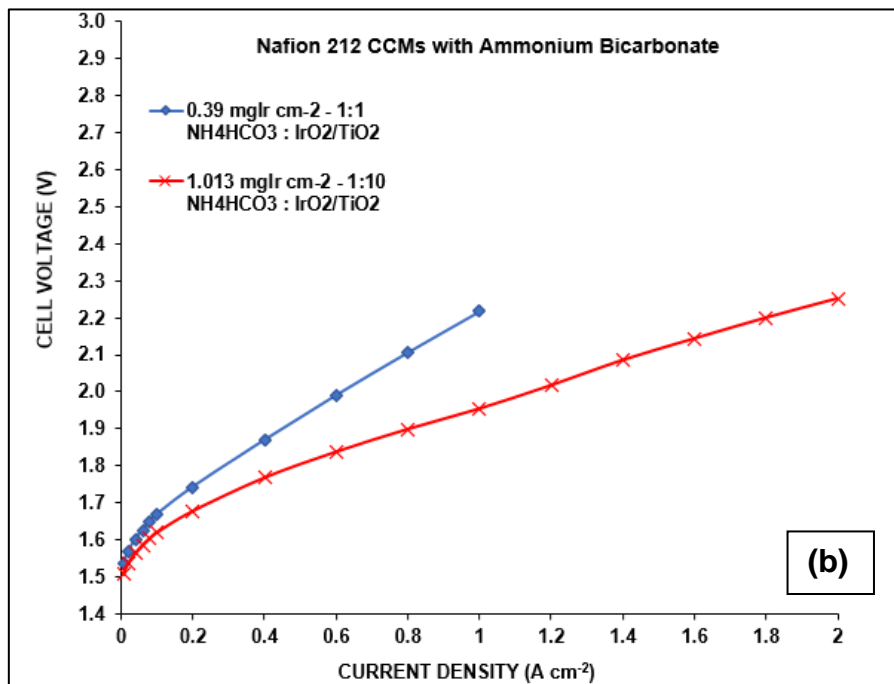
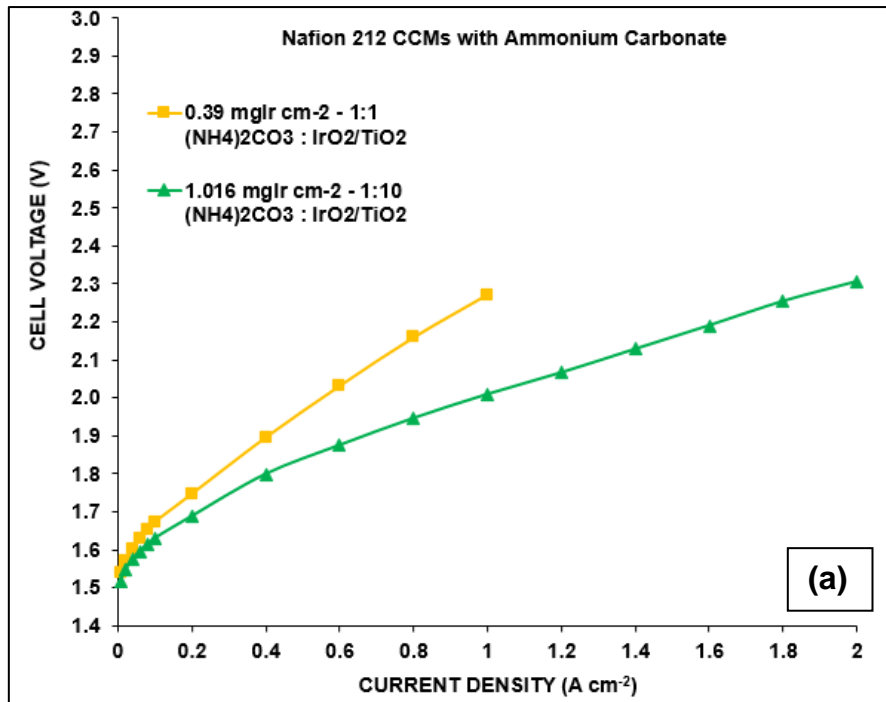


Figure 5.1.4: Current-voltage performance curves of Nafion 212 CCMs with anode electrode (a) with ammonium carbonate, (b) with ammonium bicarbonate. Testing conditions: cell T = 60°C, cell P = 1 bara, 0.1 L/min water flowrate, Titanium (Pt coated) PTLs.

This can be explained as follows: the addition of pore forming materials into the anode electrode catalyst ink formulation augmented the number and size of mesopores in the anode electrode catalyst layer permitting better oxygen products transport which is assumed resulted

in lower ohmic and concentration overvoltage thus better overall cell performance. Although CCMs with 0.39 mgIr cm⁻² anode electrode catalyst loadings showed the worst current-voltage performance, their IrO_x-TiO₂ catalyst utilisation were the highest as observed from Figure 5.1.5 which shows the current densities of all the prepared CCMs per their anode electrode iridium catalyst loading. This can be explained as follows: the introduction of more porosity in the anode electrode catalyst layer enabled the increase of the total surface area of the anode electrocatalyst particle and improved the triple-phase boundary of the anode electrode catalyst layer which allowed for a faster electrochemical reaction, therefore lower voltage required to produce the same amount of hydrogen at the same current density.

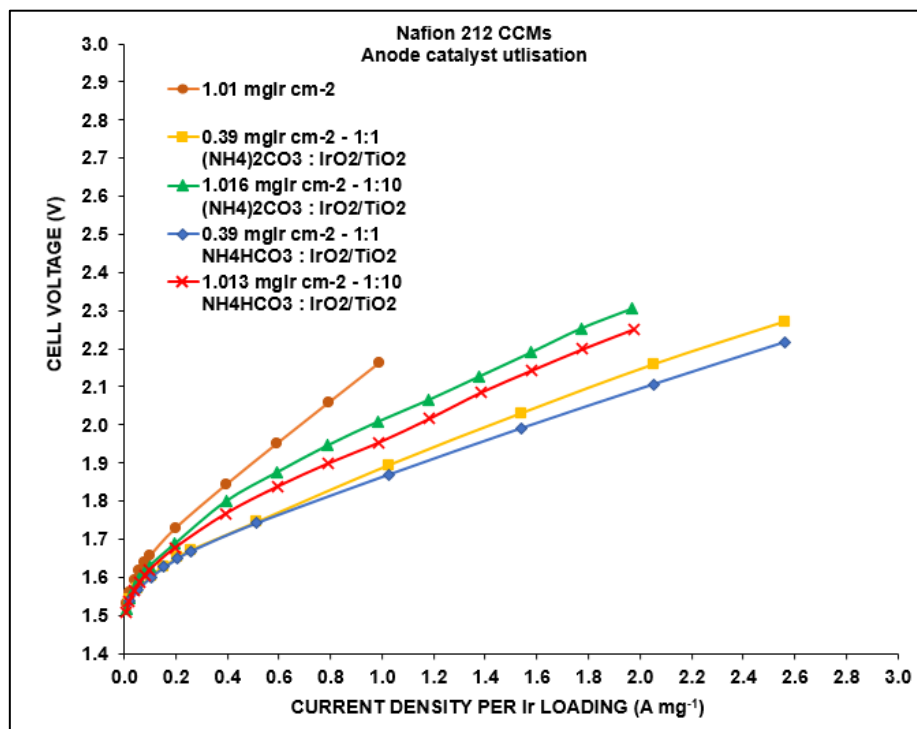


Figure 5.1.5: Performance of prepared Nafion 212 CCMs samples at current density per mg iridium loading. Testing conditions: cell T = 60°C, cell P = 1 bara, 0.1 L/min water flowrate, Titanium (Pt coated) PTLs.

5.2. Highly Porous Anode Catalyst Layer on a Thick Proton Exchange Membrane

Using the best performing pore forming substance (NH_4HCO_3), the effects of pore forming additives on the anode catalyst layer structure and overall cell performance were further investigated with a thicker perfluorosulfonic acid membrane of 135 μm thickness (Nafion 115) from DupontTM. The anode electrode of each Nafion 115 CCM sample contained 11.6 wt.% ionomer, with the catalyst loading of 1.31 mgIr cm^{-2} and 0.59 mgIr cm^{-2} for the anode electrodes without pore former and 0.4 mgIr cm^{-2} , 0.5 mgIr cm^{-2} , 0.72 mgIr cm^{-2} , and 0.95 mgIr cm^{-2} catalyst loading for the anode electrodes with 1:1, 1:1, 1:10 and 1:10 ammonium bicarbonate to $\text{IrO}_x\text{-TiO}_2$ catalyst weight ratios; respectively.

5.2.1. Anode Catalyst Layer Physical Characterisation

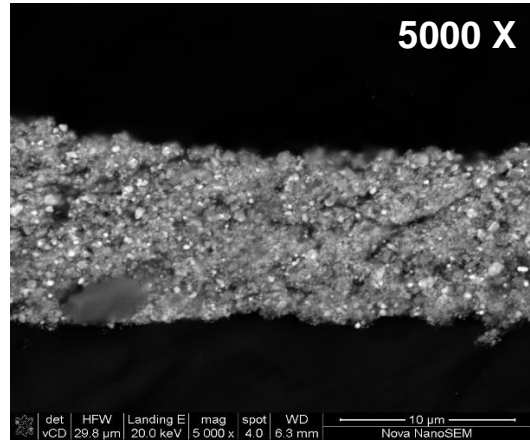
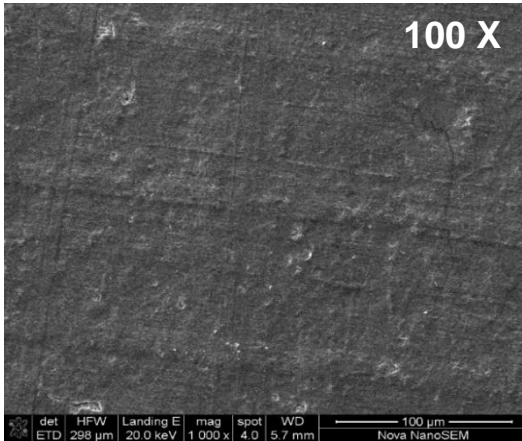
The SEM was used to investigate the fabricated anode electrodes catalyst layers structures and porosities.

5.2.1.1. Anode Catalyst Layer structure

From Figure 5.2.1, which show the SEM surface and cross-section images of the $\text{IrO}_x\text{-TiO}_2$ anode catalyst layers from prepared Nafion 115 CCM samples, it can be seen that the anode electrode catalyst inhomogeneity is closely linked with the amount of pore forming added to the catalyst ink formulation. The catalyst layer surfaces of the anode electrodes with 1:1 ammonium bicarbonate to $\text{IrO}_x\text{-TiO}_2$ weight ratio showed the highest formation of cracks compared to the anode electrodes with 1:10 ammonium bicarbonate to $\text{IrO}_x\text{-TiO}_2$ weight ratio and the anode electrode without pore forming additives which produced uniform catalyst layer. This is on par with results obtained from N212 CCM samples. Table 5.2.1 shows the summary of the physical characteristics of some of the Nafion 115 anode catalyst layers prepared in this study. It can be noticed that the anode catalyst layer thickness varies with the $\text{IrO}_x\text{-TiO}_2$ catalyst loading. The anode electrode of catalyst loading of 1.31 mgIr cm^{-2} had a catalyst layer thickness of 6.6 μm . This agrees with the expected electrode thickness from the Nafion 212 study.

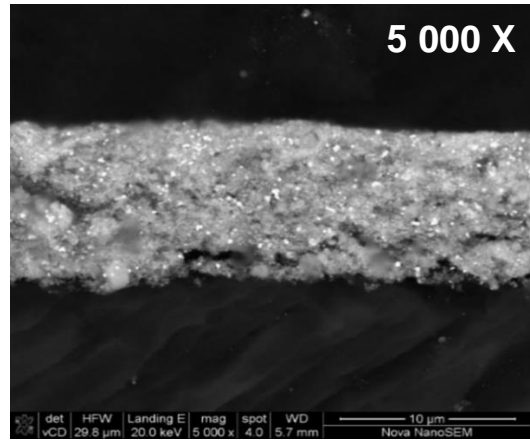
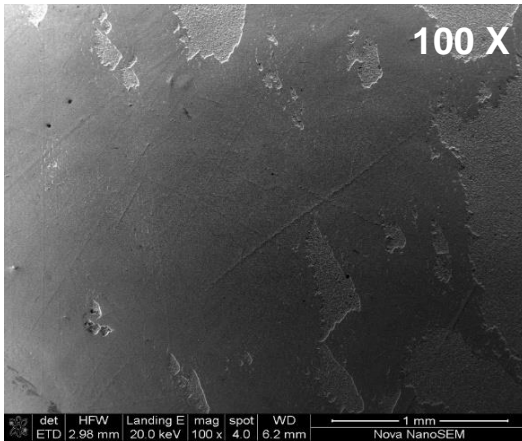
No Pore Forming Substance

1.31 mglr cm⁻²



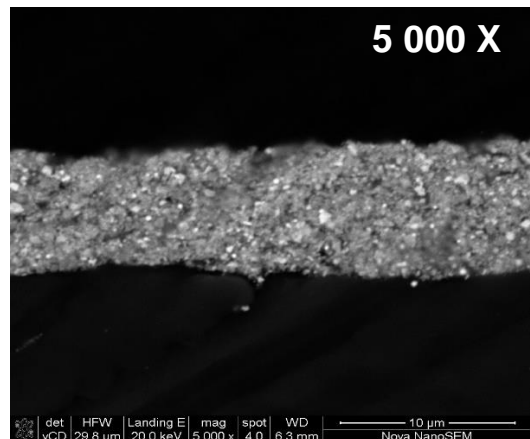
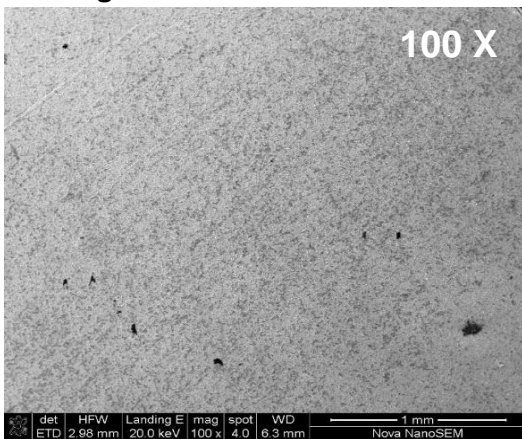
CCM with 1:10 Ammonium bicarbonate to IrO_x-TiO₂ catalyst weight ratio

0.95 mglr cm⁻²



CCM with 1:10 Ammonium bicarbonate to IrO_x-TiO₂ catalyst weight ratio

0.72 mglr cm⁻²



**CCM with 1:1 Ammonium bicarbonate to IrO_x-TiO₂ catalyst weight ratio
0.5 mgIr cm⁻²**

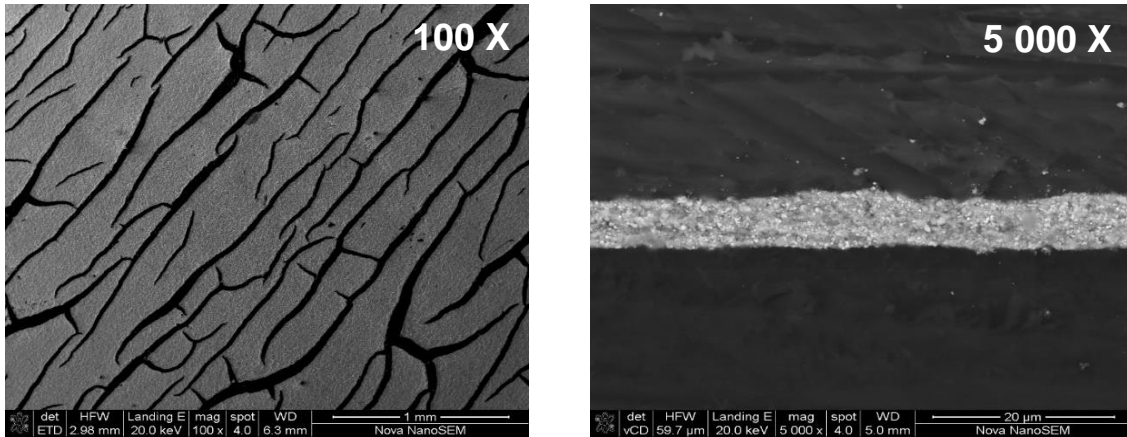


Figure 5.2.1: SEM images of IrO_x-TiO₂ anode catalyst layer surface and cross-section obtained from N115 CCMs samples without pore formers and with ammonium bicarbonate at varying pore former to catalyst weight ratios.

Table 5.2.1: Summary of anode electrode catalyst layer physical properties for some of the fabricated N115 CCM sample.

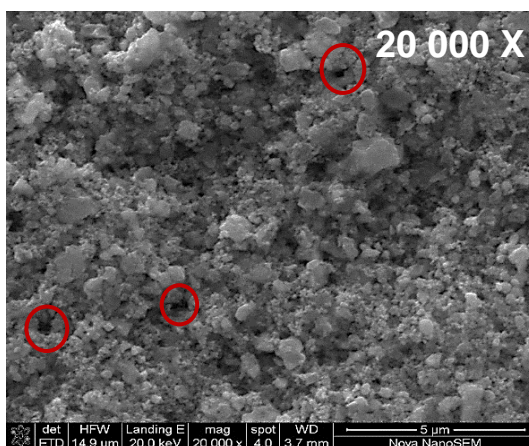
CCM	Catalyst Loadings mg cm ⁻²		Anode Catalyst Layer Specifications	
	Anode	Cathode	Thickness, μm	Standard Deviation (n = 5), μm
Sample-6	1.31	1	6.6	0.4
Sample-7	0.95	1	5.6	0.8
Sample-8	0.72	1	5.1	1.8
Sample-9	0.5	0.95	2.8	0.2

5.2.1.2. Anode Catalyst Layer Porosity

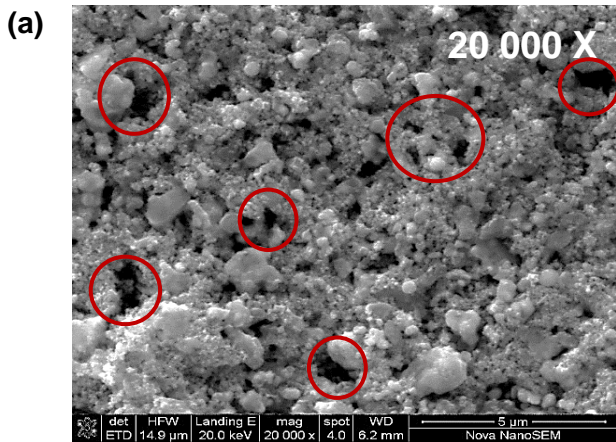
Figure 5.2.2 show SEM images of some IrO_x-TiO₂ anode electrode surface showing catalyst layer porosity obtained from Nafion 115 CCM samples without pore formers and with 1:1 and 1:10 ammonium bicarbonate to IrO_x-TiO₂ weight ratios. It can be seen that an increase of pore quantity in the anode catalyst layer was achieved with the addition of pore forming substance. Table 5.2.2, which contains the summary of some of the prepared anode electrodes catalyst layers pore volume fractions, shows that the addition of NH₄HCO₃ increased the quantity of pores in the catalyst layer by ~1.75-fold (from 40 % to 70% of the total catalyst layer volume) and ~1.5-fold (from 40% to around 60% of the total catalyst layer volume) for 1:1 and 1:10 ammonium bicarbonate to IrO_x-TiO₂ weight ratio, respectively.

No Pore forming Substance

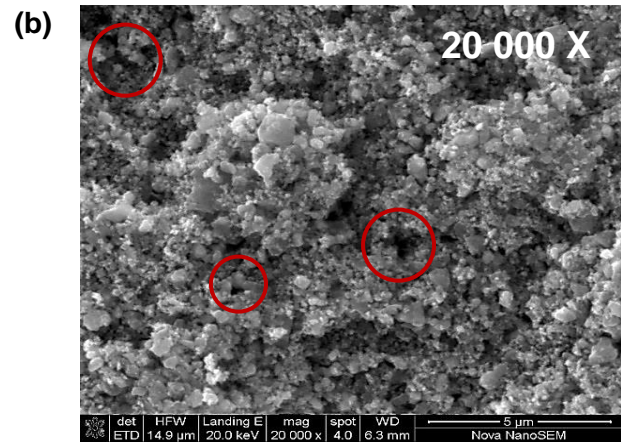
1.31 mgIr cm⁻²



**CCM with 1:10 Ammonium bicarbonate
to IrO_x-TiO₂ catalyst weight ratio
0.95 mgIr cm⁻²**



**CCM with 1:10 Ammonium bicarbonate
to IrO_x-TiO₂ catalyst weight ratio
0.72 mgIr cm⁻²**



**CCM with 1:1 Ammonium bicarbonate
to IrO_x-TiO₂ catalyst weight ratio
0.5 mgIr cm⁻²**

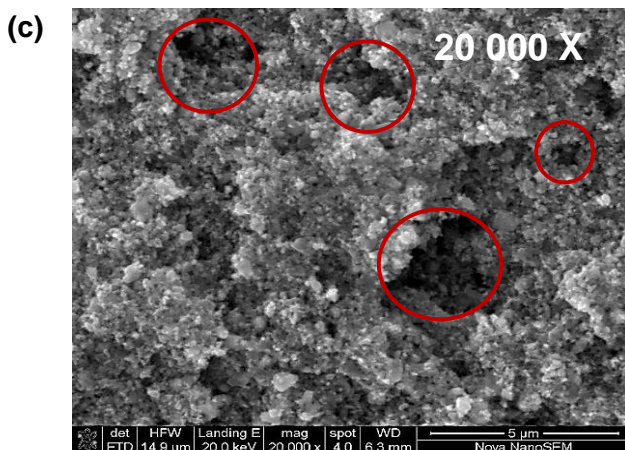


Figure 5.2.2: SEM images of IrO_x-TiO₂ anode electrode surface showing catalyst layer porosity obtained from Nafion 115 CCM samples without pore former and with ammonium bicarbonate at varying ammonium to IrO_x-TiO₂ weight ratios.

Table 5.2.2: Summary of anode electrode catalyst layer pore volume fraction for some of the fabricated Nafion 115 CCM samples.

CCM	Pore Forming Additives		Anode Catalyst Layer volume fraction		
	Type	Pore former to catalyst weight ratio	Ionomer	IrO _x -TiO ₂	Pore
Sample-6	No pore former	No pore former	0.4	0.2	0.4
Sample-7	NH ₄ HCO ₃	1:10	0.3	0.1	0.5
Sample-8	NH ₄ HCO ₃	1:10	0.4	0.1	0.5
Sample-9	NH ₄ HCO ₃	1:1	0.2	0.1	0.7

5.2.2. PEMWE Current-Voltage Performance

Figure 5.2.3 and Figure 5.2.4 show the overall electrochemical performances of the PEMWE cell for the anode electrode catalyst layers without pore forming additives, with ammonium bicarbonate at various pore forming additives weight ratio and CCMs performances normalised by iridium loadings. It can be seen that the addition of pore forming additives allowed an increase of the overall electrolyser cell performance while reducing the anode electrode catalyst loadings. CCMs with 0.72 mgIr cm⁻² anode catalyst loading 1:10 ammonium bicarbonate to IrO_x-TiO₂ weight ratio showed an average voltage performance of 1.82 V at 1 A cm⁻² (see Figure 5.2.4a) compared to CCMs with 1.31 mgIr cm⁻² anode catalyst loading and without pore forming additives which showed an average voltage of 1.89 V at 1 A cm⁻² as seen in Figure 5.2.3.

Similar trends were observed with CCMs of 0.4 mgIr cm⁻² anode catalyst loading and 1:1 ammonium bicarbonate to IrO_x-TiO₂ weight ratio performing an average voltage of 1.976 V (see Figure 5.2.4a) compared to CCMs with 0.59 mgIr cm⁻² anode catalyst loading without pore forming additives performing with an average voltage of 2.037 V at 1 A cm⁻² (refer to Figure 5.2.4). CCMs with 1:10 ammonium bicarbonate to IrO_x-TiO₂ weight ratio and anode catalyst loading of 0.95 mgIr cm⁻² showed the best performance at 1.793 V at 1 A cm⁻² while CCMs with 0.59 mgIr cm⁻² catalyst loading and without pore forming additives had the lowest performance at 2.037 V at 1 A cm⁻².

Furthermore, when normalised to the anode iridium catalyst loadings as shown in Figure 5.2.4b, the cell performance of the CCMs with the highest amount of pore forming substance required the least amount of voltage to produce the same amount of current at 1 mg of iridium. This agrees with the results obtained from Nafion 212 CCM samples.

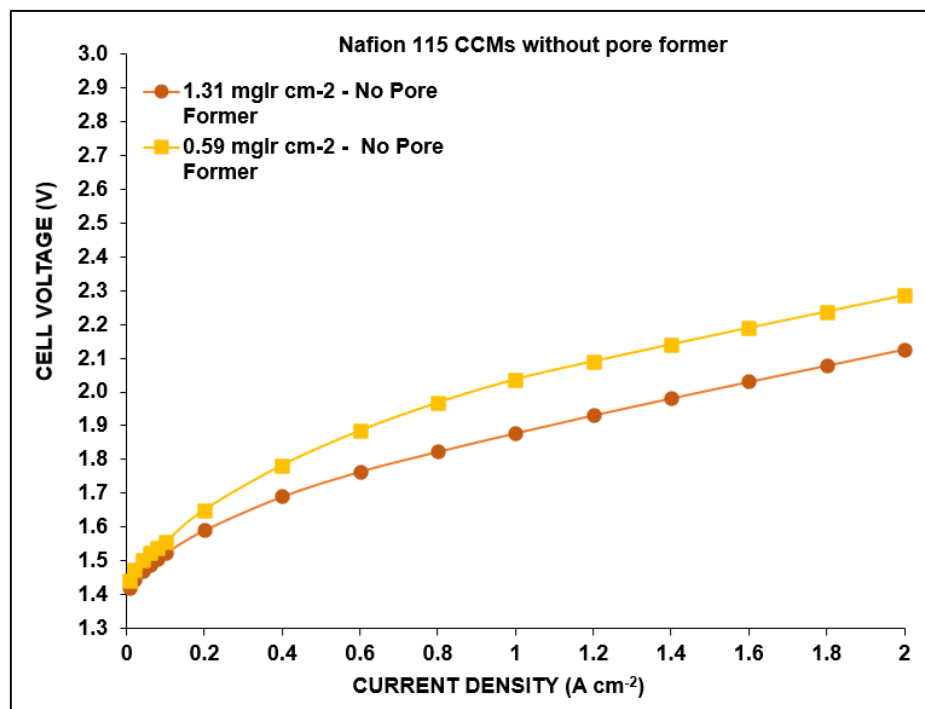


Figure 5.2.3: Current-voltage performance curves of prepared Nafion 115 CCMs with anode electrode without pore forming additives. Testing conditions: cell T = 60°C, cell P = 1 bara, 0.1 L/min water flowrate, Titanium (Pt coated) PTLs.

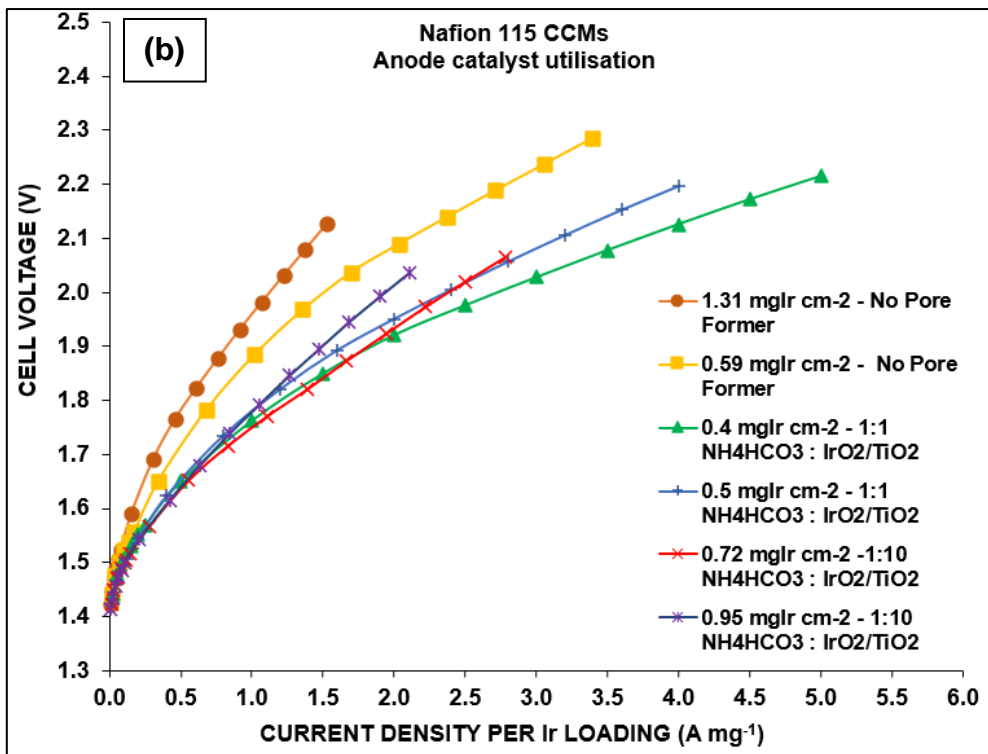
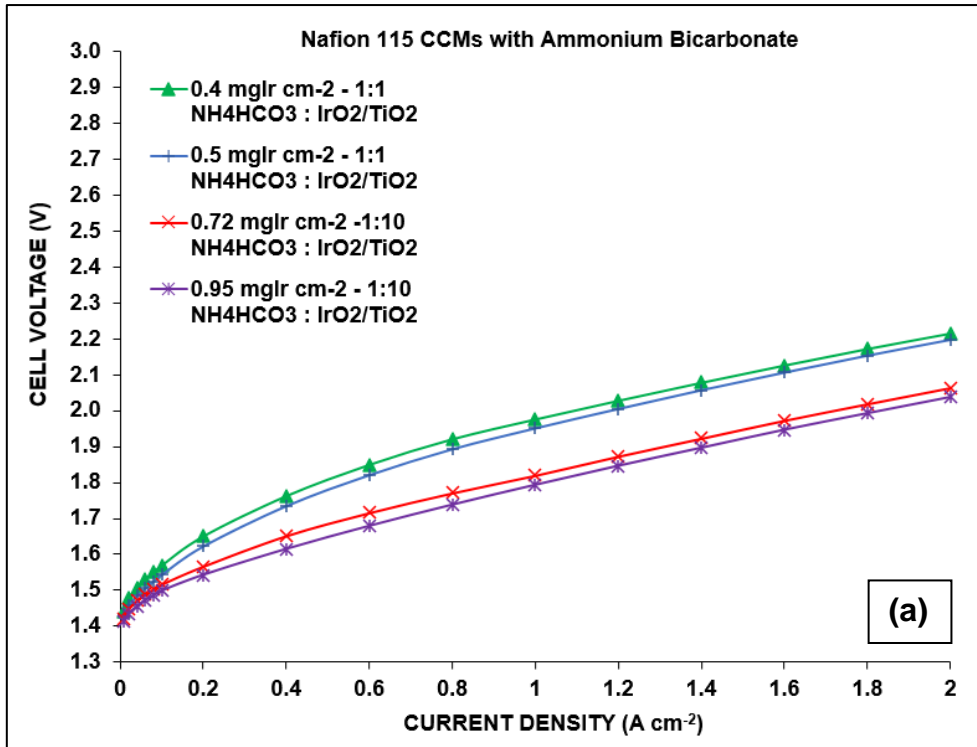


Figure 5.2.4: (a) Current-voltage performance curves of prepared Nafion 115 CCMs with anode electrode of 1:1 and 1:10 ammonium bicarbonate to $\text{IrO}_x\text{-TiO}_2$ weight ratio. And (b) Performance of all prepared Nafion 115 CCMs samples at current density per mg iridium loading. Testing conditions: cell T = 60°C, cell P = 1 bara, 0.1 L/min water flowrate, Titanium (Pt coated) PTLs.

5.3. Chapter Summary

Understanding the PEMWE anode catalyst layer structure is essential in developing low cost PEMWE systems. In this chapter, the effects of pore forming additives on the PEMWE system was investigated. Two commercial membranes were used to fabricate PEMWE CCMs samples using the fabrication method developed in the previous study. For Nafion 212 CCMs, the physical characterisation of the anode electrode catalyst layers showed that the addition of pore forming substances into the anode catalyst ink formulation resulted in inhomogeneity of the catalyst layer surface, formation of larger catalyst aggregates and uneven distribution of catalyst nanoparticle agglomerates within the anode electrode catalyst layer. With the highest amount of pore forming substances producing the most uniformity in the anode catalyst layer.

However, it was also demonstrated that the addition of pore forming additive increased of the electrode catalyst layer porosity. With the quantity of pores in the catalyst layer by 2.5-fold (from 30% to $74 \pm 1\%$ of the total catalyst layer volume) and ≈ 1.3 -fold (from 30% to $45\% \pm 0.5\%$ of the total catalyst layer volume) for pore forming materials to catalyst weight ratios of 1:1 and 1:10, respectively. The current-voltage performance evaluations of the PEMWE cell for each CCM showed that different type and quantity of pore forming additives had different effect on the cell performance. CCMs with 1:1 pore forming additive to anode catalyst weight ratio showed the worse performance while CCMs with 1:10 pore forming additive to anode catalyst weight ratio showed the best performance among all the samples. With 1:10 $(\text{NH}_4)_2\text{CO}_3$ to anode catalyst weight ratio CCMs performance of 2.009 V and 1:10 NH_4HCO_3 to anode catalyst weight ratio CCMs performance of 1.954 V at 1 A cm^{-2} , respectively. An improvement from 2.163 V at 1 A cm^{-2} for CCMs without pore formers.

For Nafion 115 CCMs, the physical characterisation of the anode electrode catalyst layer structure showed that the anode surface inhomogeneity and number of pores within the catalyst layer are closely linked with the amount of pore forming added to the catalyst ink formulation. With the addition of NH_4HCO_3 which increased the quantity of pores in the catalyst layer by ~ 1.75 -fold (from 40 % to 70% of the total catalyst layer volume) and ~ 1.5 -fold (from 40% to around 60% of the total catalyst layer volume) for 1:1 and 1:10 ammonium bicarbonate to $\text{IrO}_x\text{-TiO}_2$ weight ratio, respectively. This was on par with findings obtained from N212 CCM samples.

The electrochemical evaluation of the PEMWE cell with Nafion 115 CCMs showed that the addition of pore forming additives allowed an increase of the overall electrolyser cell performance while reducing the anode electrode catalyst loading. CCMs of $0.72 \text{ mgIr cm}^{-2}$ catalyst loading with 1:10 NH_4HCO_3 to anode catalyst weight ratio showed an average voltage performance of 1.82 V at 1 A cm^{-2} while CCMs of $1.31 \text{ mgIr cm}^{-2}$ catalyst loading without pore formers performed with an average voltage of 1.89 V at 1 A cm^{-2} .

CCMs of $0.95 \text{ mgIr cm}^{-2}$ with 1:10 NH_4HCO_3 to anode catalyst weight ratio showed the best performance with 1.793 V at 1 A cm^{-2} whilst CCMs of $0.59 \text{ mgIr cm}^{-2}$ with 1:1 NH_4HCO_3 to anode catalyst weight ratio showed the lowest performance 2.037 V at 1 A cm^{-2} . However, the normalisation of the cell performance to the iridium loading showed that CCMs with the highest number of pores in their anode electrode catalyst layer required the least amount of voltage to produce the same amount of current at 1 mg of iridium. Therefore, showing that the addition of pore forming additive into the anode catalyst ink formulation improves the anode electrode catalyst utilisation. This was also on par with findings obtained from N212 CCM samples.

CHAPTER 6 CONCLUSIONS AND RECOMMENDATIONS

6.1. Conclusions

The outcomes of this study can be summarised with three major developments.

Firstly, the Mayer rod coating technique was successfully developed and used to fabricate of PEMWE CCMs in-house. From the anode catalyst layer fabrication, it was found that the solvent mixture components ratio and the solid content of the catalyst ink had a significant influence on the physical quality of the catalyst layer. For the Mayer rod coating technique, water to IPA solvent mixture ratio of 3:1 and 30 wt.% solid ink content showed best anode catalyst layer surface homogeneity and binding to the substrate. The catalyst ink mixing time and decal transfer pressure was also investigated. It was found that 24 hours of catalyst ink mixing provided a better catalyst nanoparticle aggregate size and agglomerate uniform distribution. A full transfer of anode and cathode catalyst layers from the substrate to the proton exchange membrane was achieved with hot-pressing pressure of as low as 500 Kg/cm² and time of 3 minutes while maintaining the integrity of the catalyst layer triple-phase boundaries.

Secondly, a method for the electrochemical characterisation and benchmarking of PEMWE CCMs was also successfully developed. Commercial CCMs were used to investigate the effects of different electrochemical parameters and conditions on the accuracy and reproducibility of the test procedure. It was found that CCM tested at 4 kN cell compression provided optimal conditions for performance evaluation. Both lower and higher cell compressions showed a decrease in cell performance resulting from higher ohmic and mass transport losses, respectively. It was found that at lower cell compressions, the contact between the electrode's catalyst layers and PTLS interfaces is insufficient thereby increasing the ohmic resistance of the PEMWE system. And at higher cell compression conditions, the porous transport layer is crushed into own structure resulting in uneven supply and evacuation of water reactant and oxygen gas respectively, thereby also increasing the ohmic and mass transport losses which affect the overall PEMWE cell performance.

The investigation of the influence of water flow rate showed that it had a significant effect on the PEMWE cell performance. A flow rate of 0.2 L/min produced an overall unsteady cell temperature profile and lower CCM performance while a flow rate of 0.1 L/min generated a better temperature gradient and improved CCM performance.

Comparing different porous transport layer materials showed that titanium powder sintered PTLs on anode and cathode sides provided a better overall electrolysis performance at both 1 A cm^{-2} and 2 A cm^{-2} while the carbon paper (Toray paper 120 5wt%) PTLs showed a decrease in performance. This can be attributed to the physical properties and microporous structure of each PTL material. PTLs made of Titanium materials or Platinum coated Titanium are expected to be less corrosive in acidic media and incompressible compared to carbon PTLs. These allowed Titanium PTLs and Platinum coated Titanium PTLs to generate less resistance resulting in a minimisation of losses caused by ohmic and mass transport resistances

The effects of different electrolyser cell conditioning and evaluation measurement parameters on the overall CCM performance were also investigated. It was found that the shortest cell conditioning time of 5 min provided the lower performance while cell conditioning times of 15 min, 30 min and 45 min showed no significant differences in their results. The addition of an OCV step and the halving of the current-voltage measurement interval time from 5 min to 2.5 min improved the cell performance and stability significantly over time. Benchmarking was conducted to evaluate the developed current-voltage characterisation with respect to its accuracy and validity to water electrolysis performance. It was found that the current-voltage testing method developed in this study produced precise and reproducible performance results as the total standard deviations were 10 mV. EIS measured values were expected in the range below $150 \Omega \cdot \text{cm}^2$ at 60°C but results measured in our lab using our instrument and protocols were on average about 2 times higher showing that the HFRs data collected may not represent actual variations of the cell resistances.

Lastly, an investigation into the effects of pore forming additives in the catalyst ink formulation on the anode electrode catalyst layer structure and overall PEMWE cell performance was conducted. For both thick and thin membranes, it was found that the addition of pore formers resulted in inhomogeneity of the catalyst layer surface and formation of larger catalyst aggregates. However, the electrochemical tests showed that the addition of pore forming materials into the anode electrode catalyst ink formulation improved the overall PEMWE system performance. Furthermore, it was found that the anode catalyst ink utilisation improves with the increase of pore quantity within the anode catalyst layer.

6.2. Recommendations

Future studies should focus on the understanding of the relationship between the pore forming material quantity and the catalyst layer ohmic resistance induced losses. Also, the effects of the anode catalyst layer inhomogeneity on the electrochemical performance should be studied further to understand its influence on the overall PEMWE cell performance. Furthermore, evaluation tools and procedures (such as densometry, light transmission) should be developed to investigate the influence of the anode catalyst layer porosity on the mass transport within the catalyst layer to better understand the relationship between the catalyst layer structure and the overall PEMWE cell electrochemical performance at high current densities operations.

REFERENCES

Anette, B., Mennig, M. & Schmidt, H. 2004. Doctor Blade. In Sol-gel technologies for glass producers and users, Volume 1, pp. 89-92.

Aziz, F. & Ismail, A. 2015. Spray coating methods for polymer solar cells fabrication: A review. *Materials Science in Semiconductor Processing*, Volume 39, pp. 416-425.

Babic, U., Suermann, M., Buchi, F., Gubler, L., Schmidt, T. 2017. Critical Review—Identifying Critical Gaps for Polymer Electrolyte Water Electrolysis Development. *Journal of The Electrochemical Society*, Volume 164, pp. F387-F399.

Bender, G., Carmo, M., Smolinka, T., Gago, A., Danilovic, N., Muelle, M., Ganci, F., Fallisch, A., Letternmeier, P. 2019. Initial approaches in benchmarking and round robin testing for proton exchange membrane water electrolyzers. *International Journal of Hydrogen Energy*, Volume 44, pp 9174-9187.

Bernt, M. & Gasteiger, H. A., 2016. Influence of Ionomer Content in IrO₂/TiO₂ Electrodes on PEM Water Electrolyzer Performance. *Journal of The Electrochemical Society*, Volume 163, pp. F3179-F3189.

Bernt, M., Siebel, A. & Gasteiger, H. A. 2018. Analysis of Voltage Losses in PEM Water Electrolyzers with Low Platinum Group Metal Loadings. *Journal of The Electrochemical Society*, Volume 165, pp. F305-F314.

Bladergroen, B., Huaneng, S., Sivakumar, P. & Vladimir, L. 2012. Overview of membrane electrode assembly preparation methods for solid polymer electrolyte electrolyzer. in V. Linkov, J. Kleperis (eds.), *Electrolysis*, IntechOpen, London, pp. 45-60.

Blanco, H. & Faaij, A. 2018. A review at the role of storage in energy systems with a focus on Power to Gas and long-term storage. *Renewable and Sustainable Energy Reviews*, 01 01, Volume 81, pp. 1049-1086.

Bonifácio, R., Paschoal, J. A. & Cuenca, R. 2011. Catalyst layer optimization by surface tension control during ink formulation of membrane electrode assemblies in proton exchange membrane fuel cell. *Journal of Power Sources*, Volume 196, p. 4680–4685.

BP. 2021. BP Statistical Review of World Energy 2021. Available at: https://www.bp.com/content/dam/bp/business-sites/en/global/corporate/pdfs/energy_economics/statistical-review/bp-stats-review-2021-full-report.pdf (Accessed: 11 November 2021).

Bruce, P. G., Lisowska-Oleksiak, A., Los, P. & Vincent., C. A. 1994. Electrochemical impedance spectroscopy at an ultramicroelectrode. *Journal of Electroanalytical Chemistry*, Volume 367, pp. 279-283.

Burmeister, C. F. & Kwade, A. 2013. Process engineering with planetary ball mills. *Chemical Society Reviews*, Volume 42, pp. 7660-7667.

Carmo, M., Fritz, D. L., Mergel, J. & Stolten, D. 2013. A comprehensive review on PEM water electrolysis. *International Journal of Hydrogen Energy*, Volume 38, pp. 4901-4934.

Chen, E. 2002. Thermodynamics and Electrochemical Kinetics. *Fuel Cell Technology Handbook*, Volume 1, pp. 1-3.

Cherrington, R. & Liang, J. 2016. 2 - Materials and Deposition Processes for Multifunctionality. In: V. Goodship, B. Middleton & R. Cherrington, eds. *Design and Manufacture of Plastic Components for Multifunctionality*. William Andrew Publishing, pp. 19-51.

Colpan, C. O., Nalbant, Y. & Ercelik, M. 2018. Fundamentals of Fuel Cell Technologies. *Comprehensive Energy Systems*, Volume 1, pp. 1107-1130.

Conley, R. F. 1996. *Practical Dispersion: A Guide to Understanding and Formulating Slurries*. New Jersey: John Wiley and Sons.

Cook, T. R., Dogutan, D. K., Steven Y., Daniel G. 2010. Solar Energy Supply and Storage for the Legacy and Nonlegacy Worlds. *Chemical Reviews*, Volume 110, pp. 6474-6502.

Dale, N. V. 2009. Characterization of PEM electrolyzer and PEM fuel cell stacks using electrochemical impedance spectroscopy. *Theses and Dissertations*. 891. <https://commons.und.edu/theses/891>.

Dedigama, I., Angel, P., Ayers, K., Robinson, J.B., Shearing, P.R., Brett, D.J.L. 2014. In situ diagnostic techniques for characterisation of polymer electrolyte membrane water electrolyzers – Flow visualisation and electrochemical impedance spectroscopy. *International Journal of Hydrogen Energy*, Volume 39, pp. 4468-4482.

Dhirde, A. M., Dale, N.V., Salehfar, H., Mann, M.D; Han, T. 2010. Equivalent Electric Circuit Modeling and Performance Analysis of a PEM Fuel Cell Stack Using Impedance Spectroscopy. *IEEE Transactions on Energy Conversion*, September, Volume 25, pp. 778-786.

- Di-Risio, S. & Yan, N. 2007. Piezoelectric Ink-Jet Printing of Horseradish Peroxidase: Effect of Ink Viscosity Modifiers on Activity. *Macromolecular Rapid Communications*, Volume 28, pp. 1934 - 1940.
- Dixit, M. B., Harkey, B. A., Shen, F. & Hatzell, K. B. 2018. Catalyst layer ink interactions that affect coatability. *Journal of The Electrochemical Society*, Volume 165, p. F264.
- Durst, R. A. 1997. Chemically modified electrodes: recommended terminology and definitions (IUPAC Recommendations 1997). *Pure and applied chemistry*, Volume 69, pp. 1317-1324.
- Ebnesajjad, S. 2004. Chapter 4 - Surface and Material Characterization Techniques. *Surface Treatment of Materials for Adhesive Bonding (Second Edition)*, pp. 39-75.
- Fabbri, E. & Schmidt, T. J. 2018. Oxygen evolution reaction—the enigma in water electrolysis. *ACS Catalyst*, Volume 9, pp. 765-9774.
- Feng, Q., Yuan, X., Liu, G., Wei, B., Zhang, Z., Li, H., Wang, H. 2017. A review of proton exchange membrane water electrolysis on degradation mechanisms and mitigation strategies. *Journal of Power Sources*, Volume 366, pp. 33-55.
- Firtina, İ., Güner, S. & Albostan., A. 2011. Preparation and characterization of membrane electrode assembly (MEA) for PEMFC. *International Journal of Energy Research*, Volume 35, pp. 146-152.
- Fischer, A., Jindra, J. & Wendt, H. 1998. Porosity and catalyst utilization of thin layer cathodes in air operated PEM-fuel cells. *Journal of Applied Electrochemistry*, Volume 28, pp. 277-282.
- Fouda-Onana, F., Chandesris, M., Medeau, V., Chelghoum, S., Thoby, D., Guillet, N. 2016. Investigation on the degradation of MEAs PEM water electrolyzers part I: Effects of testing conditions on MEA performances and membrane properties. *International Journal of Hydrogen Energy*, Volume 41, pp. 16627-16636.
- Gahleitner, G. 2013. Hydrogen from renewable electricity: An international review of power-to-gas pilot plants for stationary applications. *International Journal of Hydrogen Energy*, Volume 38, pp. 2039-2061.
- Gamburzev, S. & Appleby, A. J. 2002. Recent progress in performance improvement of the proton exchange membrane fuel cell (PEMFC). *Journal of power sources*, Volume 107, pp. 5-12.
- Gerardi, M. H., 2003. *The Microbiology of Anaerobic Digesters*. New Jersey: John Wiley and Sons.

Ghosh, S. K. & Hasimur Rahaman. 2019. Chapter 16 - Noble Metal–Manganese Oxide Hybrid Nanocatalysts. *Noble Metal-Metal Oxide Hybrid Nanoparticles*, pp. 313-340.

Götz, M., Lefebvre, J., Mors, F., Kosch, A.M., Kolb, T. 2016. Renewable Power-to-Gas: A technological and economic review. *Renewable Energy*, Volume 85, pp. 1371-1390.

Grigoriev, S., Millet, P., Volobue, S. & V. F. 2009. Optimization of porous current collectors for PEM water electrolyzers. *International Journal of Hydrogen Energy*, Volume 34, pp. 4968-4973.

Handbook. 2003. High shear mixing advances for foods, pharmaceuticals, cosmetics. 2nd ed. In the *Mixing, Blending and Size Reduction Handbook*.

Harrison, R. 1993. ed. *Protein purification process engineering*. CRC Press, Volume 18.

HIAT, n.d. Hydrogen and Informatics Institute of Applied Technologies. [Online] Available at: https://www.hiat.de/download/HIAT_CCMs.pdf [Accessed 3 August 2020].

Hill, M. R. 2013. Preparation of catalyst coated membranes using screen printing, University of Cape Town. *Theses and Dissertations*. 191.

Hoth, C.N., Schilinsky, P., Choulis, S.A., Balasubramanian, S., Brabec, C.J. 2013. Solution-processed organic photovoltaics. In: Cantatore, E. (Ed.), *Applications of Organic and Printed Electronics, Integrated Circuits and Systems*.

International Energy Agency. 2021. Climate Considerations in the International Energy Outlook (IEO2021). Available at: <https://www.eia.gov/outlooks/ieo/climate.php> (Accessed 3 August 2021).

IPCC. 2021. Climate Change 2022: Mitigation of Climate Change. Available at: <https://www.ipcc.ch/report/ar6/wg3/> (Accessed 3 August 2021).

Kopeliovich, D. 2015. SubTech. Available at: <http://www.substech.com/dokuwiki/doku.php?id=homogenization> (Accessed 2 September 2019)

Kumar, S. S. & Himabindu, V. 2019. Hydrogen production by PEM water electrolysis – A review. *Materials Science for Energy Technologies*, 2(3), pp. 442-454.

Kúš, P. 2019. *Thin-Film Catalysts for Proton Exchange Membrane Water Electrolyzers and Unitized Regenerative Fuel Cells*, Springer International Publishing.

Latham, R. A. 2004. Algorithm development for electrochemical impedance spectroscopy diagnostics in PEM fuel cells. Volume 102, pp 458-463.

Lettenmeier, P., Philipp, K., Kolb, S., Fredrich, K.A. 2017. Comprehensive Investigation of Novel Pore-Graded Gas Diffusion Layers for High-Performance and Cost-Effective Proton Exchange Membrane Electrolyzers. *Energy & Environmental Science*, Volume 10, pp. 2521-2533.

Lewis, N. S. & Nocera, D. G. 2006. Powering the planet: Chemical challenges in solar energy utilization. *Proceedings of the National Academy of Sciences*, Volume 103, pp. 15729-15735.

Liang, X., Pan, G., Xu, L. & Wang, J. 2015. A modified decal method for preparing the membrane electrode assembly of proton exchange membrane fuel cells. *Fuel*, Volume 139, pp. 393-400.

Majasan, J. O., Cho, J.I.S., Dedigama, I., Tsaoulidis, D., Brett, D.J.L. 2018. Two-phase flow behaviour and performance of polymer electrolyte membrane electrolyzers: Electrochemical and optical characterisation. *International Journal of Hydrogen Energy*, Volume 43, pp. 15659-15672.

Malkow, T., Pilenga, A. & G. Tsotridis. 2018. EU harmonised test procedure: electrochemical impedance spectroscopy for water electrolysis cells, Luxembourg: Publications Office of the European Union.

Mawungwe, N., Susac, D. & Mohamed, R. 2022. Scanning Electron Microscopy: New Technique. University of Cape Town. Theses and Dissertation (submitted).

Maximilian, B. & Gasteiger, H. A. 2016. Influence of Ionomer Content in IrO₂/TiO₂ Electrodes on PEM Water Electrolyzer Performance. *Journal of The Electrochemical Society*, 25 August, Volume 163, pp. F3179-F3189.

Merwe, J. v. d., Uren, K., Schoor, G. v. & Bessarabov, D. 2014. Characterisation tools development for PEM electrolyzers. *International Journal of Hydrogen Energy*, 3 September, Volume 39, pp. 14212-14221.

Metz, S., Fallisch, A., Lickert, T., Helmle, J., Bender, G., Young, J., Carmo, M., Smolinka, T. 2019. Laboratory test cells for advanced component characterisation in PEM water electrolysis. Freiburg, Fraunhofer Institute for Solar Energy Systems Ise.

Millet, P., Mbemba, N., Grigoriev, S.A., Fateev, V.N., Aukauloo, A., Etievant, C. 2011. Electrochemical performances of PEM water electrolysis cells and perspectives. *International Journal of Hydrogen Energy*, Volume 36, pp. 4134 - 4142.

Mo, J., Kang, Z., Yang, G., Retterer, S.T., Zhang, F.Y. 2016. Thin liquid/gas diffusion layers for high-efficiency hydrogen production from water splitting. *Applied Energy*, Volume 117, pp. 817-822.

Newman, J. S. 2012. *Electrochemical systems*. Third edition. New Jersey: Prentice Hall.

Nie, J. & Chen, Y. 2010. Numerical modeling of three-dimensional two-phase gas–liquid flow in the flow field plate of a PEM electrolysis cell. Volume 35, pp. 3183-3197.

O'Kane, M. 2017. *Solution-Processing Techniques: A Comparison*. [Online] Available at: <https://www.ossila.com/pages/solution-processing-techniques-comparison> [Accessed 17 May 2021].

Orazem, M. E. & Tribollet, B. 2008. Electrohydrodynamic Impedance. In: E. E. Society, ed. *Electrochemical impedance spectroscopy*. New Jersey: A JOHN WILEY & SONS, pp. 383-389.

Paipetis, A. & Kostopoulos, V. 2013. *Carbon Nanotube Enhanced Aerospace Composite Materials: A New Generation of Multifunctional Hybrid Structural Composites*. 1st ed. New York: Springer, Dordrecht.

Paipetis, A. & Kostopoulos, V. 2013. Carbon nanotubes for novel hybrid structural composites with enhanced damage tolerance and self-sensing/actuating abilities. pp. 1-20.

Park, H.-S., Yong-Hun Cho, Y.-H. C., Jung, C. R. & Sung, J. H. J. a. Y.-E. 2007. Performance enhancement of PEMFC through temperature control in catalyst layer fabrication. *Electrochemical Acta*, December, Volume 53, pp. 763--767.

Particle-Technology-Labs. 2017. *Mercury Intrusion Porosimetry*. [Online] Available at: <https://www.particletechlabs.com/analytical-testing/gas-adsorption-and-porosimetry/mercury-intrusion-porosimetry> [Accessed 15 May 2021].

Pasupathi, S., Su, H., Liang, H. & Pollet, B. 2015. *Advanced Technologies for Proton-Exchange Membrane Fuel Cells*. December. pp. 405-420.

Pellow, M. A., Emmott, C. J. M., Barnhart, C. J. & Benson, S. M. 2015. Hydrogen or batteries for grid storage? A net energy analysis. *Energy & Environmental Science*, Volume 8, pp. 1938-1952.

Plötze, M. & Niemz, P. 2011. Porosity and pore size distribution of different wood types as determined by mercury intrusion porosimetry. *European Journal of Wood and Wood Products*, November, Volume 69, pp. 649-657.

Prasanna, M., Ha, H., Cho, E., Hong, S. 2004. Investigation of oxygen gain in polymer electrolyte membrane fuel cells. 5 October, Volume 137, pp. 1-8.

R.D. Specialities. 2016. Size Selection Chart: Common Sizes. [Online] Available at: <https://www.rdspecialities.com/pages/size-selection> [Accessed 22 July 2019].

Rajan, Z. S., Binninger, T., Kooyman, P. J. & Mohamed, D. S. a. R. 2020. Organometallic chemical deposition of crystalline iridium oxide nanoparticles on antimony-doped tin oxide support with high-performance for the oxygen evolution reaction. *Catalysis Science & Technology*, Volume 10, pp. 3938--3948.

Randles, J. E. B. 1947. Kinetics of rapid electrode reactions. *Discussions of the faraday society*, Volume 1, pp. 11-19.

Reshetenko, T. V., Kim, H.-T. & Kweon., H.-J. 2007. Cathode structure optimization for air-breathing DMFC by application of pore-forming agents. *Journal of Power Sources*, Volume 171, pp. 433-440.

Ryu, J. G., Lee, P. S., Kim, H. S. & Lee, J. W. 2001. Development of PP-Based Nanocomposites via in-situ Copolymerisation and Melt Intercalation with the Power Ultrasonic Wave. *Macromol. Res.* Volume 10, pp.187–193.

Santangelo, P., Cannio, M. & Romagnoli, M. 2019. Review of catalyst-deposition techniques for PEMFC electrodes. *TECNICA ITALIANA-Italian Journal of Engineering Science*, Volume 63, pp. 65-72.

Schiebahn, S., Grube, T., Robinius, M., Tietze, V., Kumar, B., Stolten, D. 2015. Power to gas: Technological overview, systems analysis and economic assessment for a case study in Germany. *International Journal of Hydrogen Energy*, Volume 40, pp. 4285-4294.

Schmidt, O., Gambhir, A., Staffell, I., Hawkes, A., Nelson, J., Few, S. 2017. Future cost and performance of water electrolysis: An expert elicitation study. *International Journal of Hydrogen Energy*, Volume 42, pp. 30470-30492.

Shen, M., Bennett, N., Ding, Y. & Scott, K. 2011. A concise model for evaluating water electrolysis. *International Journal of Hydrogen Energy*, Volume 36, pp. 14335-14341.

Shen, P., Wang, C., Sun, X. & Zhang, J. 2018. *Electrochemical energy: advanced materials and technologies*. 1st ed. CRC press.

Smalley, R. E. 2005. Future Global Energy Prosperity: The Terawatt Challenge. *MRS Bulletin*, Volume 30, pp. 412-417.

Smil, V. 2017. Energy Transitions: Global and National Perspectives (Second expanded and updated edition). 2nd ed. Praeger.

Song, Y., Wei, Y., Xu, H., Leonard, J., James, M. 2005. Improvement in high temperature proton exchange membrane fuel cells cathode performance with ammonium carbonate. *Journal of power sources*, 1 March, Volume 141, pp. 250-257.

Sterner, M. 2009. Bioenergy and renewable power methane in integrated 100% renewable energy systems: Limiting global warming by transforming energy systems. Kassel: kassel university press GmbH.

Suermann, M., Schmidt, T. J. & Büchi, F. N. 2015. Investigation of mass transport losses in polymer electrolyte electrolysis cells. *Ecs Transactions*, Volume 69, pp. 1141-1148.

Therdthianwong, A., Ekdharmasuit, P. & Therdthianwong, S. 2010. Fabrication and performance of membrane electrode assembly prepared by a catalyst-coated membrane method: effect of solvents used in a catalyst ink mixture. *Energy & fuels*, Volume 24, pp. 1191-1196.

Tucker, M. C., Madeleine, O., Lund, P.B., Thomas, J.O. 2005. The pore structure of direct methanol fuel cell electrodes. *Journal of the Electrochemical Society*, Volume 152, p. A1844.

Turner, J., Svuerdrup, G., Maness, P., Kroposki, B., Blake, D. 2008. Renewable hydrogen production. *International Journal of Energy Research*, Volume 32, pp. 379-407.

Tyler, E. 2010. Aligning South African energy and climate change mitigation policy. *Climate Policy*, Volume 10, pp. 575-588.

Winkler, H. & Marquand, A. 2011. Changing development paths: From an energy-intensive to low-carbon economy in South Africa. *Climate and Development*, Volume 1, pp. 47-65.

Xie, J., More, K. L., Zawodzinski, T. A. & Smith, W. H. 2004. Porosimetry of MEAs made by "thin film decal" method and its effect on performance of PEFCs. *Journal of the Electrochemical Society*, 8 November, Volume 151, p. A1841.

Xiong., L. & Manthiram, A. 2005. High performance membrane-electrode assemblies with ultra-low Pt loading for proton exchange membrane fuel cells. *Electrochemical Acta*, Volume 50, pp. 3200-3204.

Xu, J., Miao, R., Zhao, T., Wu, J., Wang, X. 2011. A novel catalyst layer with hydrophilic–hydrophobic meshwork and pore structure for solid polymer electrolyte water electrolysis. *Electrochemistry Communications*, Volume 13, pp. 437-439.

Yao, Y. & Liu, D. 2012. Comparison of low-field NMR and mercury intrusion porosimetry in characterizing pore size distributions of coals. *Fuel*, May, Volume 95, pp. 152-158.

Yu, H., Bonville, L., Jankovic, J. & Maric, R. 2019. Microscopic insights on the degradation of a PEM water electrolyzer with ultra-low catalyst loading. *Applied Catalysis B: Environmental*, Volume 260, p. 118194.

Zhang, H., Wang, X. & Zhang, J. Z. a. J. 2008. *Conventional catalyst ink, catalyst layer and MEA preparation*. London: Springer.

Zhao, J., He, X., Wang, L., Tian, J., Wana, C., Jiang, C. 2007. Addition of NH_4HCO_3 as pore-former in membrane electrode assembly for PEMFC. *International Journal of Hydrogen Energy*, Volume 32, pp. 380-384.

Zhao, J. & Liu, X. L. 2019. The effect of ink dilution and evaporation on the microstructures of catalyst layers in polymer electrolyte membrane fuel cells. *International Journal of Energy Research*, 2 August, Volume 43, pp. 6799-6811.

Zlotorowicz, A., Jayasayee, K., Dahl, P.I., Thomassen, M.S., Kjelstrup, S. 2015. Tailored porosities of the cathode layer for improved polymer electrolyte fuel cell performance. *Journal of Power Sources*, Volume 287, pp. 472-477.

APPENDIX

- **Chapter 3**

Table containing abbreviations and descriptions for the process flow diagram of the PEMWE test bench.

Table 0.1: Abbreviations and descriptions for the process flow diagram of the PEMWE test bench.

Abbreviation	Expansion	Function performed
FC	Flow Controller	Flow measurement and control
FLT	Flow Level Transmitter	Transmitting flow signal
HEX	Heat Exchanger	Cooling and heating of system fluids
HV	Hand Valve	Manual flow control
LVS	Level Sensor	Fluid level measurement and control
PCV	Pressure Control Valve	Relieving excess pressure in case of high-pressure situation
PT	Pressure Transmitter	Transmitting pressure signal
SP	Separator Tank	Two phase fluids separation
TC	Temperature Controller	Controlling/regulating temperature
TT	Temperature Transmitter	Transmitting measured temperature signals

- **Fabricated PEMWE electrodes Samples Specifications**

The Table below provides a summary of the properties of all the PEMWE electrodes samples prepared in this study.

Table 0.2: Properties summary of PEMWE electrodes prepared samples using CCM method.

Component	Type	Dimension	Specification
Membrane	- Nafion 212 - Nafion 115	25 cm ²	- 50.8 mm thick - 135 mm thick
Active area		4 cm ²	
Anode Catalyst Loadings	IrO _x -TiO ₂		<p>Nafion 115</p> <ul style="list-style-type: none"> - 1.31 ± 0.11 mgIr cm⁻² - 0.95 ± 0.3 mgIr cm⁻² (1:10 NH₄HCO₃ to IrO_x-TiO₂ catalyst weight ratio) - 0.72 ± 0.2 mgIr cm⁻² (1:10 NH₄HCO₃ to IrO_x-TiO₂ catalyst weight ratio) - 0.59 ± 0.03 mgIr cm⁻² - 0.5 ± 0.11 mgIr cm⁻²(1:1 NH₄HCO₃ to IrO_x-TiO₂ catalyst weight ratio) - 0.4 ± 0.01 mgIr cm⁻²(1:1 NH₄HCO₃ to IrO_x-TiO₂ catalyst weight ratio) <p>Nafion 212</p> <ul style="list-style-type: none"> - 1.016 ± 0.12 mgIr cm⁻² (1:10 (NH₄)₂CO₃ to IrO_x-TiO₂ catalyst weight ratio) - 1.013 ± 0.03 mgIr cm⁻² (1:10 NH₄HCO₃ to IrO_x-TiO₂ catalyst weight ratio) - 1.01 ± 0.1 mgIr cm⁻² - 0.39 ± 0.01 mgIr cm⁻² (1:1 (NH₄)₂CO₃ to IrO_x-TiO₂ catalyst weight ratio) - 0.39 ± 0.01 mgIr cm⁻² (1:1 NH₄HCO₃ to IrO_x-TiO₂ catalyst weight ratio)
Anode Ionomer Content	D2021		11.6 wt.%
Pore forming material to catalyst weight ratio	Ammonium Carbonate		- 1:10 - 1:1
Pore forming material weight ratio	Ammonium Hydrogen Carbonate		- 1:10 - 1:1
Cathode Catalyst Loadings	Pt/C		0.95 ± 0.15 mgPt cm ⁻²
Cathode Ionomer Content	Long Side Chain 1100EW		12 wt.%

- Chapter 4
- PEMWE electrochemical characterisations procedures summary

Table 0.3: Testing protocols for the catalyst coated membrane samples electrochemical test.

Step	Description	Specifications	Time, hr
CCM Cleaning	Immersed CCM in acid solution	0.1 M H ₂ SO ₄ solution	1
Swollen State	Immersed CCM in DI water	≈ 18 MΩ cm ultrapure water	2
PEMWE Cell Conditioning	Apply water hot water into the cell until desired conditions reached	60°C de-ionised water 0.1 L min ⁻¹ water flowrate ΔT 2°K cell temperature	2
PEMWE Cell Activation	OCV measurement	0 A cm ⁻²	0.083
	Current controlled operation	0.2 A cm ⁻²	0.25
	Current controlled operation	1 A cm ⁻²	0.25
	Voltage controlled operation until variation is less than 1% per hour	1.7 V	2
PEMWE Cell Electrochemical Evaluation	I-V Polarisation Curves measurements	Low to high current density curve (step A) Δi = 0.02 A cm ⁻² from 0.0 to 0.1 A cm ⁻² at 2.5 min/ramp Δi = 0.2 A cm ⁻² from 0.1 A cm ⁻² at 2.5 min/ramp until a current density of 2.0 A cm ⁻² is reached	≈1.67
		High to low current density curve (Step B) Reverse step A	≈1.67
	EIS measurements	± 5% current perturbation EIS at 0.0 A/cm ² and 0.2 A/cm ² at frequency range of 100 mHz to 100 kHz	0.06

- **Chapter 5**

For Nafion 212, sample 1 porosity calculations.

Umicore Ir75 0480					
IrO _x	wt. %	75%	ρ	11.7	g/cm ³
TiO ₂	wt. %	25%	ρ	4.23	g/cm ³
Average			ρ	9.83	g/cm ³
D2021					
Ionomer	wt. %	20%	ρ	2.1	g/cm ³

For the CCM sample without pore forming substance of anode catalyst loading of 1.01 mgIr cm⁻² and 11.6 wt.% ionomer (0.133 mgIr cm⁻²).

Catalyst:

$$V_{cat} = \frac{L_{cat}}{\rho_{cat} \times t_{an}} = \frac{1.01}{9.83 \times 6.293} = 0.43$$

Ionomer:

$$V_{ion} = \frac{L_{ion}}{\rho_{ion} \times t_{an}} = \frac{0.133}{2.1 \times 6.293} = 0.239$$

Pore:

$$V_{pore} = 1 - V_{cat} - V_{ion} = 1 - 0.43 - 0.239 = 0.332$$